PONTIFICIA
UNIVERSIDAD
CATÓLICA
DE CHILE

FACULTAD DE FÍSICA
INSTITUTO DE ASTROFÍSICA

Fast Radio Bursts: Constraining possible astrophysical scenarios from a particle acceleration model

POR

FELIPE ZEPEDA GONZÁLEZ

Tesis de Magister presentada a la Facultad de Física de la
Pontificia Universidad Católica de Chile,
para optar al grado académico de Magister en Astrofísica.

Supervisor	:	Dr. Andreas Reisenegger (UMCE)
Correctores	:	Dr. Franz Bauer (PUC)
		Dr. Mario Riquelme (U. de Chile)

Noviembre, 2020
Santiago, Chile

"Si no es ahora, ¿Cuándo?"

Eckhart Tolle

Agradecimientos

Con gusto agradecería a todas y cada una de las personas que, de una u otra forma, han participado en lo que define a mi situación de vida actual, pero me sería imposible de plasmarlo todo en esta pequeña sección. Aún así, permítanme decirles que no hay momento de mi vida en que no esté agradeciendo hasta la más mínima gota de energía que fluye desde el mundo hacia mí. Habiendo dicho lo anterior, sí me resulta fácil recordar a gente que ha estado a mi lado a lo largo de estos últimos años, dándome apoyo, consejos, ánimos, conocimiento, sabiduría y luz. A mis padres, herman@s y tí@s, gracias, los amo. A mis sobrinos, gracias, los amo. A mis mascotas, gracias, los amo. A mis amigos, Fabi, Beto, Rodri, Seba, Cami, Fefi, Joako, Mari, Kari, Poli, Cristian, entre otros: Gracias, los amo. A Eckhart, gracias por su amorosa guía. A mi profesor de Magister, Andreas Reisenegger, gracias por todo. A mis profesores de infancia y universidad, gracias, gracias, gracias.

Quienes me conocen más, saben que amo la música, y es por eso que me permito terminar esta sección citando (y también agradeciendo en el acto) a un queridísimo cantautor chileno, Cristobal Briceño, quien describió en uno de sus tantas creaciones la forma en que percibo la vida:

"Mi jardín no es realmente mi jardín. Mi jardín no es realmente mi jardín, pero lo riego como si mío fuera, como si fuera mío".

Abstract

Fast Radio Bursts (FRBs) are bright millisecond-long radio flashes whose luminosities range between $L \sim 10^{38} - 10^{46}$ erg/s, thus implying strong electromagnetic waves (EMW), of amplitude $E = B$, in their vicinity. We analyzed the acceleration experienced by particles under such intense fields, and we obtained that they will quickly –within the inverse of the cyclotron frequency, $\omega_c^{-1} \equiv mc/eE$– become relativistic and move in the direction of the incident wave, $\hat{k}$ (a process known as "surfatron"). In this process, the particles periodically reach a Lorentz factor, $\gamma_{max} \sim (\omega_c/2\pi\nu)^2 \gg 1$, which remains valid up to the radial distance, $r_f = (e/2mc\nu)\sqrt{L/c} \sim 3 \times 10^{10}\,\mathrm{cm}\ (m/m_p)^{-1} L_{42}^{1/2}\,\nu_9^{-1}$. We analyzed the possible formation of a charge separation region (CSR) due to the different r_f of protons and electrons, and then we argue that the electron acceleration process can be disrupted by the CSR beyond r_{f,p^+}. We also analyzed the incoherent and coherent radiation processes experienced by the accelerating particles. We concluded that the coherent radiation can substantially modify the incident wave, potentially dispersing its electromagnetic energy budget if the emission mechanism of the FRB is activated at $r_{act} \lesssim r_{f,p^+}$. Based on this, and assuming a neutron star (NS) progenitor scenario for FRBs, we argue that our model disfavours mechanisms in which the FRB is emitted from within the magnetosphere of a NS or magnetar. Although the model was applied to FRBs, it is applicable to other FRB-like phenomena, such as the "giant pulses" of radio pulsars. In order to reduce several limitations of our model, we propose to extend our analysis by self-consistently solving the Maxwell equations and the equations of motion for the plasma.

Contents

List of Figures

Chapter 1

Introduction

Fast radio burst (FRBs) are bright ($\sim 0.1-100$ Jy), millisecond-long radio (0.3−8 GHz; Chawla et al., 2020, Shannon et al., 2018, Gajjar et al., 2018) flashes. Their extragalactic origin has been confirmed for several events (Chatterjee et al., 2017, Bannister et al., 2019, Ravi et al., 2019, Prochaska et al., 2019, Marcote et al., 2020), but their progenitors remain unknown for the major part of their population (to date, the only exception is for FRB 121102; see The CHIME/FRB Collaboration et al., 2020, Bochenek et al., 2020). In the following sections we will provide some background about the history and properties of FRBs as well as the motivation of our work in this thesis.

1.1 A little history

The history of the detection of radio transients is closely related to the search for pulsars –rapidly rotating neutron stars (NS) whose emission comes from the open magnetic field lines that emerge from the NS's magnetic poles– in 1967 (Hewish et al., 1968, Lorimer and Kramer, 2004). Over the years, the search for more pulsars motivated the development of instrumentation towards higher time resolution, broader bandwidths and narrower frequency channels, which favored more sensitive pulsar with higher "dispersion measures" (DM; see Subsection 1.2.1). Several decades later, although single-pulse searches were left aside given the more fruitful finding of periodical signals through Fast Fourier Transforms (FFTs; Dimoudi et al., 2018) and Fast Folding Algorithms (FFAs; Morello et al., 2020), a return to the single pulse search was motivated by McLaughlin and Cordes (2003) and Cordes and McLaughlin (2003) in an attempt to find more sources. In 2006, this finally led to the discovery of the "rotating radio transients" (RRATs) –sources of short and bright radio pulses that are thought to be a subset of pulsars with higher pulse-to-pulse variability. The latter explains why they were more readily discovered through single pulse searches rather than in FFT searches (see McLaughlin et al., 2006)–.

A year later, all these efforts led to the unexpected discovery of the first FRB, identified as FRB 010724 (and also known as the "Lorimer burst", see Figure 1.2; Lorimer et al., 2007), during a single-pulse search of archival data recorded by the Parkes telescope. This burst was astonishing not only by its intensity (of monochromatic flux density, $F_\nu > 30$ Jy) but also for its high dispersion measure (DM; see Subsection 1.2.1) $\approx 375\,\mathrm{pc\,cm^{-3}}$, which was ~ 8 times higher than the contribution expected from the Milky way along the line of sight. Such DM implied an extragalactic origin and a high luminosity for this event.

In 2011, several man-made (terrestrial) symmetric radio signals of duration $> 20\,\mathrm{ms}$ and imperfect dispersive sweeps of DM $\sim 400\,\mathrm{pc\,cm^{-3}}$ were detected during searches among the archival data of Parkes Telescope. These detection resembled the spectral characteristic of the, at that moment, very recent Lorimer burst. As a consequence, some astronomers speculated that the Lorimer burst could be artificial too (Burke-Spolaor et al., 2011).

Strong new support in favor of FRBs as a real astrophysical phenomenon came from Thornton et al. (2013), who detected four new events (that we dubbed here as "Thornton bursts") using the High Time Resolution Universe survey at the Parkes telescope (HTRU; Keith et al., 2010). All Thornton bursts presented properties similar to those of the Lorimer burst, but with a much larger and (apparently) randomly-distributed DM. They adhere to a dispersive sweep to high precision; three (of the four) bursts are shorter in time by a factor of > 3 than all known perytons; furthermore, one of them (FRB 110220) showed a fast-rise and exponential-tail profile, making a clear case for cold plasma propagation (see Subsection 1.2.3). Is worth to note that all Thornton bursts were only detected in a single beam, while perytons were detected by all the beams of the Parkes' 13-beam receiver. Given these evidence, Thornton et al. (2013) concluded that FRBs were not obvious analogs of perytons, so they could have a celestial rather than a terrestrial origin, thus implying there is a population of extragalactic radio sources producing these events.

In the mean time, Petroff et al. (2015b) showed that perytons were produced by the microwave ovens of Parkes observatory with a bimodal DM distribution around ~ 200 and $400\,\mathrm{pc\,cm^{-3}}$. They also demonstrated that the Lorimer burst could not be a peryton since, at the time of its detection, the receivers of Parkes were pointing to a blocked region for the location of the microwave ovens. In addition, they showed that perytons do not perfectly mimic a genuine DM dispersive sweep and that they are not consistent with the properties of scattering trough cold plasma observed in one FRB. This way, Petroff et al. (2015b) demonstrated that FRBs are likely extragalactic transients.

After the discovery of Thornton et al. (2013) and the publication of Petroff et al. (2015b), a major interest was put on FRBs given their more reliable astrophysical origin, their fast-transient nature, and high luminosity ($\sim 10^{42}$ erg/s; see Subsection 1.2.8), which can be related with high-energy events and cataclysmic mechanisms (for a complete catalog of theories see Platts et al., 2018). As a consequence, searches for FRBs were carried by several telescopes around the globe, such as the Canadian Hydrogen Intensity Mapping Experiment (CHIME, Boyle and Chime/Frb Collaboration, 2018); the Upgraded Molonglo Synthesis Telescope (UTMOST, Caleb et al., 2016); the Arecibo Telescope Spitler et al., 2014 ; the Green Bank Telescope (GBT, Masui et al., 2015); The Australian Square Kilometre Array Pathfinder (ASKAP, Bannister et al., 2017); and others. This resulted in the discovery of so far ~ 100 FRBs (for a complete online-catalog of the registered FRBs see Petroff et al., 2016).

Worthy of note that, to date, there is no strict formalism to classify determined signals as FRBs. In practice, this means that there is a loose criteria which includes pulse duration, broadbandedness, brightness, and in particular whether the signal's DM is larger than the maximum Galactic contribution, $\mathrm{DM_{MW}}$. As consequence, events with DM close to $\mathrm{DM_{MW}}$ might be ambiguously classified as FRB or Galactic pulsar/RRAT (see Figure 1.1; Spitler et al., 2014 and Petroff et al., 2019).

Among the actual FRB population, there are important events, like the detection of the first repeating FRB 121102 (Spitler et al., 2014, Spitler et al., 2016), which led to milli-arcsecond localization and, consecutively, to the association of the progenitor of this

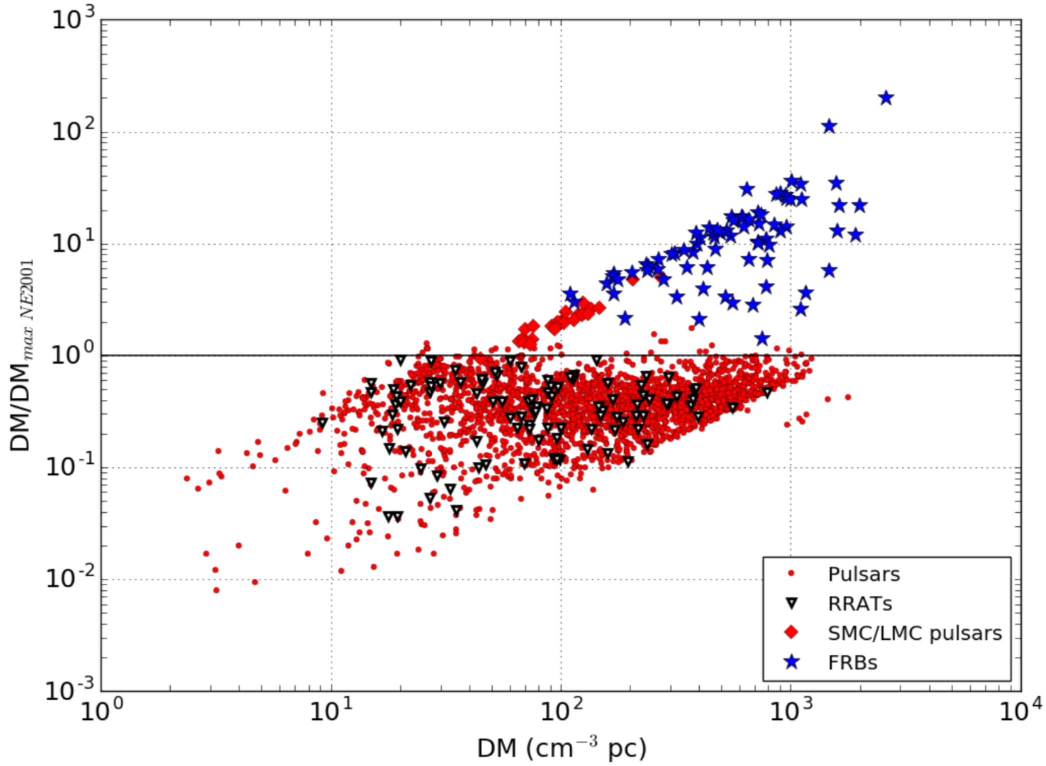

Figure 1.1: Dispersion measure (DM) of Galactic pulsars, RRATS, radio pulsars in the Small and Large Magellanic Clouds, and some of the published FRBs in comparison with the modeled maximum $\mathrm{DM_{MW}}$ along each respective line of sight from the NE2001 model (Cordes and Lazio, 2002). Sources with $\mathrm{DM/DM_{MW}} > 1$ are thought to be extragalactic. Figure from Petroff et al. (2019), based on an earlier version presented in Spitler et al. (2014).

FRB with a persistent radio source within a low-metallicity, irregular, dwarf ($\sim 10^8\,M_\odot$) galaxy at $z = 0.193$ ($\sim$ 1Gpc; see Chatterjee et al., 2017, Marcote et al., 2017, Tendulkar et al., 2017, Adachi and Kasai, 2012). This detection was highly revealing, not only because of presenting strong support to the extragalactic origin of FRBs (and its implications over their energetic properties), but also because of its implications when constraining theory –repetitions rule out any cataclysmic-like event to produce all the FRBs–. Moreover, whichever the progenitor, it must be able to provide energy for at least, until now, 8 years. After that, $\sim$ hundred FRBs have been detected, and 20 of them has been observed to repeat (CHIME/FRB Collaboration et al., 2019a, CHIME/FRB Collaboration et al., 2019c, Kumar et al., 2019 Fonseca et al., 2020). In addition, 3 one-off FRBs (Bannister et al., 2019 Ravi et al., 2019 Prochaska et al., 2019), and one repater source (FRB 180916.J0158+65;

Marcote et al., 2020) have been localized into higher-metallicity, massive ($\sim 10^{10}$–$10^{11}\ M_\odot$) elliptical or star-forming galaxies.

Another important event was the recent discovery of a Mega-Jansky FRB 200428 (The CHIME/FRB Collaboration et al., 2020, Bochenek et al., 2020). FRB 200428 was quickly associated with an X-ray bursts from the galactic magnetar SGR 1935+2154 ($\sim$ 10kpc away, and $1-10$ kyr old; see Kothes et al., 2018, Mereghetti et al., 2020). Soon after, much fainter FRB-like detections were done by the FAST telescope ($F_\nu \sim 30$ mJy at $\nu = 1.25$ GHz; Zhang et al., 2020), and others ($F_n u \sim 100$ Jy and $F_n u \sim 20$ Jy, at 1.3 GHz; Kirsten et al., 2020). This brand new connection clearly proposes magnetars as the progenitor of at least some of the FRB population (see Mereghetti et al., 2020), and give us new information about the possible emission mechanism for FRBs (see Bochenek et al., 2020).

Other highlights include: Polarization profile measurements of some FRBs (Petroff et al., 2015a, Masui et al., 2015, Michilli et al., 2018, Caleb et al., 2018, CHIME/FRB Collaboration et al., 2019a, CHIME/FRB Collaboration et al., 2019c, Chawla et al., 2020). Also, the detection of a downward frequency drift within a fraction of the bursts from repeateating sources (see Hessels et al., 2018,CHIME/FRB Collaboration et al., 2019a, CHIME/FRB Collaboration et al., 2019c)

1.2 Main properties and order-of-magnitude estimates of FRBs

The extragalactic origin of FRBs implies they will inevitably pass through matter at the vicinity of their local source –e.g., the accretion disk of a binary system (likely containing a compact star or black hole), a supernova remnant (SNR), or pulsar/magnetar nebula, depending on the model–, the interstellar medium (ISM) of their host galaxy, the IGM, our galaxy ISM and even our atmosphere. As a consequence, the EM pulse interacts with the plasma along the line of sight, leading to propagation effects such as dispersion, Faraday rotation and scattering. The first two effects are quantified with the dispersion measure (DM), and rotation measure (RM).

The aim of this section is to establish a theoretical background about the key observed properties of FRBs in order to infer their likely energy range, physical mechanisms and potential progenitors. For additional information see Katz (2016), Katz (2018b), Petroff et al. (2019), and Lorimer and Kramer (2004).

1.2.1 Dispersion measure as distance indicator and more

As mentioned above, FRBs share the common property of having a highly dispersed signal. This dispersion can be explained by a frequency-dependent group velocity, v_g, among the waves traversing a cold plasma. The amount of dispersion can be observationally quantified by the time delay of the pulse as function of the observing frequency as

$$\Delta t = \int_0^d \mathrm{d}l \left(\frac{1}{v_g(\nu_1)} - \frac{1}{v_g(\nu_2)} \right) = \int_0^d \frac{\mathrm{d}l}{c} \left[\left(1 - (\nu_p/\nu_1)^2\right)^{-1/2} - \left(1 - (\nu_p/\nu_2)^2\right)^{-1/2} \right] \tag{1.1}$$

where ν_1 and ν_2 are two different observing frequencies, we used $v_g = c\sqrt{1-(\nu_p/\nu)^2}$, l is a path length, d is the distance from here to the emitting source, c is the speed of light, $\nu_p = \sqrt{e^2 n_e/\pi m_e} \simeq 8.5\,\mathrm{kHz}\,(n_e/\mathrm{cm}^{-3})^{1/2}$ is the definition of the plasma frequency, $e\,(-e)$ is the proton (electron) charge, n_e is the electron number density, and m_e is the electron mass.

For $\nu_p \ll \nu$, we find

$$\Delta t = \frac{e^2}{2\pi m_e c} \left({\nu_1}^{-2} - {\nu_2}^{-2}\right) \mathrm{DM} \approx 4.15\,\mathrm{ms} \left[\left(\frac{\nu_1}{1\,\mathrm{GHz}}\right)^{-2} - \left(\frac{\nu_2}{1\,\mathrm{GHz}}\right)^{-2} \right] \left(\frac{\mathrm{DM}}{1\,\mathrm{pc\,cm^{-3}}}\right), \tag{1.2}$$

where DM is the dispersion measure, whose definition is

$$\mathrm{DM} \equiv \int_0^d n_e(l)\,\mathrm{d}l. \tag{1.3}$$

As exemplified by the Lorimer burst from Figure 1.2, the time delay from the observed FRBs follow $\Delta t \propto \nu^{-2}$ with high precision, which is highly consistent with radiation traversing cold plasma under the approximation $\nu_p \ll \nu$.

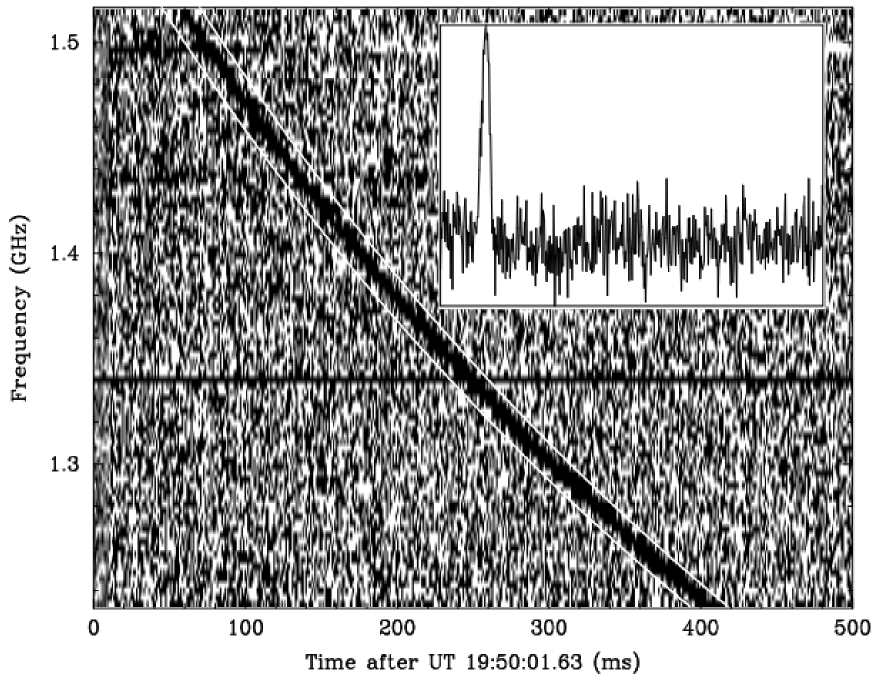

Figure 1.2: Two-dimensional plot of intensity as function of radio frequency versus arrival time of the Lorimer Burst (FRB 010724). The time-dispersion of the signal is clearly seen as a quadratic sweep across the frequency band, with broadening towards lower frequencies, being this consistent with a propagation through cold plasma with $DM = 375 \pm 1\,\mathrm{pc\,cm^{-3}}$ (see subsections 1.2.1 and 1.2.3). The horizontal line at ~ 1.34 GHz is an artifact in the data caused by a malfunctioning frequency channel. Figure from Lorimer et al. (2007).

Now, the DM can be expanded as

$$\mathrm{DM} = \mathrm{DM_E} + \mathrm{DM_{MW}}, \tag{1.4}$$

where $\mathrm{DM_{MW}}$ is the dispersion contribution from our galaxy, which can be obtained from electron density models such as NE2001 (Cordes and Lazio, 2002) and YMW16 (Yao et al., 2017), and $\mathrm{DM_E}$ is the dispersion measure excess

$$\mathrm{DM_E} = \mathrm{DM_{IGM}}(z) + \frac{\mathrm{DM_{Host}}}{1+z}. \tag{1.5}$$

In this last expression, $\mathrm{DM_{Host}}$ is the host galaxy contribution and the factor $(1+z)$ accounts for cosmological time dilation, and $\mathrm{DM_{IGM}}$ is the intergalactic dispersion, whose mean contribution is

$$\overline{\mathrm{DM}}_{\mathrm{IGM}} = \int n_{e,\mathrm{IGM}} \mathrm{d}l = K_{\mathrm{IGM}} \int_0^z \frac{(1+z)x(z)\mathrm{d}z}{\sqrt{\Omega_m(1+z)^3 + \Omega_\Lambda}} \simeq 1000\, z\, \mathrm{pc\,cm^{-3}}, \tag{1.6}$$

which is obtained assuming all baryons are homogeneously distributed. Here, $x(z)$ is the IGM ionization fraction ($\simeq 7/8$ at low redshift), $K_{\mathrm{IGM}} = 933\mathrm{pc\,cm^{-3}}$ assumes standard Planck cosmological parameters and a baryonic mass fraction of 83% (Yang and Zhang, 2016), and Ω_m and Ω_Λ are, respectively, the energy densities of matter and dark energy. Note that the rightmost equality of equation (1.6) is obtained taking a low-redshift approximation (which is valid for our interests).

As last step, this redshift estimate can be converted into luminosity distance, D_L, using the expansion expression in Taylor series in redshift z, $D_L \simeq 2z(z+2.4)$ Gpc, which is valid for $z < 1$ (Chiba and Nakamura, 1998, Petroff et al., 2019). This way, $\mathrm{DM_E}$ acts as an upper limit for $\mathrm{DM_{IGM}}$ that can be used to constrain the luminosity distance as follows (see also Deng and Zhang, 2014, Yang and Zhang, 2016 and Adachi and Kasai, 2012):

$$D_L < \left(\frac{\mathrm{DM_E}}{500\,\mathrm{pc\,cm^{-3}}}\right)\left[2.4 + \left(\frac{\mathrm{DM_E}}{1000\,\mathrm{pc\,cm^{-3}}}\right)\right] \mathrm{Gpc}. \tag{1.7}$$

As we can see from Figure 1.3 (Shannon et al., 2018), leaving aside the repeater FRB 121102 case, the excess of dispersion of the FRB population is $\gtrsim 100\,\mathrm{pc\,cm^{-3}}$, which implies constraints on the luminosity distance $\gtrsim 100\,\mathrm{Mpc}$. In addition, this figure shows that the FRB population from Parkes and ASKAP telescopes is consistent with $\mathrm{DM_E}$ as distance indicator since the Parkes bursts (black dots) might present themselves as a more distant versions of the ASKAP events (blue dots). See (Shannon et al., 2018) for further details.

DM: Some other uses

Provided we can dissentagle DM contribution of the IGM from the rest (ISM and local), plus an independent redshift or distance estimation, a DM measurement can be used to probe the properties of the IGM. This has been already done using FRBs (see Macquart

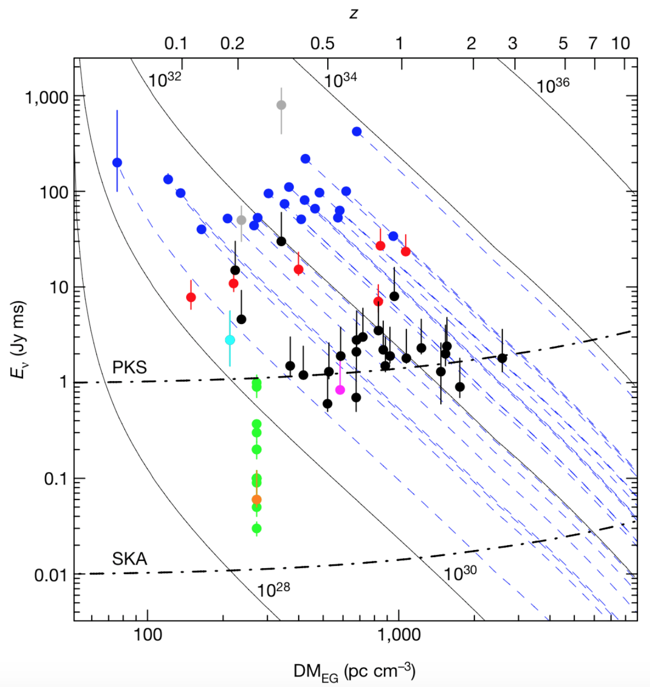

Figure 1.3: The figure shows the fluence (E_ν) against the extragalactic dispersion measure, $\mathrm{DM_{EG}}$ (equal to our $\mathrm{DM_E}$), for FRBs detected with the ASKAP (blue dots), Parkes (black dots), UTMOST (red dots), Green Bank Telescope (magenta dot) and Arecibo (orange dot) radio telescopes. The figure also shows a cyan dot for the candidate FRB 010621, and the beam-corrected fluences of two Parkes FRBs (grey dots). Repeated pulses from FRB 121102 are displayed in green. In addition, the upper horizontal axis shows redshift, assuming a homogeneously distributed intergalactic plasma and a host contribution of $50(1+z)^{-1}$. The blue dashed curves show extrapolation to larger distances of the expected fluence from the ASKAP-detected bursts. As order-of-magnitude reference, the black curves shows contours of constant spectral-energy density (in units of erg Hz^{-1}). The dash-dotted black curves are lines of constant fluence after accounting redshift-dependent time dilation. Figure from Shannon et al. (2018).

et al., 2020).

In addition, again assuming a correct disentanglement, $\mathrm{DM_{Local}}$ and $\mathrm{DM_{Host}}$ can be used to distinguish between progenitor models for FRBs since these two strongly depend on the properties of the local plasma and the host galaxy type.

1.2.2 Rotation measure (RM) as magnetized source indicator

As explained in Lorimer and Kramer, 2004 (Chapter 4), the interaction of a EMW and a magneto-ionized plasma leads to a different dispersion relation for right- and left-handed circular polarized EMWs. As a result of this, their group velocities are

$$v_{R,L}(\nu, B_{\|}, n_e) = c\sqrt{1 - \frac{{\nu_p}^2}{\nu^2} \mp \frac{{\nu_p}^2 \nu_B}{\nu^3}} \approx c\left[1 - \frac{{\nu_p}^2}{2\nu^2}\left(1 \mp \frac{\nu_B}{\nu}\right)\right], \tag{1.8}$$

where $B_{\|}$ is the component of the plasma magnetic field parallel to the wave vector $\vec{k}$, and $\nu_B = eB_{\|}/2\pi m_e c \simeq 3\,\mathrm{MHz}\,(B_{\|}/\mathrm{G})$ is the cyclotron frequency related to $B_{\|}$. Note that we assumed $\nu_p \ll \nu$ and $\nu_B \ll \nu$ to obtain the approximation in the last part of this equation.

As an observational consequence, a linearly polarized wave (a superposition of a right- and left- circular wave) would present a rotation of its linear polarization plane, whose polarization position angle (PPA) is then

$$\Theta = \mathrm{RM}\,\lambda^2 + \Theta_0, \tag{1.9}$$

where Θ_0 is the initial PPA, and RM is the Faraday rotation measure (or just rotation measure), which is defined as

$$\mathrm{RM} \equiv \frac{e^3}{2\pi m_e^2 c^4}\int_0^d n_e B_{\|} \mathrm{d}l \approx 812\,\mathrm{rad\,m^{-2}}\int_0^d \left(\frac{n_e}{\mathrm{cm^{-3}}}\right)\left(\frac{B_{\|}}{\mu\mathrm{G}}\right)\left(\frac{\mathrm{d}l}{\mathrm{kpc}}\right). \tag{1.10}$$

Note that the sign of RM gives the direction of the magnetic field (by convention RM > 0 implies a magnetic field directed towards the observer).

Figure 1.4 shows the measured Stokes parameters, U/L and Q/L, of the repeating FRB 121102, whose RM is particularly high ($\sim 10^5\,\mathrm{rad\,m^{-2}}$). The results exhibit a good fit of the measured parameters with the theory related to Faraday Rotation (where $Q/L = \cos(2\Theta)$ and $U/L = \sin(2\Theta)$). Note, however, that FRB 121102 is not necessarily representative of the FRB population. Only a relatively small fraction of the published FRBs have measured polarization profiles, including some FRBs consistent with $\mathrm{RM_{local}} \sim 0$ (see for example Ravi et al., 2016, Petroff et al., 2017, Caleb et al., 2018, CHIME/FRB Collaboration et al., 2019c, and others).

We note that RM, like DM, can be decomposed into contributions from different regions, but to disentangle them correctly is more complicated than in the DM case, since magnetic field variations along the line of sight can add or cancel each other's RM contributions.

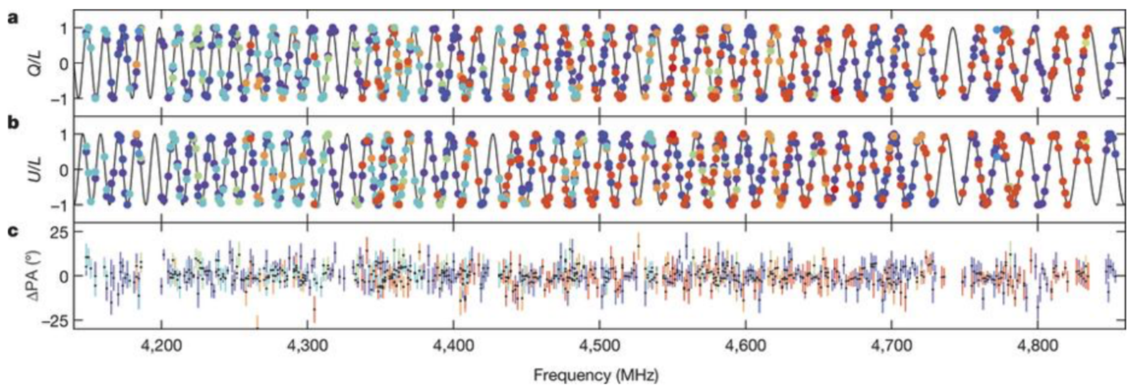

Figure 1.4: The figure shows the Faraday rotation seen in FRB 121102. Panels (a) and (b) show the values of the normalized Stokes Q and U parameters of the polarized signal across its observed frequency. Panel (c) shows the residual of the polarization angle compared to a Faraday rotation model. Colored dots in the figure represent measurements from different bursts detected in the same observing session. Figure from Michilli et al. (2018).

Now, since the IGM may provide a small RM contribution ($< 10\,\mathrm{rad\,m^{-2}}$, Ravi et al., 2016) and the Galactic contribution can be modeled (Oppermann et al., 2015), we might be able to relate the RM (and its potential variability) to the local environment of the source. A good example of this is the case of the repeating FRB 121102, whose extremely high RM $\sim 10^5\,\mathrm{rad\,m^{-2}}$ has decreased 10% over a time-scale $\sim$ 7 months. As Michilli et al. (2018) claim, this large and variable rotation measure could imply that FRB 121102 is in an extreme and dynamic magneto-ionic environment which (along with the bursts timescales, see Subsection 1.2.8) suggest an origin related to the vicinity of a massive black hole, a neutron star, or both.

From the measurement of the DM and the RM, we can estimate the average magnetic field of the local environment weighted by the electron number density along the path length:

$$\langle B_\parallel \rangle \equiv \frac{\int_0^d n_e B_\parallel \mathrm{d}l}{\int_0^d n_e \mathrm{d}l} \approx 1.23\,\mu\mathrm{G}\left(\frac{\mathrm{RM}}{\mathrm{rad\,m^{-2}}}\right)\left(\frac{\mathrm{DM}}{\mathrm{pc\,cm^{-3}}}\right)^{-1}. \tag{1.11}$$

In the case of FRB 121102, this leads to a lower limit estimate of the (likely local to the source) line-of-sight magnetic field $\langle B_\parallel \rangle = (0.6-2.4) f_{\mathrm{DM}}\,\mathrm{mG}$. In the latter expression, the range is due to an inferred $\mathrm{DM_{Host}} \sim 70 - 270\,\mathrm{pc\,cm^{-3}}$ (Tendulkar et al., 2017), where $f_{\mathrm{DM}} \equiv \mathrm{DM_{Host}}/\mathrm{DM_{RM}} \geqslant 1$ since the dispersion measure contribution specifically related to the observed rotation measure ($\mathrm{DM_{RM}}$) could be much smaller than the total dispersion measure contribution of the host ($\mathrm{DM_{Host}}$). For comparison, typical magnetic fields within our ISM are only $\sim 5\,\mu$G (Haverkorn, 2015), which is in agreement with inferring that the source of the repeating FRB 121102 could be embedded within a highly magnetized environment (see Michilli et al., 2018).

1.2.3 Scattering as indicator of turbulence and inhomogeneity

Following Lorimer and Kramer (2004) (chapter 4), scattering can be (more easily) understood when considering a thin screen model between observer and source. This screen concentrates all possible inhomogeneities (of length $\sim a$ and electron density fluctuations $\sim \Delta n_e$) along a distance D between them. The inhomogeneities lead to a bending of the wavefront by an angle θ_s, which can finally be quantified in terms of an exponential decay of the FRB radiation as a function of time. This exponential decay over time can be explained by the geometric time delay between the straight and the deflected waves, whose characteristic timescale is

$$\tau_{scatt} \sim \frac{\theta_s^2 D}{c} \propto \frac{\Delta n_e^2 D^2}{a} \nu^{-4}. \tag{1.12}$$

Note that, in reality the variations in electron density show a distribution of scales rather than a single size. For this reason, a more detailed and used model of scattering is the "Kolmogorov spectrum", for which $\tau_{scatt} \propto \nu^{-\beta}$, and where $\beta = 4.4$ is its scattering index (Lorimer and Kramer, 2004).

Thus, scattering is a strongly frequency-dependent propagation effect. As Equation (1.12) makes clear, the main observable property of a scattered signal is its exponential tail widening, but this also means that the flux becomes smoother as the frequency decreases. Because of the latter, although debated (Sokolowski et al., 2018), it is known that scattering could make difficult to detect FRBs at very low frequencies ($\lesssim 1\,$GHz). We must highlight that observed FRBs are consistent with the picture of scattering described above for the thin screen model ($\beta = 4$) and the Kolmogorov spectrum ($\beta = 4.4$), as Thornton et al. (2013) obtained $\beta = 4 \pm 0.4$, Shannon et al. (2018) measured $\beta = 3.5 \pm 0.6$, and Masui et al. (2015) estimated $\beta = 3.6 \pm 1.4$ (see also Figure 1.5).

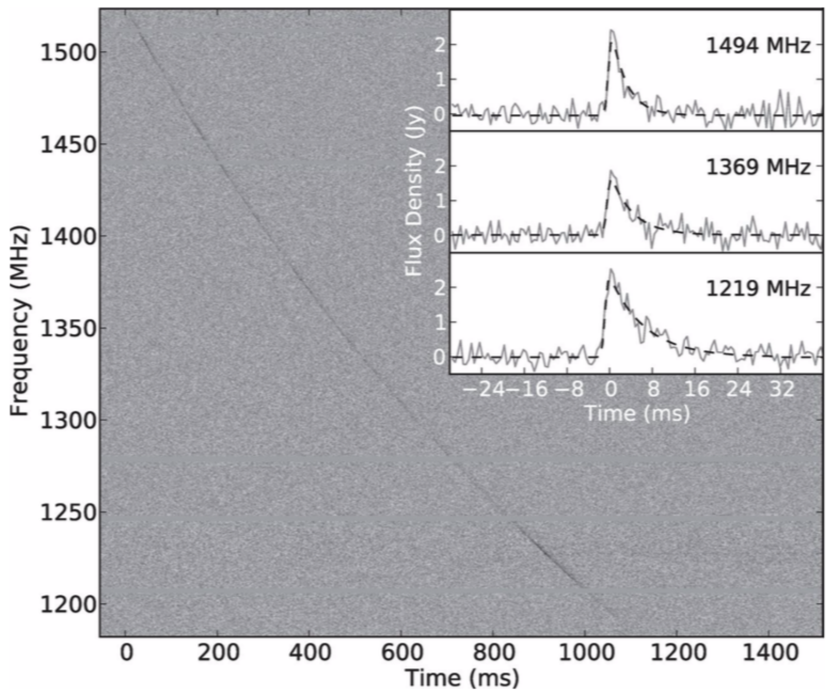

Figure 1.5: The main panel shows the dynamic spectrum of FRB 110220 along with its clear dispersive sweep. The three mini-panels on right top show the exponential decay of the signal as a function of time observed at different frequencies. From the figure is also possible how the exponential decay is broadened towards lower frequencies. Figure from Thornton et al. (2013).

Equation (1.12) also tells us that $\tau_{scatt} \propto \Delta n_e^2$. Thus, scattering measurements can be used to study inhomogeneities and turbulence of the ionized material along the line of sight. Regarding this idea, some authors observed that the FRB population has less scattering than predicted from the Galactic DM/scattering trend (see Cordes et al., 2016, Xu and Zhang, 2016, and CHIME/FRB Collaboration et al., 2019b), which can be explained by a low scattering contribution of the IGM (compared to its inferred high DM contribution, see Macquart and Koay, 2013 and Zhu et al., 2018).

CHIME/FRB Collaboration et al. (2019b) recently reported FRBs between $0.4 - 0.8$ GHz that have more scattering than expected from our Galactic ISM. From this, they suggest that FRBs may come from overdense regions with stronger scattering properties than the quiescent diffuse ISM, as very young SNRs, star-forming regions, or galactic centers. However, other FRBs in the new CHIME sample have very narrow pulse widths (as low as $\sim 0.1\,$ms) at these frequencies (where scattering is expected to be stronger). To date FRBs have been observed down to 300 MHz (see Chawla et al., 2020, Pilia et al., 2020) in at least one source, suggesting that some of their circumburst environments could have weak scattering properties (Chawla et al., 2020). In any case, the origin of the unscattered events is still an open question.

1.2.4 Scintillation

Again following Lorimer and Kramer (2004), scintillation is interpreted as short-term intensity variations seen on the radio signal of some sources, like pulsars. These intensity variations can be understood in terms of the model of scattering explained before. The delay imparted by the refractive and diffractive effects as the signal passes through a clumpy and turbulent environment produces a variety of phases within a range $\delta\Phi \sim 2\pi\Delta\nu\,\tau_{scatt}$. Thus, once the waves come back together, constructive and destructive interference patterns (over the time τ_{scatt} and a bandwidth $\Delta\nu$) are produced if the phase of the waves do not differ by more than 1 radian:

$$2\pi\Delta\nu_d\,\tau_{scatt} \sim 1\,\mathrm{rad}. \tag{1.13}$$

As a consequence, there is a limitation in bandwidth of the interfering waves, which is called "the decorrelation bandwidth", $\Delta\nu_d \propto \tau_{scatt}^{-1} \propto \nu^4$ (interference could be seen on frequency scales $\lesssim \Delta\nu_d$). This produces a complex frequency structure of the radiation that also varies with time, given the relative motion of the observer, source and scattering screen.

Given their small source size and large distances (see Subection 1.2.8; Michilli et al., 2018 and Tendulkar et al., 2017), FRBs should be point-like sources; as a consequence, they will scintillate unless they present a significant angular broadening of the source. Scintillation could have been observed in some FBRs like FRB 121102, whose frequency structure has been proposed to be attributed to scintillation from our Galaxy (Gajjar et al., 2018). In the case of FRB 150807, the observed scintillation is speculated to be produced by weak scattering in the IGM or host galaxy (Ravi et al., 2016). A final interesting case is FRB 110523, whose measured scattering time $\approx 1.66 \pm 0.14\,\mathrm{ms}$ and decorrelation bandwidth $\approx 1.2 \pm 4\,\mathrm{MHz}$ can only be explained by two scattering screens (one located within 44 kpc of the source, and the other within our Galactic ISM, see Masui et al., 2015).

We need to remark that scintillation can give us important information about the magnitude of fluctuations, turbulence and the location of scattering screens, and therefore, potential insights about the possible progenitor of FRBs. However, this has to be carefully studied since some spectral features could be related to propagation or to broad- or narrow-band impulsive "radio frequency interference" (RFI), and thus, not being intrinsic to the emission mechanism.

1.2.5 Plasma lensing

Similarly as described for scattering, any refractive medium (e.g. plasma) can act as a lens. Thus, plasma structures has the potential to bend the radio waves to finally produce bright, time-dependent, and highly monochromatic caustic spots (Clegg et al., 1998).

Plasma lensing has been convincingly demonstrated in the Crab pulsar (whose filaments have an estimated radii $\sim 1\,\mathrm{AU}$ which can contribute DM $\sim 1\mathrm{pc\,cm^{-3}}$, see Backer et al., 2000 and Graham Smith et al., 2011) and more recently in the Black Widow pulsar B1957+20 (produced by intra-binary plasma that has been blown off the pulsar's companion star, see Main et al., 2018). Considering this and previous insights from scattering and scintillation produced in the close and intermediate vicinity of some FRB sources, it has been proposed that FRBs could also present plasma lensing features in their spectra (produced, for example, by a young SNR, a nebula or any high density environment).

Cordes et al. (2017) studied the potential effects of plasma lensing over FRBs since it can mask the spectra and energetic properties of any source. Plasma lensing could reduce $\lesssim 100$ times the energy of FRBs bursts and might explain the highly variable radio spectra seen in the repeating FRB 121102 (Cordes et al., 2017). In addition, it has been also recalled to explain the time-frequency downward drifting (quantified by the "frequency drift", see the last part of Subsection 1.2.7) of the repeating FRB 121102 (Hessels et al., 2018). However, frequency drift from plasma lensing is supposed to be symmetric in time, while FRB 121102, FRB 180814.J0422+73 (the second repeater; CHIME/FRB Collaboration et al., 2019a), and others, present only descending time-frequency structures. In that sense, the relevance of plasma lensing for FRBs becomes less clear (although it could be tested with ultra-wide-band observations from $\sim 0.1 - 10\,\mathrm{GHz}$, Cordes et al., 2017).

1.2.6 Free-free absorption

Another important effect we need to consider is the absorption of energy by the ionized plasma along the line of sight of propagation path. The free-free optical depth can be expressed as (Draine, 2011 and Margalit et al., 2018)

$$\tau_{ff} = 0.018\, Z^2 \nu^{-2} \int T^{-3/2}\, n_i\, n_e\, \overline{g}_{ff}\, \mathrm{d}r. \tag{1.14}$$

where T is the temperature of the environment, n_e and n_i are the electron and ion number density, $\overline{g}_{ff}$ is the velocity averaged Gaunt factor, and Z is the atomic number of the plasma.

Equation (1.14) tell us that radio wave opacity is dependent of the thermal, ionization and density state of the emitting source, along with a dependence of the observing frequency. This become particularly important when considering low-frequency radiation ($\lesssim 1\,\mathrm{GHz}$) passing through dense environments (like a SNR or star forming regions). Regarding this, radio transparency requirements for FRBs against free-free absorption are being used to put constraints on the age of SNRs as possible progenitors of these events (see Margalit et al., 2018).

To date, despite large efforts and very optimistic detection predictions for LOFAR and MWA telescopes (Hassall et al., 2013), no FRB has been detected below ~ 300 MHz. While this could be explained by the intrinsic spectra of FRBs or scattering effects, the strong frequency dependence of the free-free optical depth ($\propto\ \nu^{-2.1}$ for more detailed models) might also be a contributing factor. Since all the discussed propagation effects are strongly dependent on the observing frequency, a large sample of events is needed to disentangle the relevant factors to explain the lack of detections at these low frequencies.

1.2.7 Intrinsic spectra

As we have discussed previously, FRB signals could be highly masked by propagation effects (e.g. scattering, free-free absorption, etc.), so the correct disentangling of each in order to make a correct analysis of the intrinsic spectra of FRBs is not a trivial task. Additional complications arise from observational constraints, such as the small available observing bandwidth, and the (generally) poor localization of FRBs within telescope beams, which is at least of several arcminutes. As a consequence, the spectral index of FRBs, α (from the flux density definition $F_\nu \propto \nu^\alpha$), is poorly constrained.

From broad-band spectral analysis, some of the most stringent constraints on the spectral index come from non-detections of FRBs at low frequencies. For example, Chawla et al. (2017) proposed $\alpha > -0.9$ from previous non-detections at GBT (at 0.35 GHz), and Karastergiou et al. (2015) propose $\alpha > +0.1$ from non-detections at LOFAR (at 0.145 GHz). Law et al. (2017), during a multi-telescope observing campaign on the repeater FRB 121102, obtained $\alpha = 2.1$ from Arecibo (1.4 GHz)-VLA (3 GHz) telescope observations, and $\alpha < -1.4$ from VLA-Effelsberg (4.5 GHz) (along with other similar constraints, see Figure 1.6). In addition, Macquart et al. (2019) obtained $\alpha \approx -1.5^{+0.3}_{-0.2}$ from a recent study of the ASKAP FRBs.

The previously mentioned constraints are clearly in disagreement. Because of this, it has been proposed that the spectra of FRBs could present intrinsic (related to the emission mechanism) or extrinsic (related to propagation effects) turnovers, or that they may not follow a power law at all, but that they are better represented by spectral emission envelopes (of $\sim 500\,\mathrm{MHz}$ wide, see Law et al., 2017, Gourdji et al., 2019 and Hessels et al., 2018).

Another important spectral feature of FRBs is the frequency drift –time-dependent changes on the observing frequency of the FRB sub-pulses as time progress–. It has been proposed that this feature could be related to the emission mechanism or propagation effects like plasma lensing. To date, frequency drifts has been measured only on repeating FRBs, e.g., $\sim -200\,\mathrm{MHz\,ms^{-1}}$ for FRB 121102 (Hessels et al., 2018), and $\sim -5\,\mathrm{MHz\,ms^{-1}}$ for FRB 180814.J0422+73 (CHIME/FRB Collaboration et al., 2019a). We note that, to date, the observed drifts are only negative (meaning that the peak frequency of each sub-

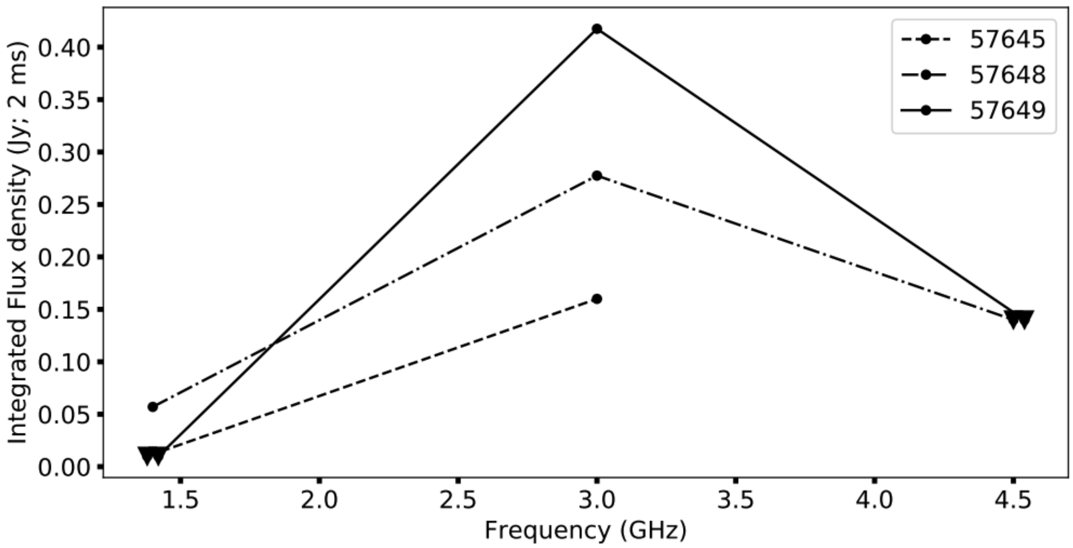

Figure 1.6: Broadband spectra measurements and limits for three bursts of FRB 121102 with observing coverage by VLA (3 GHz), Arecibo (1.4 GHz) or Effelsberg (4.5 GHz) telescopes. Measurements are show as dots and upper limits as triangles. Limits are estimated assuming pulse width = 2 ms and a 5σ detection threshold. Errors in flux density are comparable to symbol sizes and are not shown. Figure from Law et al. (2017).

pulse decreases with time; see Hessels et al., 2018 and CHIME/FRB Collaboration et al., 2019a). Since plasma lensing is expected to produce temporally symmetrical features, it has been proposed that the frequency drift on FRB 121102 and FRB 180814.J0422+73 would be better explained by the emission mechanism of FRBs (Metzger et al., 2019).

1.2.8 FRBs: Implications from luminosity and pulse width

Emitting source size

One of the first and easiest estimates we can do is to constrain the emitting source size using the expression for the light-crossing time ($t \sim R/c$) as

$$r_s \leq c\Delta t \approx 300\,\mathrm{km}\,\Delta t_{-3}, \tag{1.15}$$

where r_s is the estimated source size, $\Delta t \sim 1\,\mathrm{ms}$ is the pulse width of typical FRBs, $c = 3 \times 10^{10}\mathrm{cm\,s^{-1}}$ is the speed of light. Here, the inequality come because the light-crossing time considers the absolute minimum communication time between the spatial limits of an event. Note that a more general expression for this constraint is $r_s \leq c\Delta t\Gamma^2$, which considers beamed emission (into an angle $\approx 1/\Gamma$) from a relativistically expanding source with a Lorentz factor Γ (see Katz, 2014 and Luan and Goldreich, 2014). Hereafter, we employ the short-hand notation $q_x = q/10^x$ in cgs units, e.g., $L_{42} = L/(10^{42}\,\mathrm{erg\,s^{-1}})$.

It is highlighted that the estimation of the source size, r_s, from Equation (1.15) implies a relatively small source size which might be related to compact sources like neutron stars or stellar-mass black holes.

Luminosity and energy

As previously mentioned, the precise localization of FRB 121102 has helped identify its host galaxy and its extragalactic origin ($\sim 1\,\mathrm{Gpc}$), thus establishing the FRBs as a truly new class of extragalactic events.

Taking FRB 121102 as reference, we can estimate the instantaneous luminosity of FRBs as

$$L = 4\pi D^2 \nu F_\nu \sim 10^{42}\ \mathrm{erg\,s^{-1}}\, F_{\mathrm{Jy}}\, \nu_9\, D^2_{\mathrm{Gpc}}, \tag{1.16}$$

where D is the source distance from Earth, F_ν is the measured monochromatic flux, and ν is the radio frequency (usually $\sim 1\,\mathrm{GHz}$).

Considering an emission timescale $\Delta t \sim 1$ ms, we can estimate the total energy of this FRB as

$$\mathcal{E}_{FRB} = L\,\Delta t \sim 10^{39}\,\mathrm{erg}\, F_{\mathrm{Jy}}\, \nu_9\, D^2_{\mathrm{Gpc}} \Delta t_{-3}. \tag{1.17}$$

Then, the estimated energy of FRBs could be significantly lower than the kinetic energy released by supernovae (SNe, $\mathcal{E}_{SN} \sim 10^{51}$ erg; see Khokhlov et al. (1993)). In the case of neutron stars (NSs), with magnetic fields ranging $B_\star \sim 10^8 - 10^{15}\,\mathrm{G}$ and rotation periods ranging $P_\star \sim 10^{-3} - 10\,\mathrm{s}$ (see Manchester et al., 2005), their rotational energy budget is $\mathcal{E}_{\star,rot} \sim 10^{48}$ erg $P_{\star-1}^{-2}$, and their magnetic energy budget is $\mathcal{E}_{\star,B_\star} \sim 10^{43}$ erg $B_{\star 13}^2$. Thus, any NS could have enough rotational energy to produce a FRB, while only NSs with $B_\star > 10^{11}\,\mathrm{G}$ have enough magnetic energy to produce these events (see Murase et al., 2016). In any case, progenitors with $\gg 10^{39}\,\mathrm{erg}$ will be necessary since we know repeating FRB sources do exist.

Brightness temperature

The observed luminosity of FRBs give us insights related to their physical mechanism and/or their progenitor. For instance, following Katz (2014) and Lyutikov (2017), we can estimate the brightness temperature, T_{FRB}, of FRBs as

$$T_{FRB} \simeq 10^{36}\mathrm{K}\, F_{\mathrm{Jy}}\, \nu_9^{-2}\, \Delta t_{-3}^{-2}\, D_{\mathrm{Gpc}}^2 \tag{1.18}$$

where we assumed a black body equivalent luminosity for the FRB at the Rayleigh-Jeans limit.

The huge temperature from Equation (1.18) implies a coherent emission mechanism (see Figure 1.7), which needs the contribution of bunched particles radiating in phase within a relatively small space volume (see Katz, 2014). A corollary from this is that FRBs cannot be produced by thermal processes; and therefore, as was previously mentioned, they need to be produced by highly energetic processes like those involved in gamma ray bursts (GRBs), giant pulses (GPs) from pulsars, nano-shots (nanosecond subpulses observed within the Crab pulsar's GPs), and some others (see Hankins and Eilek, 2007, Katz, 2014, Lyutikov et al., 2016, and Margalit et al., 2018).

Electromagnetic field at the source

Another estimate that can be done is to calculate the electromagnetic field at the FRB source. Similar as Lyutikov (2017) did, we can estimate the electromagnetic field from the definition of the Poynting vector and its connection with the energy flux

$$|\vec{S}| \equiv \frac{c}{4\pi}|\vec{E}\times\vec{B}| = \frac{c}{4\pi}E^2 = \frac{L}{4\pi r^2} \equiv F, \tag{1.19}$$

where we assumed $B = E$. Then, evaluating at the estimated source size, $r \sim r_s$, we obtain

$$\begin{aligned} E_s \sim \frac{L^{1/2}}{c^{1/2} r_s} &\sim 10^8\,\mathrm{G}\, F_{\mathrm{Jy}}^{1/2}\, \nu_9^{1/2}\, D_{\mathrm{Gpc}}\, \Delta t_{-3}^{-1} \\ &= 10^8\,\mathrm{G}\, L_{42}^{1/2}\, \Delta t_{-3}^{-1}, \end{aligned} \tag{1.20}$$

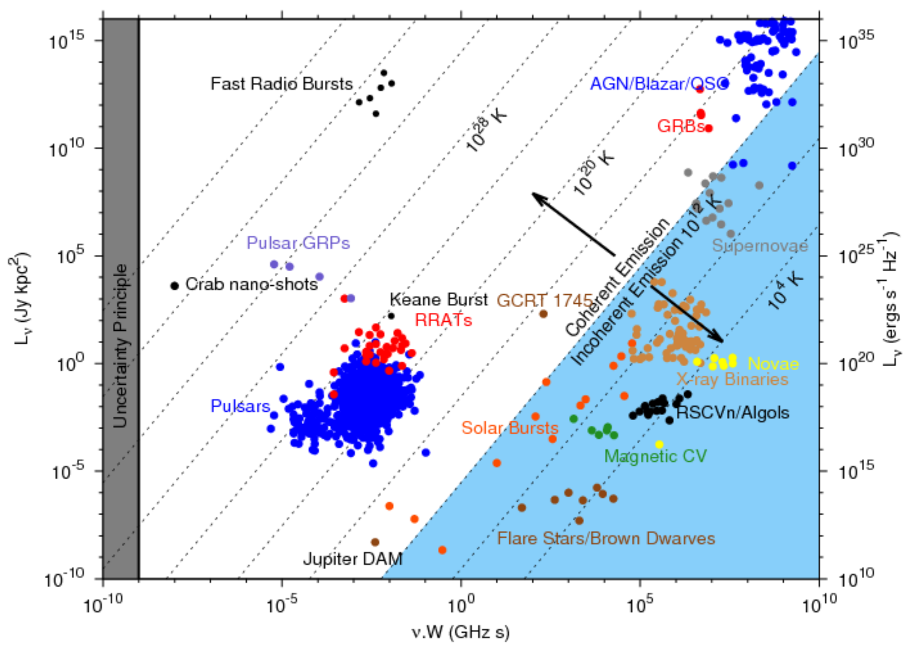

Figure 1.7: The present figure shows the monochromatic brightness ($L_\nu = L/\nu$) against νW (where W is the pulse width) of different types of astrophysical events. Despite there are no clear physical restrictions to classify coherent and incoherent astrophysical events, astronomers usually consider the temperature $T \sim 10^{12}\,\mathrm{K}\,(\nu/\mathrm{GHz})^{-1/5}$ to avoid the so-called "Inverse Compton catastrophe" (see Tsang and Kirk, 2007). Figure from Pietka et al. (2015).

where for simplicity we have normalized the FRB luminosity by $L_{42} = 10^{42}\,\mathrm{erg/s}$.

Therefore, an order-of-magnitude estimation of the magnetic field at the emission source (Equation 1.20) hints toward a highly magnetized progenitor. This, along with the small source size, high brightness temperature, high scattering, RM measurements, and constraints from the persistent radio source of FRB 121102 (Chatterjee et al., 2017), suggest that NSs are the most promising progenitors of FRBs, as has been already observed for one FRB source (see Pen and Connor, 2015, Lyutikov et al., 2016, Hessels, 2018 Masui et al., 2015, Beloborodov, 2017, The CHIME/FRB Collaboration et al., 2020, Bochenek et al., 2020, and Mereghetti et al., 2020).

Chapter 2

Particle acceleration

To accelerate a particle (of mass m and charge e) to light speed within a time comparable to a half of the wave cycle period, $\nu^{-1}/2$, it would be necessary to have an electromagnetic field of amplitude

$$E_{crit} \equiv 2mc\nu/e, \tag{2.1}$$

thus implying $E_{crit} \sim 300\,\mathrm{G}\ (\nu/1\mathrm{GHz})^{-1}$ for electrons, and $\sim 10^5\,\mathrm{G}\ (\nu/1\mathrm{GHz})^{-1}$ for protons. Since the estimated amplitude of the electromagnetic wave (EMW) near the FRB source (Equation 1.20) is several orders of magnitude larger, FRBs could be producing a big impact on the surrounding plasma close to the source.

In this work, we assume that a pre-FRB is triggered at the source, then that its energy is transported outwards and, eventually, converted into the coherent radiation of the FRB at a given location. Beyond this point, the FRB EMW will interact with its surrounding plasma (see Figure 2.1). The motivation of this work is to study the behavior of charged particles accelerated by a strong EMW in order to determine possible observational or theoretical constraints over FRBs and the local environment of their progenitors.

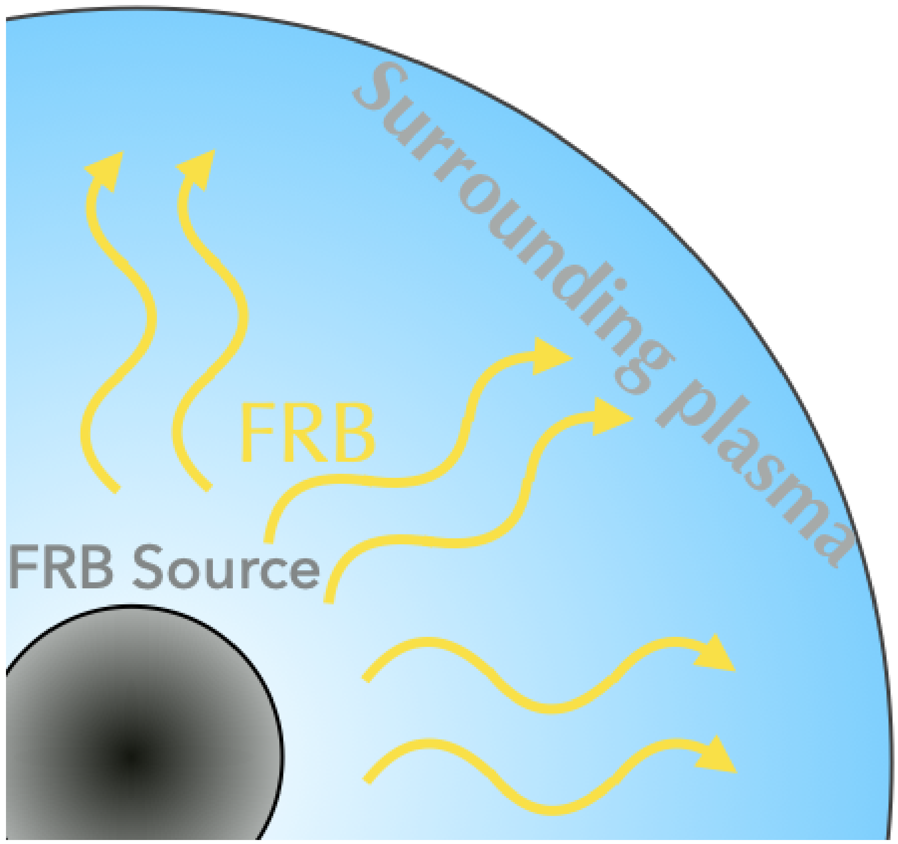

Figure 2.1: Representation of the assumed FRB emission scenario. We assume that a pre-FRB is triggered at the source (the FRB progenitor) due to an uncertain mechanism. Then, the pre-FRB energy is transported outwards and eventually converted (through a coherent emission mechanism) into the actual FRB signal at an uncertain location. Beyond this point, the FRB EMW will interact with its surrounding plasma (initially at rest).

2.1 Particle acceleration by an intense electromagnetic wave of constant amplitude

As a first step towards understanding the particle's movement, consider an electromagnetic wave with $\vec{E} = E\hat{y}$, $\vec{B} = B\hat{z}$ (where $E = B$), and wave vector $\vec{k} \equiv k\hat{k} = k\hat{x}$. This electromagnetic wave will interact with the particle a Lorentz force, given by

$$\vec{F} = e\left(\vec{E} + \frac{\vec{v}}{c} \times \vec{B}\right). \tag{2.2}$$

A particle at rest at $t = 0$ will first only interact with the electric field, accelerating in the direction of the electric field ($\hat{y}$). After that, the particle will no longer have null velocity, and therefore will be interacting with the magnetic field as well. Following the right-hand rule $\left(\hat{v} \times \hat{B} = \hat{y} \times \hat{z} = \hat{x}\right)$, the particle will now also accelerate in the direction $\hat{k}$. This will produce a magnetic force in the $-\hat{y}$ direction that largely cancels the electric force as the particle becomes relativistic. As consequence, the particle will asymptotically approach the speed of light moving along with the incident wave that accelerated it (almost surfing it, a process called "Surfatron"; see Gunn and Ostriker, 1969 and Katsouleas and Dawson, 1983).

2.1.1 The equations of motion

As we have obtained some insight on the particle's behavior, we describe the EMW field as $\vec{E} = E \cos\Phi\, \hat{y}$ and $\vec{B} = B \cos\Phi\, \hat{z}$ (again with $B = E$), where $\Phi \equiv kx - \omega t$ is the relative phase of the wave with respect to the particle and $\omega \equiv 2\pi\nu$ is the angular frequency of the wave. Any radiative effect will be discussed later.

Since the particle's movement could (qualitatively) be in 2D, we analyze its behavior using polar coordinates for the velocity, v, and its angle, θ, with respect to the wave vector, $\vec{k} = k\hat{x}$ (see Figure 2.2). This means

$$\vec{v} = v\hat{v}, \tag{2.3}$$

and therefore

$$\dot{\vec{v}} = \dot{v}\hat{v} + v\dot{\hat{v}} = \dot{v}\hat{v} + v\dot{\theta}\hat{\theta}, \tag{2.4}$$

where $\hat{v} \cdot \hat{\theta} = 0$.

Rewriting the Lorentz force shown in Equation (2.2) using our polar coordinates (Equations 2.3 and 2.4), we obtain that the left-hand side is

$$\vec{F} \equiv \frac{d\vec{p}}{dt} = \frac{d}{dt}\left[m\gamma\vec{v}\right] = m\dot{v}\gamma^3\hat{v} + vm\gamma\dot{\theta}\hat{\theta}, \tag{2.5}$$

where $\gamma = (1 - v^2/c^2)^{-1/2}$ is the Lorentz factor of the particle.

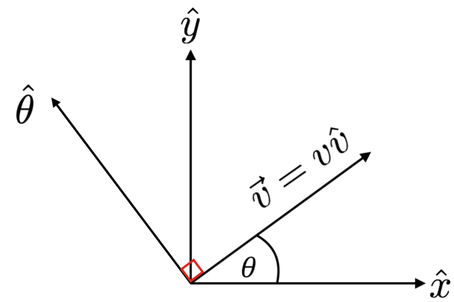

Figure 2.2: Representation of the velocity vector ($\vec{v}$), and the unit vectors $\hat{v}$ and $\hat{\theta}$ in polar coordinates. Note $\hat{v}$ and $\hat{\theta}$ are always perpendicular to each other, which is represented here by a red square.

Doing the same with the right-hand side of Equation (2.2), we obtain

$$\frac{\mathrm{d}\vec{p}}{\mathrm{d}t} = e\left(\vec{E} + \frac{\vec{v}}{c} \times \vec{B}\right) = e\cos\Phi\left[E_v\hat{v} + \left(E_\theta - \frac{v}{c}B\right)\hat{\theta}\right], \tag{2.6}$$

where we have decomposed $\vec{E} = \cos\Phi\left(E_v\hat{v} + E_\theta\hat{\theta}\right)$ and $\vec{v} \times \vec{B} = v\hat{v} \times B\hat{z}\cos\Phi = -vB\cos\Phi\,\hat{\theta}$. Since $B = E$, $E_v = E\sin\theta$, and $E_\theta = E\cos\theta$, then Equation (2.6) can be rewritten as

$$\frac{\mathrm{d}\vec{p}}{\mathrm{d}t} = eE\cos\Phi\left[\sin\theta\,\hat{v} + \left(\cos\theta - \frac{v}{c}\right)\hat{\theta}\right], \tag{2.7}$$

and we can finally obtain the equations of motion of the particle by equating the components along the polar basis vectors:

$$\dot{\gamma} = \omega_c\left(1 - \gamma^{-2}\right)^{1/2}\sin\theta\cos\Phi, \tag{2.8}$$

$$\dot{\theta} = \omega_c\gamma^{-1}\left(1 - \gamma^{-2}\right)^{-1/2}\left[\cos\theta - \left(1 - \gamma^{-2}\right)^{1/2}\right]\cos\Phi, \tag{2.9}$$

$$\dot{\Phi} = \omega\left[\left(1 - \gamma^{-2}\right)^{1/2}\cos\theta - 1\right], \tag{2.10}$$

where we used $\omega_c \equiv eE/mc$. We have converted the equations to dimensionless units by defining $\mu \equiv \omega/\omega_c$ and $\tau \equiv \omega_c t$ and obtained

$$\frac{\mathrm{d}\gamma}{\mathrm{d}\tau} = \left(1-\gamma^{-2}\right)^{1/2} \sin\theta \cos\Phi, \tag{2.11}$$
$$\frac{\mathrm{d}\theta}{\mathrm{d}\tau} = \gamma^{-1}\left(1-\gamma^{-2}\right)^{-1/2} \left[\cos\theta - \left(1-\gamma^{-2}\right)^{1/2}\right] \cos\Phi, \tag{2.12}$$
$$\frac{\mathrm{d}\Phi}{\mathrm{d}\tau} = \mu \left[\left(1-\gamma^{-2}\right)^{1/2} \cos\theta - 1\right]. \tag{2.13}$$

2.1.2 Asymptotic analytic solution

In this subsection we will focus on exploring the particle's behavior assuming it moves relativistically ($\gamma \gg 1$) and nearly co-linear with the wave ($\theta \ll 1$). Given that, another reasonable approximation is to take a constant phase ($\Phi = 0$). Of course, given that our particle's speed will never equal c (and might never point exactly towards $\hat{k}$), the constant phase approximation is valid for a limited period of time. However, given the cyclical behavior of waves, we can also expect a cyclical acceleration process for our particle. Later in this subsection, we will discuss the amount of time for which the constant-phase approximation is valid.

Summarizing, the approximations $\gamma \gg 1$, $\theta \ll 1$, and $\Phi = 0$ (with $\dot{\Phi} = 0$) imply that the equations of motion (Equations 2.11 and 2.12) now become:

$$\frac{\mathrm{d}\gamma}{\mathrm{d}\tau} \approx \theta, \tag{2.14}$$

and

$$\frac{\mathrm{d}\theta}{\mathrm{d}\tau} \approx \frac{1}{2}\gamma^{-1}\left(\gamma^{-2} - \theta^2\right). \tag{2.15}$$

From these equations, we see that if $\theta < \gamma^{-1}$, then Equation (2.15) would make θ increase, ultimately making the assumption $\theta < \gamma^{-1}$ no longer valid. As a consequence, we see that $\theta > \gamma^{-1}$ is the only stable relation for γ and θ (later we will see that this approximation works well enough). Then, we approximate $\theta^2 \gg \gamma^{-2}$, so the equations can be approximated as

$$\frac{\mathrm{d}\gamma}{\mathrm{d}\tau} \approx \theta, \tag{2.16}$$

and

$$\frac{\mathrm{d}\theta}{\mathrm{d}\tau} \approx -\frac{1}{2}\gamma^{-1}\theta^2. \tag{2.17}$$

We can easily solve this system of equations by taking $\frac{\mathrm{d}\theta}{\mathrm{d}\tau}/\frac{\mathrm{d}\gamma}{\mathrm{d}\tau}$ to obtain

$$\theta \approx (D\gamma)^{-1/2}, \tag{2.18}$$

which we replace in Equations (2.16) and (2.17) to obtain the asymptotic solutions for large τ:

$$\gamma = \left[\frac{3}{2}D^{-1/2}\,\tau\right]^{2/3}, \tag{2.19}$$

and

$$\theta = \left[\frac{3}{2}D\,\tau\right]^{-1/3}, \tag{2.20}$$

where D is a constant that depends on the initial conditions of γ and θ. We note that, in principle, the solutions from Equations (2.19) and (2.20) contain constants of integration ~ 1. For simplicity here we neglect these constants since we expect to be working with $\tau \gg 1$ (see Subsection 2.1.3).

We explored the behavior and value of the constant D by considering the change of variable, $\epsilon = \gamma^{-1}$. If we divide Equation (2.11) by Equation (2.12) we obtain

$$\frac{\mathrm{d}\epsilon}{\mathrm{d}\theta} = -\frac{\epsilon\left(1-\epsilon^2\right)\sin\theta}{\cos\theta - (1-\epsilon^2)^{1/2}}, \tag{2.21}$$

so we can construct the relation between ϵ and θ by considering the initial condition $\epsilon(\theta_{min}) = D\theta_{min}^2$ (obtained from Equation 2.18), where $\theta_{min} \ll 1$ is a free parameter. Note that, by doing this, we are actually integrating the equations of motion (Equations 2.11, 2.12, and $\dot{\Phi} = 0$) backwards in time.

Figure 2.3 shows some solutions of Equation (2.21) using the initial condition $\epsilon(\theta_{min}) = D\theta_{min}^2$, with $\theta_{min} = 10^{-3}$, for different values of the constant D. As a reference, we show the numerical solution of Equations (2.11) and (2.12) with constant phase $\Phi = 0$ and the initial conditions $\gamma(t=0) = 1$, and $\theta(t=0) = \pi/2$ (a test particle starting from rest and initially moving in the direction of the electric field). From these results we can see that the

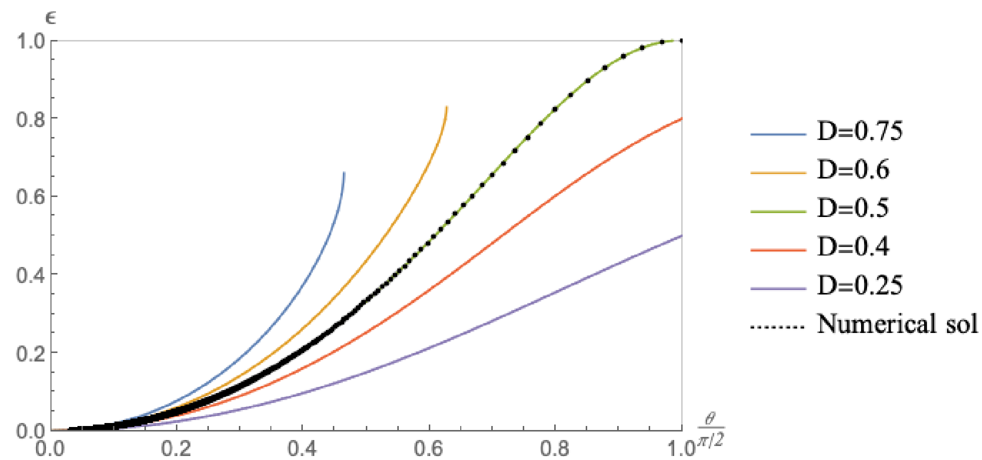

Figure 2.3: Inverse of the Lorentz factor, $\epsilon = \gamma^{-1}$, as function of the velocity inclination angle, θ, obtained by two numerical integration methods. The black doted line ("Numerical sol") is set as the reference result: It is obtained by solving the Equations (2.11) and (2.12) from $\tau = 0$ to $\tau = 10^4$ with fixed phase ($\Phi = 0$) and the initial conditions $\gamma(t = 0) = 1$, and $\theta(t = 0) = \pi/2$ (a test particle starting from rest and initially moving in the direction of the electric field). The rest of the curves are obtained by solving the equation (2.21) with the initial condition $\epsilon(\theta_{min}) = D\theta^2_{min}$ (Equation 2.18), where we tried different values for the constant D. Without losing generality, we took $\theta_{min} = 10^{-3}$ for these simulations.

solution for the equations of motion are highly consistent with $D = 1/2$ (Equation 2.18), which is why we will take that value when evaluating any expression from now on.

Figure 2.4 shows the comparison of the numerical versus the asymptotic behavior of the combination γ/θ. We note that $[\gamma/\theta]_{asympt} = 3\tau/2$ is independent of the parameter D. Therefore, here we are only exploring the linear dependence of γ/θ with time, and its consistency with the numerical results at $\tau \gg 1$.

2.1.3 A limit for the constant-phase approximation: Succession of acceleration cycles

As discussed in the previous subsection, regardless of whether our accelerating particle is able to reach an asymptotic behavior with $\gamma^{-1} \ll \theta \ll 1$, it will gradually accumulate phase, Φ, due to the velocity inclination angle, θ, and the fact that $v < c$ is always true. A combination of this fact with the cyclical nature of the EMW imply a cyclic acceleration process for our particle, albeit with a different timescale period than ω^{-1}. In this subsection we will focus on estimating this timescale and its implications on the equations of motion.

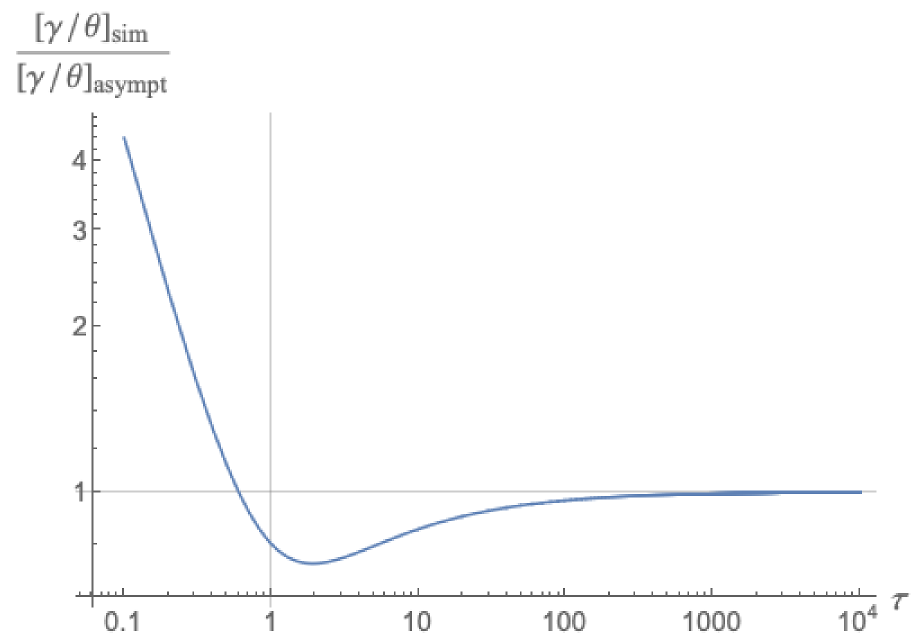

Figure 2.4: Ratio of the numerically simulated (Equations 2.11 and 2.12) to the asymptotic (Equations 2.19 and 2.20) combination γ/θ. For the numerical simulation we took $\Phi = 0$ =constant from $\tau = 0$ to $\tau = 10^4$.

Assuming that the constant phase approximation should dominate the evolution of the equations of motion, it is possible to study the conditions that define each cycle duration using the expressions for γ (Equation 2.19) and θ (Equation 2.20) that we obtained previously. From Equation (2.13) we have

$$\begin{aligned}\Phi(\tau) = kx - 2\pi t = \omega \int \left(\frac{v}{c}\cos\theta - 1\right) \mathrm{d}t \\ = \mu \int_0^\tau \left(\left(1-\gamma^{-2}\right)^{1/2} \cos\theta - 1\right) \mathrm{d}\tau \\ \sim \mu \int_0^\tau \frac{\theta^2}{2} \mathrm{d}\tau,\end{aligned} \tag{2.22}$$

where we have approximated $\gamma^{-1} \ll \theta \ll 1$. Then, using θ (Equation 2.20) and imposing $\Phi(\tau_{sc}) = \pi$, we can obtain the timescale that defines a semi-cycle

$$\tau_{sc} = \frac{2}{3}\pi^3 D^2 \mu^{-3}, \tag{2.23}$$

which implies a distance

$$\Delta_{sc} = c\tau_{sc}/\omega_c = \frac{2}{3}\pi^3 D^2 \left(\frac{c}{\omega}\right) \mu^{-2} \sim 2 \times 10^{12}\,\mathrm{cm} \left(\frac{m}{m_e}\right)^{-2} E_8^2\,\nu_9^{-3}, \tag{2.24}$$

traveled by the particle during that time, where.

In turn, we can evaluate γ (Equation 2.19) and θ (2.20) at τ_{sc} to obtain

$$\gamma_{max} \sim \left[\frac{3}{2} D^{-1/2}\tau_{sc}\right]^{2/3} = D\pi^2\mu^{-2} \sim 4 \times 10^{11} \left(\frac{m}{m_e}\right)^{-2} E_8^2\,\nu_9^{-2}, \tag{2.25}$$

and

$$\theta_{min} \sim \left[\frac{3}{2} D\tau_{sc}\right]^{-1/3} = D^{-1}\pi^{-1}\mu \sim 2 \times 10^{-6} \left(\frac{m}{m_e}\right) E_8^{-1}\,\nu_9, \tag{2.26}$$

which are the maximum Lorentz factor and minimum velocity inclination angle that each accelerating particle can reach within a cycle.

In order to check these estimates (along with the respective approximations and assumptions from which they were obtained) we present Figure 2.5, which shows the full numerical solution of the equations of motion for γ, θ, x, and Φ as function of τ/τ_{sc} using $\mu = 0.1$ (panels (a) and (b)) and $\mu = 10^{-3}$ (panels (c) and (d)). The results are consistent with the expected periodic behavior, except for a factor ~ 2 of deviation in the estimation of τ_{sc} (Equation 2.23), which also implies a similar deviation for γ_{max} and θ_{min}. Nonetheless, our estimations seem to be consistent over time and over different values of μ. We stress that our test particle returns to rest ($\gamma = 1$) periodically, which implies that, ignoring any radiative effect, all mechanical work done on the particle is undone by the end of each cycle.

The Figure 2.5 also shows the linear advance (in the wave direction $\hat{k}$), $x = \int v\cos\theta \mathrm{d}t \sim ct$, which, as expected, grows linearly over time with $v \approx c$.

2.1.4 Radiative effects on the particle acceleration

As of now, we have assumed that radiative effects do not play a relevant role on particle acceleration. The validity of this assumption can be checked by comparing the radiated

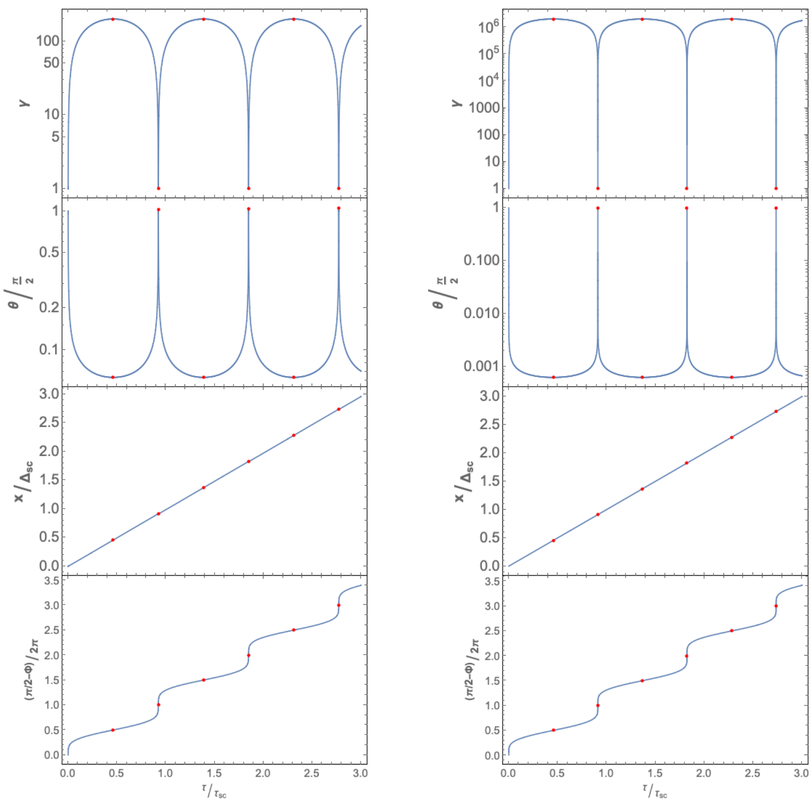

(a) (b)

Figure 2.5: Numerical solution of the Lorentz factor, γ, velocity angle, θ, radial advance, x (normalized by Δ_{sc}), and relative phase, Φ, as function of the dimensionless "time", τ (normalized by τ_{sc}; Equation 2.23) for an accelerating electron in the presence of a constant-amplitude EMW with $\mu \equiv \omega/\omega_c$ using the full equations of motion (Equations 2.11, 2.12, and 2.13). Panel (a) shows the case for $\mu = 0.1$, while panel (b) shows the case for $\mu = 10^{-3}$, both up to a timescale $\tau/\tau_{sc} = 3$. The red dots represent the ends of each semi-cycle experienced by the accelerating particle.

energy with the kinetic energy gained (and lost) in each cycle.

The radiated power has the general expression

$$\begin{aligned} P_{rad} = \frac{2}{3}\frac{e^2\gamma^4}{c^3}(\gamma^2 a_\parallel^2 + a_\perp^2) &= \frac{2}{3}\frac{e^2\gamma^6}{c^3}\left[\dot{\vec{v}}^2 - \left(\frac{\vec{v}}{c}\times\dot{\vec{v}}\right)^2\right] \\ &= \frac{2}{3}\frac{e^2}{c}\left[(1-\gamma^{-2})^{-1}\dot{\gamma}^2 + (1-\gamma^{-2})\gamma^4\dot{\theta}^2\right], \end{aligned} \tag{2.27}$$

where the components of the acceleration are $a_\parallel = \dot{v}$ and $a_\perp = \dot{\theta}v$ (Rybicki and Lightman, 1986).

In the following, we will assess the validity of our assumptions in the non-relativistic and ultra-relativistic regimes.

The non-relativistic regime

In this regime, $\gamma \sim 1$ and $a_\parallel \gg a_\perp$. Thus, the acceleration by the electric field, $a_\parallel = \dot{v} \sim eE/m$, is the main contributor to the particle radiation. Then, integrating Equation 2.27 up to $t_{v\to c} \sim c/\dot{v} = \omega_c^{-1}$ (when the particle becomes relativistic), we obtain

$$\begin{aligned} \frac{\mathcal{E}_{rad}}{\gamma mc^2} &\sim \frac{P_L\,\Delta t_{v\to c}}{mc^2} \sim \frac{e^2}{c^3} a_\parallel^2 \frac{\Delta t_{v\to c}}{mc^2} \\ &\sim \frac{e^2 \omega_c}{c^3 m} \sim 10^{-8} \left(\frac{m}{m_e}\right)^{-2} E_8, \end{aligned} \tag{2.28}$$

where take $E \sim 10^8\,\mathrm{G}$ as a reference value according to E_s (Equation 1.20). Thus, our estimation predicts that the radiated energy is much smaller than the rest mass energy of the particle, which was verified by our simulations (not presented here). This confirms that radiation does not significantly affect the particle's motion in the non-relativistic regime.

The relativistic regime

Once the accelerating particle is relativistic ($\gamma^{-1} \ll \theta \ll 1$), we can use the asymptotic solution we developed in Subsection 2.1.2 (Equations 2.19 and 2.20). In that case, we can estimate the radiated power (Equation 2.27) as

$$\begin{aligned} P_{rad} &\sim \frac{2e^2}{3c}\frac{D^{-1}}{4}\gamma\dot{\gamma}^2 \sim \frac{2e^2}{3c}\frac{D^{-2}}{4}\mu^{-2}\omega^2 = \frac{2e^2}{3c}\frac{D^{-2}}{4}\omega_c^2 \\ &\approx 60\,\mathrm{erg\,s^{-1}} \left(\frac{m}{m_e}\right)^{-2} E_8^2, \end{aligned} \tag{2.29}$$

where we used $\dot{\theta}^2 = \frac{D^{-1}}{4}\gamma^{-3}\dot{\gamma}^2$, and the combination $\gamma\dot{\gamma}^2 \sim \omega_c^2 D^{-1} = \text{constant}$. We can write $P_{rad} = (D/0.5)^{-2}\,\|\vec{S}\|\sigma_T$, where $\|\vec{S}\|$ is the norm of the Poynting vector, $\vec{S} = \frac{c}{4\pi}\vec{E}\times\vec{B}$, and $\sigma_T = \frac{8\pi}{3}\left(e^2/mc^2\right)^2$ is the Thompson cross section. Then, This might be an indirect way to verify $D = 1/2$.

With equation (2.29) we can calculate the radiated energy in a semi-cycle as

$$\mathcal{E}_{rad} \sim P_{rad} \left(\frac{\mu}{\omega}\right) \int_0^{\tau_{sc}} \mathrm{d}\tau = \frac{\pi^3}{9} m_e \left(r_e \omega\right) c \mu^{-4}, \tag{2.30}$$

where $r_e = e^2/m_e c^2$ is the classical electron radius.

In the asymptotic case, the energy gained by the particle within a semi-cycle is

$$\mathcal{E}_{kin} \sim \gamma_{max} mc^2 = D\pi^2 \mu^{-2} mc^2, \tag{2.31}$$

so we can estimate the ratio of the radiated and gained (or lose) energy densities within a semi-cyle as

$$\begin{aligned} \frac{\epsilon_{rad}}{\epsilon_{kin}} &= \frac{\int n\, P_{rad}\, \mathrm{d}t}{\int n\, P_{kin}\, \mathrm{d}t} \sim \frac{\mathcal{E}_{rad}}{\mathcal{E}_{kin}} = \frac{\pi}{9D} \left(\frac{r_e}{c}\right) \omega \mu^{-2} = \frac{\pi}{9D} \frac{\omega_c^2}{\omega \left(c/r_e\right)} \left(\frac{m}{m_e}\right)^{-1} \\ &\sim 10^{-2} \left(\frac{m}{m_e}\right)^{-3} E_8^2\, \nu_9^{-1}, \end{aligned} \tag{2.32}$$

where we have approximated a particle density, $n =$ constant.

This indicates that radiative losses will be negligible with respect to the gained kinetic energy rate (and thus, should not modify the particle's movement) as long as

$$\frac{E}{10^8\ \mathrm{G}} \ll 10 \left(\frac{m}{m_e}\right)^{3/2} \nu_9^{1/2}, \tag{2.33}$$

which is naturally satisfied for our nominal FRB parameters considering that $E \lesssim E_s \sim 10^8\ \mathrm{G}\, L_{42}^{1/2}\, \Delta t_{-3}^{-1}$.

Figure 2.6 show the numerical simulated results of the radiated energy rate, P_{rad}, in comparison with its asymptotic estimation (Equation 2.29) as function of the dimensionless time, τ. The results of the figure show a clear consistency between simulations and our asymptotic model, which is also the case for the kinetic energy (as seen in the simulated results for γ from Figure 2.5 in comparison with its asymptotic estimation; Equation 2.25). As a consequence, all these results support our assumptions about the negligible effects of radiation over the particle's movement (Equation 2.32), as long as Equation (2.33) is satisfied. Worthy of note that any simulation presented in this thesis is numerically solved by the program "Mathematica" using the package "NDsolve", which adapts its step size so that the estimated error in the solutions is within specified tolerance parameters (using at least 10 digits of accuracy and precision).

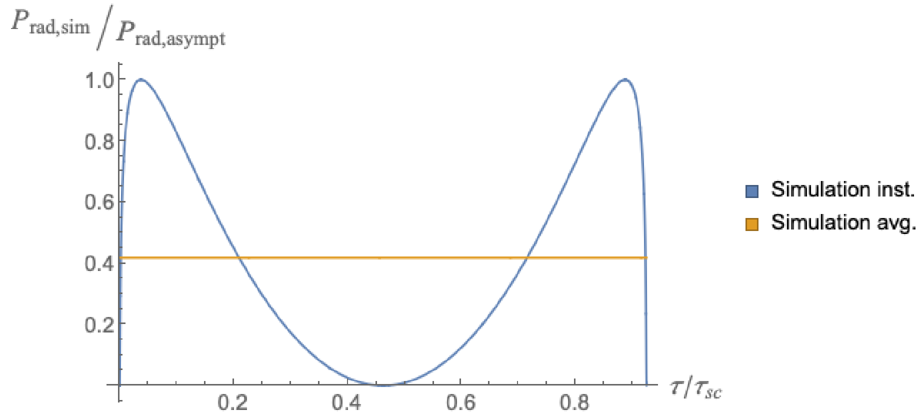

Figure 2.6: Numerical simulation of the radiated energy, P_{rad} (Equation 2.27) normalized by its asymptotic estimation (Equation 2.29) as function of the dimensionless "time", τ, up to $\tau/\tau_{sc} \sim 1$ (Equation 2.23) for an electron accelerated by an EMW with $\mu \equiv \omega/\omega_c$. Here we used the equations of motion from Equations (2.11), (2.12), and (2.13). In this particular case we used $\mu = 0.1$. However, it is worth noting that these results will be similar for any μ sufficiently small.

2.2 Particle acceleration by an EMW of decaying amplitude

As one could suppose, to consider an EMW of constant amplitude is an ideal case whose purpose is to have a glimpse of the particle's behavior. A more realistic case would be to consider an EMW with radially-decaying amplitude. The energy conservation of the FRB radiation demands that the amplitude of the waves decrease as $1/r$, where r is the distance from the source, so we define

$$\omega_c(r) = \omega_i \frac{r_i}{r} = \omega_i \frac{r_i}{r_i + \Delta r} = \omega_i f(r_i, \Delta r), \tag{2.34}$$

where $f(r_i, \Delta r) \equiv r_i/(r_i + \Delta r)$ and $\omega_i \equiv eE_i/mc$. In addition, $r_i \geq r_s$ and $E_i \leq E_s$ are the initial (starting) radius and electric field of our accelerating particle, and

$$\Delta r = \int v \cos\theta \mathrm{d}t = c\mu\omega^{-1} \int \left(1 - \gamma^{-2}\right)^{1/2} \cos\theta \mathrm{d}\tau \tag{2.35}$$

is the radial distance traveled by an accelerating particle after a (dimensionless) time τ.

Following Subsection 2.1, we rewrite our asymptotic ($\gamma^{-1} \ll \theta \ll 1$ and $\Phi = 0$ =constant) equations of motion as

$$\frac{\mathrm{d}\gamma}{\mathrm{d}\tau} \approx \theta f(\tau), \tag{2.36}$$

$$\frac{\mathrm{d}\theta}{\mathrm{d}\tau} = -\frac{1}{2}\gamma^{-1}\theta^2 f(\tau), \tag{2.37}$$

where this time $\tau = \omega_i t$, $\mu \equiv \omega/\omega_i$, and

$$\Delta r \sim ct, \tag{2.38}$$

so

$$f(\tau) \sim \frac{1}{1 + ct/r_i} = \frac{1}{1 + c\tau/\omega_i r_i}, \tag{2.39}$$

where

$$\frac{\omega_i r_i}{c} = \frac{e}{mc^2}\frac{L^{1/2}}{c^{1/2}} \sim 3 \times 10^{12}\, L_{42}^{1/2} \left(\frac{m}{m_e}\right)^{-1} \tag{2.40}$$

is a constant that we will often use, hereafter.

By combining Equations (2.36) and (2.37) we obtain

$$\theta \sim (D\gamma)^{-1/2}\,, \tag{2.41}$$

which is the same of the constant-amplitude case, as it could be expected since $\mathrm{d}\gamma/\mathrm{d}\theta$ is independent from $f(\tau)$. Given this, we might expect $D = 1/2$, which was verified by our simulations.

After that, we can replace Equation (2.41) in Equations (2.36) and (2.37) to finally obtain the solutions

$$\gamma \sim \left[\frac{3}{2\sqrt{D}}\frac{\omega_i r_i}{c}\ln\left(1 + c\tau/\omega_i r_i\right)\right]^{2/3} = \left[\frac{3}{2\sqrt{D}}\frac{\omega_i r_i}{c}\ln\left(\frac{r}{r_i}\right)\right]^{2/3}, \tag{2.42}$$

and

$$\theta \sim \left[\frac{3D}{2}\frac{\omega_i r_i}{c}\ln\left(1+c\tau/\omega_i r_i\right)\right]^{-1/3} = \left[\frac{3D}{2}\frac{\omega_i r_i}{c}\ln\left(\frac{r}{r_i}\right)\right]^{-1/3}, \tag{2.43}$$

which is valid as long as $\gamma^{-1} \ll \theta \ll 1$ and $\omega_i^{-1} \ll \omega^{-1}$. Note that, same as in Subsection 2.1.2, here we are neglecting integration constants ~ 1 for $\tau \gg 1$. In addition, our solutions become equivalent to the constant-amplitude-wave case when $c\tau/\omega_i r_i = r/r_i \ll 1$. Further discussion of the latter will follow on Subsection 2.2.1. On the other hand, the solutions are highly constrained when $c\tau/\omega_i r_i = r/r_i > 1$ due to the presence of the natural logarithm. Let us first consider the case $c\tau/\omega_i r_i = r/r_i > 1$.

Since $\ln(1 + c\tau/\omega_i r_i)$ grows slowly at $\tau \geq \omega_i r_i/c$, we can approximate

$$\gamma_{1/r} \sim \begin{cases} \left[\frac{3}{2\sqrt{D}}\tau\right]^{2/3} & \tau \ll \frac{\omega_i r_i}{c} \\ \left[\frac{3}{2\sqrt{D}}\frac{\omega_i r_i}{c}\right]^{2/3} \sim 4\times 10^{8}\left(\frac{m}{m_e}\right)^{-2/3} L_{42}^{1/3} & \tau \gtrsim \frac{\omega_i r_i}{c} \end{cases} \tag{2.44}$$

and

$$\theta_{1/r} \sim \begin{cases} \left[\frac{3D}{2}\tau\right]^{-1/3} & \tau \ll \frac{\omega_i r_i}{c} \\ \left[\frac{3D}{2}\frac{\omega_i r_i}{c}\right]^{-1/3} \sim 7\times 10^{-5}\left(\frac{m}{m_e}\right)^{1/3} L_{42}^{-1/6} & \tau \gtrsim \frac{\omega_i r_i}{c} \end{cases} \tag{2.45}$$

Therefore, exploring the limits of the constant phase approximation for this case (see Subsection 2.1.3), assuming $\tau \gg \omega_i r_i/c$, we have

$$\begin{aligned} \Phi(\tau) &\sim \frac{\mu}{2}\int_0^{\tau}\theta_{1/r}^2 \mathrm{d}\tau \sim \frac{\mu}{2}\left[\int_0^{\frac{\omega_i r_i}{c}}\left(\frac{3D}{2}\tau\right)^{-2/3}\mathrm{d}\tau + \int_{\frac{\omega_i r_i}{c}}^{\tau}\left(\frac{3D}{2}\frac{\omega_i r_i}{c}\right)^{-2/3}\mathrm{d}\tau\right] \\ &\sim \left(\frac{3D}{2}\frac{\omega_i r_i}{c}\right)^{-2/3}\frac{\mu}{2}\tau. \end{aligned} \tag{2.46}$$

which, imposing $|\Delta\Phi(\tau^*_{sc})| \sim \pi$, implies

$$\tau^*_{sc} \sim \frac{2\pi}{\mu}\left(\frac{3D}{2}\frac{\omega_i r_i}{c}\right)^{2/3}, \tag{2.47}$$

and

$$\Delta^*_{sc} \sim \left(\frac{3D}{2}\frac{\omega_i r_i}{c}\right)^{2/3}\left(\frac{c}{\nu}\right), \tag{2.48}$$

being the latter independent of μ and, therefore, of the starting radius, r_i.

Noticing that $\tau \sim \tau_{sc}^* \gg \omega_i r_i/c$ implies $\Delta r \sim \Delta_{sc}^* \gg r_i$, we may expect that the particle does not return to rest after the first semi-cycle (unlike the constant-amplitude-wave case) since the intensity of the wave decays as $f(\tau) \sim r_i/\Delta r \sim r_i/\Delta_{sc}^* \ll 1$.

Figure 2.7 shows the numerical solutions γ and θ of an accelerating electron in the presence of a radially decaying EMW with $\mu = 10^{-5}$ as function of τ/τ_{sc}^*. We note that these results are consistent with our estimations from Equations (2.44) and (2.45) at $\tau \sim \tau_{sc}^* \gg \omega_i r_i/c$. We also remark that these results are consistent with our guess that the accelerating electron would not return to rest after the first cycle, but will remain relativistic.

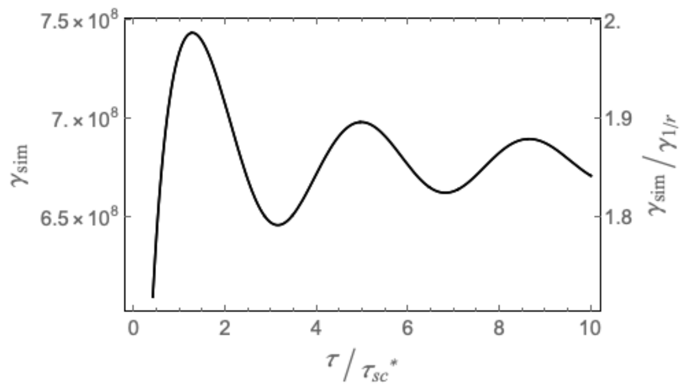

(a)

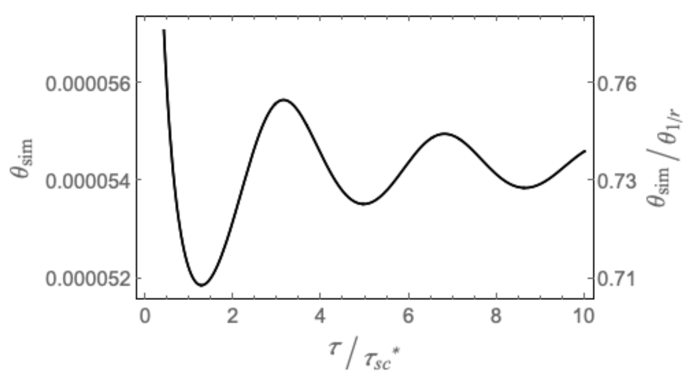

(b)

Figure 2.7: Numerical simulated Lorentz factor, γ (panel (a)), and velocity angle, θ (panel (b)), as function of τ/τ_{sc}^* (Equation 2.47) for an accelerating electron in the presence of a radially decaying EMW with $\mu = 10^{-5}$. Note also that, in the right hand frames of both panels, we are comparing the simulated results with their estimated values $\gamma_{1/r}$ (Equation 2.44) and $\theta_{1/r}$ (Equation 2.45).

2.2.1 Transition between a constant-amplitude and a radially decaying EMW

As it was previously mentioned, the solutions for the equations of motion when considering a radially decaying EMW (Equations 2.42 and 2.43) could be connected with the constant-amplitude-wave case under the approximation $c\tau/\omega_i r_i = r/r_i \ll 1$, but there could be other conditions for this to hold. In this subsection we will focus in defining such conditions in order to simplify our analysis. Regarding that, from the function $f(r_i, \tau) \equiv r_i/(r_i + \Delta r)$ we can see that whenever $\Delta r \ll r_i$ (i.e., the accumulated radial advance of our test particle is negligible with respect to its initial accelerating radius) the constant-amplitude solutions are valid as an approximation.

Our accelerating particle should behave consistent with the cyclical (of dimensionless period τ_{sc}) and symmetrical solutions of Subsection 2.1.2 (Equations 2.19 and 2.20 with their respective maximum (γ_{max}; Equation 2.25) and minimum (θ_{min}; Equation 2.26)) as long as the decay of the wave intensity over the length of one cycle would be much less than the initial wave intensity (parametrized as $\omega_i = eL/mc^{3/2}\, r_i$). This condition can be set as $\Delta_{sc} \ll r_i$ (Equation 2.24), which implies

$$\begin{aligned} \mu &\gg \left[\frac{2}{3}\pi^3 D^2 \left(\frac{\omega_i r_i}{c}\right)^{-1}\right]^{1/3} \equiv \mu_{lim} \\ &\gg 10^{-4} \left(\frac{m}{m_e}\right)^{1/3} L_{42}^{-1/6}, \end{aligned} \tag{2.49}$$

or

$$\begin{aligned} r_i &\gg \frac{c}{\omega}\left[\frac{2}{3}\pi^3 D^2 \left(\frac{\omega_i r_i}{c}\right)^{2}\right]^{1/3} \equiv r_{lim} \\ &\gg 10^{9}\,\mathrm{cm} \left(\frac{m}{m_e}\right)^{-2/3} L_{42}^{1/3}\, \nu_9^{-1}. \end{aligned} \tag{2.50}$$

Therefore, particles starting their acceleration at $r_i \gg r_{lim}$ will follow the solutions of the constant-amplitude wave case according to the initial intensity they perceive, ω_i. Note that the restrictions from comparing Δ_{sc} or Δ_{sc}^* with r_i differ by a factor 3, so they are equivalent for an order-of-magnitude estimation.

Figure 2.8 shows numerical simulated result of the Lorentz factor, γ, as function of the dimensionless time, τ, for an accelerating electron in the presence of a radially decaying EMW for different values of μ. The results show a transition in the behavior of γ: From logarithmic, with smooth oscillations, when considering $\mu = 10^{-5}$ in panel (a) (where we have used τ^*_{sc} (Equation 2.47) as dimensionless time normalization constant) to symmetrical and cyclic (oscillating between rest and relativistic) when $\mu = 10^{-3}$ in panel (c) (where we have used τ_{sc} (Equation 2.23) as dimensionless time normalization constant).

Regarding the transition from Figure 2.8, a geometrical average points to $\mu \sim 10^{-4}$ as the a critical value for this behavioral transition. This is also supported by the substantial change on the observed numbers of cycles of this panel with respect to panel (a), which tell us τ^*_{sc} is ceasing to be a good estimation to describe a semi-cycle. All this consistent with our prediction from Equation (2.49) for electrons. On the other hand, in the case of protons (along with our nominal parameters for FRBs: $L \sim 10^{42}\,\mathrm{erg/s}$, $D = 1/2$ and $\nu \sim 1\mathrm{GHz}$) we have $r_i \geq r_s \sim r_{lim}$, which means that their solutions are consistent with the constant-amplitude-wave approximation for any starting radius, r_i.

2.2.2 A radial distance scale limit for our particle acceleration model

Now we already analyzed the solutions for the particle's acceleration by a radially-decaying wave, we note there is a radius r_i above which $E_i \leq E_{crit}$, in which case our accelerating particle will qualitatively be only oscillating along the electric field axis with $\gamma \sim 1$. Since energy conservation allows us to write $E_i = E_s r_s / r_i$, then the condition $E_i > E_{crit}$ (to ensure a relativistic particle) is rewritten as

$$
\begin{aligned}
r_i < \frac{E_s}{E_{crit}} r_s = \frac{e}{mc}\frac{L^{1/2}}{c^{1/2} 2\nu} \equiv r_f \\
\approx 5 \times 10^{13}\,\mathrm{cm} \left(\frac{m}{m_e}\right)^{-1} L_{42}^{1/2}\, \nu_9^{-1},
\end{aligned}
\tag{2.51}
$$

which would imply two different radial distance ranges in which our particle acceleration is valid; $r_s \leq r_i < r_{f,p^+} = 3 \times 10^{10}\,\mathrm{cm} L_{42}^{1/2}\, \nu_9^{-1}$ for protons, and $r_s \leq r_i < r_{f,e^-} = 5 \times 10^{13}\,\mathrm{cm}\, L_{42}^{1/2}\, \nu_9^{-1}$ for electrons.

We highlight that the difference between these radial scales of acceleration would imply

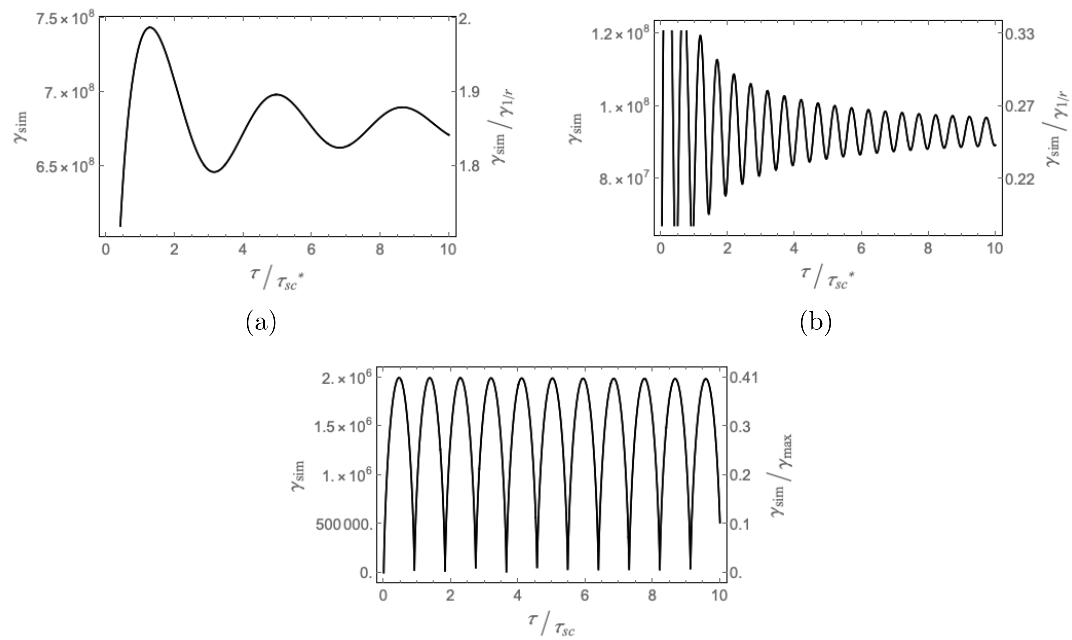

(a) (b) (c)

Figure 2.8: Numerical simulated Lorentz factor, γ, as function of the dimensionless time τ for an accelerating electron in the presence of a radially decaying EMW. (a) Shows the case for $\mu = 10^{-5}$; we also use τ_{sc}^{*} (Equation 2.47) as normalization constant for time. (b) Shows the case for $\mu = 10^{-4}$; we also use τ_{sc}^{*} as normalization constant. (c) Shows the case for $\mu = 10^{-3}$; this time we use τ_{sc} (Equation 2.23) as normalization constant.

the formation of a structure of separate charges. We will discuss this later (see chapter 3.3).

Chapter 3

Particle acceleration model: Extension to a plasma

Now we have an idea of the behavior of single protons and electrons in the presence of a strong and low-frequency EMW, we extend our analysis to a plasma surrounding the FRB source. The aim is to consider some basic properties of such plasma –such density and location– in order to put constraints on the physical mechanism, progenitor scenario (or type) or local environment related to the observed FRBs.

3.1 Avoiding EMW depletion

One of the simplest constraints we can set on a plasma under the presence of an intense EMW comes from imposing that the maximum kinetic energy density transferred by the EMW to the plasma does not exceed the electromagnetic energy density of the wave in order to avoid the depletion of the latter's energy budge. This is $\epsilon_{kin} \sim n\gamma_{max}mc^2 \ll \epsilon_{EM} = E^2/4\pi$ (where for simplicity $B = E =$constant), which implies

$$n \ll \frac{\omega^2 m}{D4\pi^3 e^2} \sim 10^9\,\mathrm{cm}^{-3}\left(\frac{m}{m_e}\right)\nu_9^2. \tag{3.1}$$

That way we can constrain the plasma density to ensure we can actually observe the FRB radiation at $\nu \sim 1$GHz.

It is worth noting that Equation (3.1) assumes the equations of motion of the particles are not modified by radiative effects, which is actually a good approximation as previously discussed for the case of a single accelerating particle (see subec. 2.1.4). However, the radiative analysis could be very different from what we previously showed due to radiative coherence.

3.2 Coherence

We have discussed in Chapter 2 that the incident radiation from FRBs can quickly accelerate the particles, coupling them to the wave and making them all move in the direction of the wave vector, $\hat{k}$. Thus, the acceleration and radiation processes of the plasma particles in this scenario is reminiscent of a coherent mechanism. In this section we study the conditions for such coherence (see also Kumar et al. (2017)) and their implications over the behavior of the plasma.

Considering that the accelerating particles radiate coherently – which means that the individual radiative contribution of each accelerating particle is increased through constructive interference (see Cox, 1979, and Cordes and Wasserman, 2016)–, and that their emitting frequency is the same as that of the incident wave, $\nu \sim 1\text{GHz}$ (Lyubarsky, 2019), then the size of a coherent source, l_l, along the line of sight in our reference frame must satisfy

$$l_l \lesssim k^{-1} = \frac{\lambda}{2\pi}. \tag{3.2}$$

However, the previous condition does not apply to the transverse size of the coherent source.

Assuming that the emitting particles move towards us with γ, then the radiated wavelength in their reference frame will be

$$\lambda' \sim \gamma\lambda, \tag{3.3}$$

which remains the same in our reference system. Thus, the transverse coherent source size,

l_t, in our reference frame follows

$$l_t \lesssim k^{-1}\gamma \sim 8\times10^{6}\,\mathrm{cm}\left(\frac{r_i}{r_{f,p^+}}\right)^{-2}\left(\frac{m}{m_e}\right)^{-2}\nu_9^{-1}, \tag{3.4}$$

where we used $\gamma \sim \gamma_{max}$ (Equation 2.25).

Another important restriction for coherence is that the motion of the accelerating particles is confined within the emitting cone ($\sim 1/\gamma$) of the relativistic particles, so that the radiation of all the particles involved is aligned. In a radially expanding source, this implies that the transverse coherent source size, l_t, has to satisfy

$$l_t \lesssim \frac{r_i}{\gamma} \sim 2\times10^{4}\,\mathrm{cm}\left(\frac{r_i}{r_{f,p^+}}\right)^{3}\left(\frac{m}{m_e}\right)^{2}L_{42}^{1/2}\nu_9^{-1}, \tag{3.5}$$

where we used $\gamma \sim \gamma_{max}$ (Equation 2.25).

However, since the distance path of the radiation from the opposite ends of the transverse source size is increased with respect to the line-of-sight size, then we have to check that

$$\sqrt{l_t^2 + r_i^2} + \sqrt{l_t^2 + D^2} - D - r_i \ll \lambda \tag{3.6}$$

in order that coherence is valid, where D is the distance from the FRB source to us. Equation (3.6) can be rewritten as

$$l_t \lesssim \sqrt{2\lambda\left(\frac{1}{r_i}+\frac{1}{D}\right)^{-1}} \sim \sqrt{2\lambda r_i} \sim 10^{6}\mathrm{cm}\left(\frac{r_i}{r_{f,p^+}}\right)^{1/2}\nu_9^{-1}L_{42}^{1/4}, \tag{3.7}$$

where we neglected $D \sim$ Gpc since it is substantially greater than the radial distances of our interest ($r_i \sim r_f$ for protons and electrons).

Since all these estimations for l_t are relevant, we take

$$l_t \sim \min\left\{\frac{r_i}{\gamma}, \frac{\lambda}{2\pi}\gamma, \sqrt{2\lambda r_i}\right\}, \tag{3.8}$$

from which we obtain

$$l_t \sim \begin{cases} r_i/\gamma_{max} \sim 2 \times 10^4\,\mathrm{cm} \left(\frac{r_i}{r_{f,p^+}}\right)^3 \left(\frac{m}{m_e}\right)^2 L_{42}^{1/2}\,\nu_9^{-1}, & \left(\frac{r_i}{r_{f,p^+}}\right) \leq 3 \left(\frac{m}{m_e}\right)^{-4/5} L_{42}^{-1/10} \\ \frac{\lambda}{2\pi}\gamma_{max} \sim 8 \times 10^6\,\mathrm{cm} \left(\frac{r_i}{r_{f,p^+}}\right)^{-2} \left(\frac{m}{m_e}\right)^{-2} \nu_9^{-1}, & \left(\frac{r_i}{r_{f,p^+}}\right) > 3 \left(\frac{m}{m_e}\right)^{-4/5} L_{42}^{-1/10}. \end{cases} \tag{3.9}$$

Notice that the condition from Equation (3.7) is naturally satisfied for our definition of l_t in Equation (3.9).

As a consequence, the plasma density, n, has to satisfy

$$n \gg \frac{1}{l_l l_t^2} \equiv \frac{1}{V_{coh}} \equiv n_{coh} \tag{3.10}$$

in order for coherent radiation to be in operation, where

$$\frac{n_{coh}}{\mathrm{cm}^{-3}} \equiv \begin{cases} \gamma_{max}^2 \frac{k}{r_i^2} \approx 5 \times 10^{-10} \left(\frac{r_i}{r_{f,p^+}}\right)^{-6} \left(\frac{m}{m_e}\right)^{-4} L_{42}^{-1}\,\nu_9^3, & \left(\frac{r_i}{r_{f,p^+}}\right) \leq 3 \left(\frac{m}{m_e}\right)^{-\frac{4}{5}} L_{42}^{-\frac{1}{10}} \\ \gamma_{max}^{-2} k^3 \approx 7 \times 10^{-15} \left(\frac{r_i}{r_{f,p^+}}\right)^4 \left(\frac{m}{m_e}\right)^4 \nu_9^3, & \left(\frac{r_i}{r_{f,p^+}}\right) > 3 \left(\frac{m}{m_e}\right)^{-\frac{4}{5}} L_{42}^{-\frac{1}{10}}. \end{cases} \tag{3.11}$$

A reasonable guess to estimate the coherent radiation power is to multiply the incoherent radiation power by the number of particles within the coherent volume (Cordes and Wasserman, 2016). This means

$$P_{rad,coh} \sim nV_{coh} \times P_{rad}, \tag{3.12}$$

where nV_{coh} is the number of particles within the coherent volume V_{coh}.

With this, we can calculate

$$
\begin{aligned}
\frac{\epsilon_{rad,coh}}{\epsilon_{kin}} &= \frac{\int n^2 V_{coh}\, P_{rad}\,\mathrm{d}t}{\int n\, P_{kin}\,\mathrm{d}t} \sim \frac{n V_{coh} P_{rad}\,\tau_{sc}/\omega_i}{mc^2\gamma_{max}} \\
&= \begin{cases} \frac{8}{9\pi}\left(\frac{D}{1/2}\right)^{-3}\left(\frac{m_p}{m_e}\right)^{-2} n r_e^2\, \frac{cL}{\omega_i^2 mc^2}\left(\frac{r_i}{r_{f,p^+}}\right)^2, & \left(\frac{r_i}{r_{f,p^+}}\right) \leq 3\left(\frac{m}{m_e}\right)^{-\frac{4}{5}} L_{42}^{-\frac{1}{10}} \\ \frac{D\pi^5}{9}\left(\frac{m}{m_e}\right)^{-1} \frac{\omega_i^6}{\omega^5 (c/r_e)}\left(\frac{c}{\omega}\right)^3 n, & \left(\frac{r_i}{r_{f,p^+}}\right) > 3\left(\frac{m}{m_e}\right)^{-\frac{4}{5}} L_{42}^{-\frac{1}{10}} \end{cases} \\
&\sim \begin{cases} 20\left(\frac{n}{\mathrm{cm}^{-3}}\right)\left(\frac{r_i}{r_{f,p^+}}\right)^4\left(\frac{m}{m_e}\right) L_{42}\,\nu_9^{-2}, & \left(\frac{r_i}{r_{f,p^+}}\right) \leq 3\left(\frac{m}{m_e}\right)^{-\frac{4}{5}} L_{42}^{-\frac{1}{10}} \\ 10^6\left(\frac{n}{\mathrm{cm}^{-3}}\right)\left(\frac{r_i}{r_{f,p^+}}\right)^{-6}\left(\frac{m}{m_e}\right)^{-7} \nu_9^{-2}, & \left(\frac{r_i}{r_{f,p^+}}\right) > 3\left(\frac{m}{m_e}\right)^{-\frac{4}{5}} L_{42}^{-\frac{1}{10}}. \end{cases}
\end{aligned}
\tag{3.13}
$$

So, similarly as we did in Subsection 2.1.4, we can neglect radiative effects on the particle's movement if $\epsilon_{rad,coh} \ll \epsilon_{kin}$, which is fulfilled when

$$
n \ll \begin{cases} 5\times 10^{-2}\,\mathrm{cm}^{-3}\left(\frac{r_i}{r_{f,p^+}}\right)^{-4} L_{42}^{-1}\,\nu_9^2, & \left(\frac{r_i}{r_{f,p^+}}\right) \leq 3\, L_{42}^{-\frac{1}{10}} \\ 10^{-6}\,\mathrm{cm}^{-3}\left(\frac{r_i}{r_{f,p^+}}\right)^{6} \nu_9^2, & \left(\frac{r_i}{r_{f,p^+}}\right) > 3\, L_{42}^{-\frac{1}{10}} \end{cases}
\tag{3.14}
$$

for electrons, and

$$
n \ll \begin{cases} 3\times 10^{-5}\,\mathrm{cm}^{-3}\left(\frac{r_i}{r_{f,p^+}}\right)^{-4} L_{42}^{-1}\nu_9^2, & \left(\frac{r_i}{r_{f,p^+}}\right) \leq 7\times 10^{-3} L_{42}^{-\frac{1}{10}} \\ 10^{16}\,\mathrm{cm}^{-3}\left(\frac{r_i}{r_{f,p^+}}\right)^{6} \nu_9^2, & \left(\frac{r_i}{r_{f,p^+}}\right) > 7\times 10^{-3} L_{42}^{-\frac{1}{10}} \end{cases}
\tag{3.15}
$$

for protons. Note that the condition for coherence to modify the motion of protons is several orders of magnitude less restrictive than for electrons.

Figure 3.1 shows the behaviors and restrictions of the plasma explored so far in terms of its density, n, and initial accelerating radius, r_i. For instance, we show the curve "n_{coh}" (in red; Equation 3.11), at which the electrons become coherent, and the curve "$\epsilon_{kin} = \epsilon_{rad,coh}$" (in pink, Equation 3.13), where the coherent radiation starts playing a relevant role in the equations of motion. Finally, we show the restriction that arises from avoiding the EMW energy being depleted by the particle acceleration process, $\epsilon_{kin} \ll \epsilon_{EMW}$ (dashed and green curve; Equation 3.1), in which we neglect effects of the coherent radiation over the equations of motion. We note that the region above the latter curve is ruled out for observed FRBs. Note also that the latter restriction does not apply above the curve "$\epsilon_{kin} = \epsilon_{rad,coh}$".

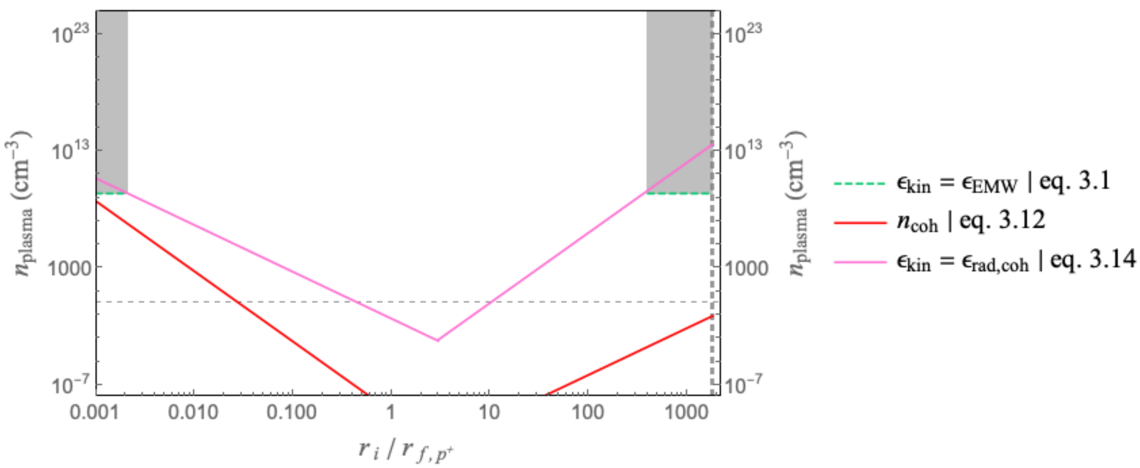

Figure 3.1: Regimes of behavior and restrictions for electrons accelerated by a EMW of amplitude $E \sim \sqrt{L/c\,r_i^2}$ and frequency $\nu = 1\,$GHz from an observed FRB of luminosity, $L = 10^{42}\,$erg/s. The results are expressed in this figure in terms of plasma density as function of the initial radius of acceleration, $r_i/r_{f,p^+}$. The curve "$\epsilon_{kin} = \epsilon_{EMW}$" (dashed and green curve; Equation 3.1) is set in order to avoid the EMW energy depletion by particle acceleration, assuming that the coherent radiation does not modify their equations of motion. The curve "n_{coh}"(in red; Equation 3.11) divides the figure into regimes of incoherent and coherent emission. The curve "$\epsilon_{kin} = \epsilon_{rad,coh}$" (in pink, Equation 3.13) divides the figure into regimes in which the coherent radiation modifies and no does not modify the equations of motion. Notice that "$\epsilon_{kin} = \epsilon_{EMW}$" is only valid in relation with their position with respect to "$\epsilon_{kin} = \epsilon_{rad,coh}$"; and also note that the grey region is restricted. In addition, the thin dashed grey horizontal line indicates $n = 1\,\mathrm{cm}^{-3}$, while the thick dashed grey vertical line indicates $r_{f,e^-}/r_{f,p^+} = m_p/m_e$.

This figure tells us that coherent radiation is likely to modify the equations of motion of protons and electrons at some starting radius $r_i \lesssim r_f$. This case is non-linear and very complex, therefore we leave it for future work. However, we will present a brief discussion about this in Section 3.5.

Note that for simplicity we show only the behaviors and restrictions for electrons in Figure 3.1, while the plasma also contains protons, which can be accelerated up to a radial scale $r_{f,p^+} \approx 3\times 10^{10}\,\mathrm{cm}\,L_{42}^{1/2}\,\nu_9^{-1}$. As was previously discussed in Subsection 2.2.2, the different maximum radii of acceleration between protons and electrons ($r_{f,e^-} \sim r_{f,p^+}\,(m_p/m_e)$) and their implications for the plasma behavior must be analyzed before continuing.

3.3 The charge-separated region

As discussed in Subsection 2.2.2, the maximum radii of acceleration are different for protons and electrons ($r_{f,e^-} \sim r_{f,p^+}(m_p/m_e)$). In the region between these two radii, protons are not accelerated to relativistic speeds, while electrons, in principle, can still become relativistic due to their interaction with the EMW. As a consequence, there will be a "charge-separated region" (CSR). The aim of this section is to study their implications on the plasma acceleration process.

If we approximate that the protons are fixed in place, the CSR implies the generation of an induced electric field that can be naively modeled as a spherical capacitor with electric field

$$E_{CSR} = \frac{4\pi}{3} enr \left(1 - \frac{r_{f,p^+}^3}{r^3}\right) \sim \frac{4\pi}{3} enr \tag{3.16}$$

where the last expression can be easily obtained at $r \gg r_{f,p^+}$.

3.3.1 CSR potential energy and proton/electron separation

Assuming stationary protons and relativistic electrons within the CSR, the potential energy, $\mathcal{E}_{ind}$, at r_i can be estimated as

$$\begin{aligned} \mathcal{E}_{ind} &\sim \int_{r_{f,p^+}}^{r_i} \frac{E_{CSR}^2}{8\pi} 4\pi r_i^2 \mathrm{d}r_i = \int_{r_{f,p^+}}^{r_i} \left(\frac{4\pi}{3}\right)^2 \frac{n^2 e^2 r_i^4}{2} \left(1 - \frac{r_{f,p^+}^3}{r_i^3}\right)^2 \mathrm{d}r_i \\ &= \left(\frac{4\pi}{3}\right)^2 \frac{n^2 e^2 r_i^5}{10} \left[1 - 5\frac{r_{f,p^+}^3}{r_i^3} + 9\frac{r_{f,p^+}^5}{r_i^5} - 5\frac{r_{f,p^+}^6}{r_i^6}\right] \\ &\sim 8 \times 10^{33} \mathrm{erg} \left(\frac{n}{\mathrm{cm}^{-3}}\right)^2 \left(\frac{r_i}{r_{f,p^+}}\right)^5 L_{42}^{5/2} \nu_9^{-5} \left[1 - 5\frac{r_{f,p^+}^3}{r_i^3} + 9\frac{r_{f,p^+}^5}{r_i^5} - 5\frac{r_{f,p^+}^6}{r_i^6}\right], \end{aligned} \tag{3.17}$$

which we can use to set the condition

$$n \ll n_{CSR,FRB} \sim 4 \times 10^2 \,\mathrm{cm}^{-3} \left(\frac{r_i}{r_{f,p^+}}\right)^{-5/2} L_{42}^{-3/4} \nu_9^{5/2} \Delta t_{-3}^{1/2} \left[1 - 5\frac{r_{f,p^+}^3}{r_i^3} + 9\frac{r_{f,p^+}^5}{r_i^5} - 5\frac{r_{f,p^+}^6}{r_i^6}\right]^{-1/2}, \tag{3.18}$$

in order to avoid the complete transference of the FRB energy budget (of luminosity $L = 10^{42}$ erg/s and duration $\Delta t = 10^{-3}$ s) into the induced electric field, E_{CSR}, of the CSR. However, the approximation of fixed protons is only consistent as long as the electrons move a distance $\Delta r \sim r_i$ before the protons become relativistic. Assuming an electron velocity $v_{e^-} \approx c$, this condition can be written as

$$a_{p^+} = eE_{CSR}/m_p c \ll c/r_i, \tag{3.19}$$

where $a \equiv eE_{CSR}/mc$. This means

$$\begin{aligned} n &\ll \frac{3}{\pi} r_e^{-1} \left(\frac{\nu}{c}\right)^2 \left(\frac{m_p}{m_e}\right)^3 \left(\frac{m_e c^2}{L}\frac{c}{r_e}\right) \left(\frac{r_i}{r_{f,p^+}}\right)^{-2} \left(1 - \frac{r_{f,p^+}^3}{r_i^3}\right)^{-1} \\ &\sim 2 \times 10^{-6}\,\mathrm{cm}^{-3} \left(\frac{r_i}{r_{f,p^+}}\right)^{-2} \left(1 - \frac{r_{f,p^+}^3}{r_i^3}\right)^{-1} L_{42}^{-1}\,\nu_9^2. \end{aligned} \tag{3.20}$$

So, in the cases in which Equation (3.20) is not satisfied, protons can be delayed with respect to electrons up to a distance scale

$$\begin{aligned} \Delta x_{p^+e^-} &\sim \frac{c}{a_{p^+}} = \frac{3}{2\pi} n^{-1} r_e^{-1} \left(\frac{\nu}{c}\right) \left(\frac{m_p}{m_e}\right)^2 \left(\frac{m_e c^2}{L}\frac{c}{r_e}\right)^{1/2} \left(\frac{r_i}{r_{f,p^+}}\right)^{-1} \left(1 - \frac{r_{f,p^+}^3}{r_i^3}\right)^{-1} \\ &\sim 5 \times 10^4\mathrm{cm} \left(\frac{n}{\mathrm{cm}^{-3}}\right)^{-1} \left(\frac{r_i}{r_{f,p^+}}\right)^{-1} \left(1 - \frac{r_{f,p^+}^3}{r_i^3}\right)^{-1} L_{42}^{-1/2}\,\nu_9. \end{aligned} \tag{3.21}$$

On one side, Equations (3.20) and (3.21) tell us that it is possible that the induced electric field in the CSR is geometrically more complex –likely, with a separation distribution between protons and electrons along the CSR– than the simple spherical capacitor with fixed protons and relativistic electrons, in which case our naive plasma density restriction to avoiding the EMW absorption by the CSR (Equation 3.18) should be relaxed (the complex the electric field geometry is, the less electric energy it can contain). On the other side, the lower limit on the proton-electron distance (Equation 3.21) implies that protons will be behind the wave-surfing electrons, so that our estimated induced electric field (E_{CSR}; Equation 3.16) is fine as an order-of-magnitude estimation around $r \sim r_i$.

3.3.2 Free electron acceleration within the CSR

In this subsection we explore the limits of our particle acceleration model applied to electrons within the limits of the CSR (from r_{f,p^+} to r_{f,e^-}). A first approach comes from imposing $E_{CSR} \ll E_{EMW}$ in order to verify that the electron is accelerating to relativistic speeds despite the presence of the induced electric field of the CSR. This leads to the restriction

$$\begin{aligned} n_{CSR} &\ll \frac{3}{\pi} r_e^{-1} \left(\frac{\nu}{c}\right)^2 \left(\frac{m_p}{m_e}\right)^2 \left[\frac{m_e c^2}{L}\left(\frac{c}{r_e}\right)\right]^{1/2} \left(\frac{r}{r_{f,p^+}}\right)^{-2} \left(1 - \frac{r_{f,p^+}^3}{r^3}\right)^{-1} \\ &\sim 4 \times 10^3\,\mathrm{cm}^{-3} \left(\frac{r}{r_{f,p^+}}\right)^{-2} \left(1 - \frac{r_{f,p^+}^3}{r^3}\right)^{-1} L_{42}^{-1/2}\,\nu_9^2. \end{aligned} \tag{3.22}$$

A more restrictive condition arises by comparing the maximum kinetic energy ($\gamma_{max} m_e c^2$; Equation 2.25) of a freely accelerating electron with the potential electric energy stored within a semi-cycle radial advance ($\Delta x \sim \Delta_{sc}$) of the same electron with respect to the fixed protons at r_i. In this case, neglecting radiative effects, we have

$$eE_{CSR}(r_i)\Delta_{sc} \lesssim \gamma_{max} m_e c^2 \tag{3.23}$$

which, assuming $E_{CSR} =$ constant (Equation 3.16), implies

$$\begin{aligned} n &< \frac{9}{\pi}\frac{m_p}{m_e}\left[\left(\frac{m_e c^2}{L}\right)\frac{c}{r_e}\right]^{1/2} r_e^{-1}\left(\frac{\nu}{c}\right)^2 \left(\frac{D}{1/2}\right)^{-1} \left(\frac{r_i}{r_{f,p^+}}\right)^{-1} \left(1 - \frac{r_{f,p^+}^3}{r_i^3}\right)^{-1} \equiv n_{CSR,\,trf}(\Delta_{sc}) \\ &\sim 5\,\mathrm{cm}^{-3} \left(\frac{r_i}{r_{f,p^+}}\right)^{-1} \left(1 - \frac{r_{f,p^+}^3}{r_i^3}\right)^{-1} L_{42}^{-1/2}\,\nu_9^2. \end{aligned} \tag{3.24}$$

Thus, within a given cycle, the motion of the electrons in a plasma satisfying this condition will not be strongly modified by E_{CSR}. On the other hand, we must emphasize that a plasma with $n \gtrsim n_{CSR,\,trf}(\Delta_{sc})$ would not follow the solutions and restrictions explored in the previous chapters regarding the plasma acceleration process.

Regarding the analysis related to Equations (3.23) and (3.24), we can put a more restrictive condition by demanding the free movement of our accelerating electrons up to a distance $\Delta r \sim r_i$ (which we will see is an important distance scale for radiative matters; see Section 3.5). In that case

$$\mathcal{E}_{csr}(r_i, \Delta r = r_i) = \int_{r_i}^{2r_i} \frac{2\pi}{3} e^2 n r \left(1 - \frac{r_{f,p^+}^3}{r^3}\right) \mathrm{d}r = \frac{2\pi}{3} e^2 n r_i^2 \left(3 - \frac{r_{f,p^+}^3}{r_i^3}\right), \tag{3.25}$$

so when comparing this energy with the maximum kinetic energy of electrons ($\gamma_{max}\, m_e c^2$), we obtain the restriction

$$\begin{aligned} n &< \frac{6D}{\pi} \left(\frac{e^2}{m_p c^2}\right)^{-2} \frac{m_p}{m_e} \frac{m_p c \nu^2}{L} \left(\frac{r_i}{r_{f,p^+}}\right)^{-4} \left(3 - \frac{r_{f,p^+}^3}{r_i^3}\right)^{-1} \equiv n_{CSR,\,trf}(r_i) \\ &\sim 3 \times 10^{-3} \mathrm{cm}^{-3} \left(\frac{r_i}{r_{f,p^+}}\right)^{-4} \left(3 - \frac{r_{f,p^+}^3}{r_i^3}\right)^{-1} L_{42}^{-1}\, \nu_9^2, \end{aligned} \tag{3.26}$$

where we have assumed that the equations of motion are not modified by radiative effects.

Figure 3.2 shows the plasma density restrictions for the free movement of electrons accelerated by a EMW within the CSR zone ($\sim$ 1 cycle, Equation 3.24; and $\Delta r \sim r_i$, Equation 3.26). We note the figure is empty above the curve "$n_{CSR,\,trf}(\Delta_{sc})$" since there we can no longer trust our asymptotic model even for a single cycle. Also note that the coloured zones of the figure are explained in more detail in Subsection 3.4.

3.3.3 Equations of motion in the CSR

We can verify the restrictions of the curves "$n_{CSR,\,trf}(\Delta_{sc})$" and "$n_{CSR,\,trf}(r_i)$" by adding the electric field of the CSR, E_{CSR}, into the equations of motion. In that case we have

$$\dot{\gamma} = \left(1 - \gamma^{-2}\right)^{1/2} \left[\omega_c \sin\theta \cos\Phi - a\cos\theta\right], \tag{3.27}$$

$$\dot{\theta} = \gamma^{-1} \left(1 - \gamma^{-2}\right)^{-1/2} \left[\omega_c \cos\Phi \left(\cos\theta - \left(1 - \gamma^{-2}\right)^{1/2}\right) + a\sin\theta\right], \tag{3.28}$$

$$\dot{\Phi} = \omega \left(\left(1 - \gamma^{-2}\right)^{1/2} \cos\theta - 1\right). \tag{3.29}$$

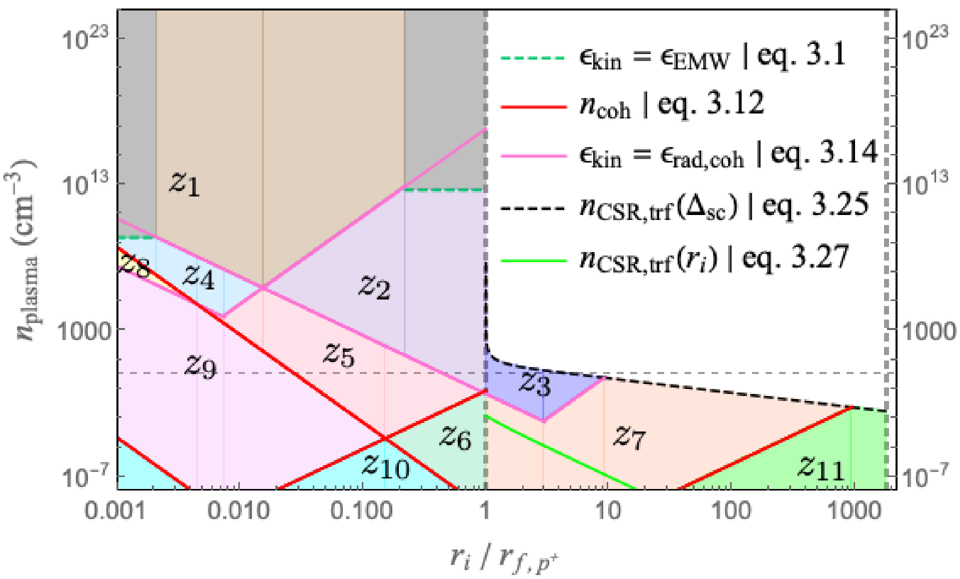

Figure 3.2: Regimes of behavior and restrictions for electrons accelerated by an EMW of amplitude $E \sim \sqrt{L/c r_i^2}$ and frequency $\nu = 1\,\mathrm{GHz}$ from an observed FRB of luminosity $L = 10^{42}$ erg/s. The results in this figure are expressed in terms of plasma density as function of the initial radius of acceleration, $r_i/r_{f,p^+}$. Here are also present the modifications by the induced electric field, E_{CSR} (Equation 3.16), of the CSR. Some of the curves were previously explained in Figure 3.1. The black and dashed curve "$n_{CSR,\,trf}(\Delta_{sc})$" (Equation 3.24) is related to the transference of the maximum kinetic energy of electrons to the induced electric field, E_{CSR}, along the path length of one semi-cycle, Δ_{sc} (Equation 2.24). The green curve "$n_{CSR,\,trf}(r_i)$" (Equation 3.26) is related to the transference of the maximum kinetic energy of electrons to the induced electric field, E_{CSR}, along a radial advance, $\Delta r \sim r_i$. The figure also shows coloured zones for the plasma behavior, which are labeled as z_n and explained in Subsection 3.4. In addition, the thin dashed grey horizontal line indicates $n = 1\mathrm{cm}^{-3}$, while the thick dashed grey vertical lines indicate $r_f/r_s \sim 10^3\,(m/m_e)^{-1}\,L_{42}^{1/2}\,\nu_9^{-1}\,\Delta t_{-3}^{-1}$ for protons and electrons.

Note that we can reduce the number of free parameters again by defining $\tau \equiv \omega_c t$, $\mu \equiv \omega/\omega_c$, and the parameter

$$b \equiv \frac{a}{\omega_c} = \frac{E_{CSR}}{E_{EMW}}, \tag{3.30}$$

so the equations of motion now become

$$\frac{\mathrm{d}\gamma}{\mathrm{d}\tau} = \left(1-\gamma^{-2}\right)^{1/2}\left[\sin\theta\,\cos\Phi - b\cos\theta\right], \tag{3.31}$$

$$\frac{\mathrm{d}\theta}{\mathrm{d}\tau} = \gamma^{-1}\left(1-\gamma^{-2}\right)^{-1/2}\left[\cos\Phi\,\left(\cos\theta-\left(1-\gamma^{-2}\right)^{1/2}\right)+b\sin\theta\right], \tag{3.32}$$

$$\frac{\mathrm{d}\Phi}{\mathrm{d}\tau} = \mu\left(\left(1-\gamma^{-2}\right)^{1/2}\cos\theta - 1\right). \tag{3.33}$$

We stress that, hereafter, we will consider E_{CSR} (and therefore a) as a constant, which is partially justified since we consider radial advances $\Delta r \lesssim r_i$.

Assuming negligible radiative effects, we can rewrite the restriction from the curve "$n_{CSR,\,trf}(\Delta_{sc})$" (Equation 3.24) as

$$b \ll \frac{3}{\pi}\left(\frac{D}{1/2}\right)^{-1}\mu \sim \mu \tag{3.34}$$

to ensure a one-cycle free electron acceleration, and of the curve "$n_{CSR,\,trf}(r_i)$" (Equation 3.26) as

$$b \ll \left(\frac{D}{1/2}\right)\frac{\pi^2}{2}\left(\frac{m_e c^2}{L}\frac{c}{r_e}\right)^{1/2}\mu^{-2} \sim 10^{-8}\left(\frac{\mu}{10^{-2}}\right)^{-2} L_{42}^{-1/2} \tag{3.35}$$

to ensure free electron acceleration for a radial advance $\Delta r \sim r_i$.

Figure 3.3 shows the case of the curve "$n_{CSR,\,trf}(\Delta_{sc})$", in which the kinetic energy of the electron is expected to be lost within a semi-cycle ($\Delta r \sim \Delta_{sc}$). The actual results show a substantial decrease in the Lorentz factor between cycles (which consequently shortens over time). We note that, given numerical limitations, we only show our simulations up to $\tau/\tau_{sc} \sim 0.1$, which nevertheless is sufficient to show the validity of the restriction from Equation (3.34) (and its original equation 3.24). Now, by doing this same exercise with the condition from the curve"$n_{CSR,\,trf}(r_i)$" we obtain the same conclusion, except that it happens in a longer radial scale ($\sim r_i$).

Figure 3.4 shows the Lorentz factor, $\gamma_{start,cycle}$, at the beginning of each cycle. Here the results show that there are no symmetric cycles, unlike what is observed when there is no induced electric field.

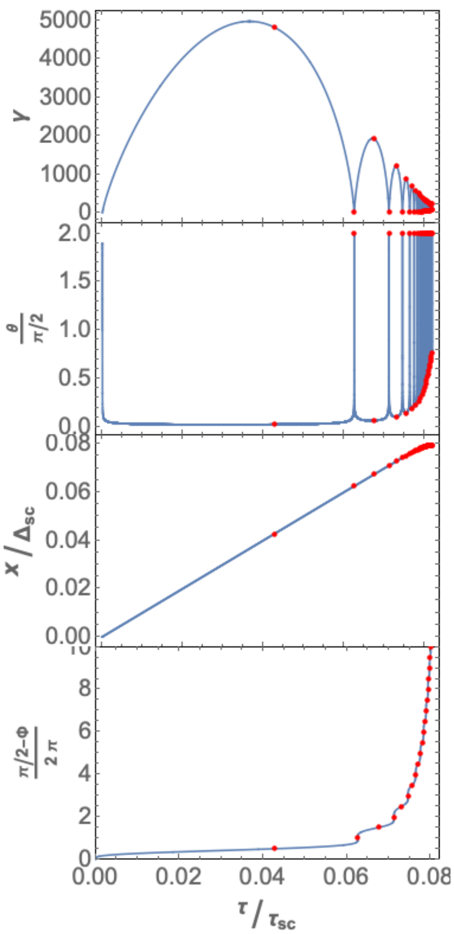

Figure 3.3: Numerical solution for the Lorentz factor, γ, velocity angle, θ, radial advance, x/Δ_{sc}, and phase, Φ, as functions of τ/τ_{sc} (Equation 2.23) for an electron accelerated by an EMW of amplitude parametrized by $\mu = \omega/\omega_i$. The simulations also consider the presence of the induced electric field of the CSR, which is parameterized by $b \equiv a/\omega_c$. In this case we chose $b = \mu = 10^{-2}$, according to Equation (3.24).

As we could observe along this subsection, our curves "$n_{CSR,trf}(\Delta_{sc})$" and "$n_{CSR,trf}(r_i)$" serve as an order-of-magnitude restriction to clarify the limits of our simplified model of particle acceleration for the case of electrons in the CSR.

3.4 Regions of different plasma behavior

In this section we summarize the plasma behavior in each of the zones identified in Figure 3.2, which are divided in terms of the plasma density, n, and the radial distance,

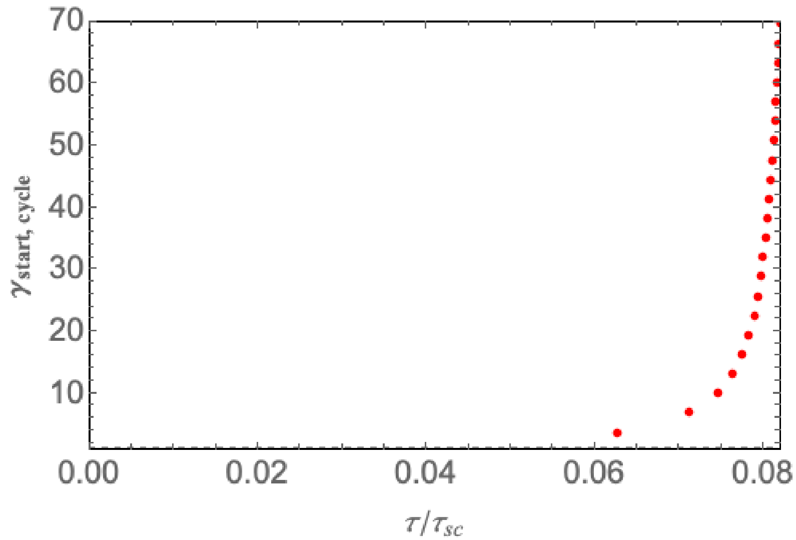

Figure 3.4: Numerical solution for the Lorentz factor, $\gamma_{start,cycle}$, at the start of each cycle as a function of τ/τ_{sc} (Equation 2.23) for an electron accelerated by an incident EMW (whose amplitude is parametrized by $\mu \equiv \omega/\omega_c$) and decelerated by the induced electric field of the CSR (which is parameterized by $b \equiv a/\omega_c$). In this case we chose $b = \mu = 10^{-2}$, according to Equation (3.24).

r_i, from the source of the FRB.

- **Zone 1 (brown region):** Protons and electrons radiate coherently with coherence-modified equations of motion. This means that we do not know how protons and electrons move and radiate since the coherent radiation is strong enough to modify the particle's energy.

- **Zone 2 (purple region):** Protons and electrons radiate coherently. Electrons have coherence-modified equations of motion (thus, we do not exactly know how they move and radiate). On the other hand, protons have regular equations of motion, so they follow the Equations 2.19, 2.20, 2.25, 2.26, and radiate according to Equation 3.12.

- **Zone 3 (blue region):** Here, electrons radiate coherently with coherence-modified equations of motion, while protons are not accelerated to relativistic speeds.

- **Zone 4 (light blue region):** Protons and electrons radiate coherently. Protons with coherence-modified equations of motion. Electrons have regular equations of motion (Equations 2.19, 2.20, 2.25, 2.26), and radiate according to Equation 3.12.

- **Zone 5 (light red region):** Protons and electrons radiate coherently, but this time both follow the regular equations of motion (Equations 2.19, 2.20, 2.25, 2.26), and radiate according to Equation 3.12.
- **Zone 6 (green region):** Here electrons radiate coherently (following Equation 3.12) while protons incoherently (following Equation 2.29), both with regular equations of motion.
- **Zone 7 (orange region):** Here, electrons radiate coherently with regular equations of motion, while protons are not accelerated at relativistic speeds.
- **Zone 8 (yellow region):** Electrons radiate incoherently with known equations of motion while protons radiate coherently with coherence-modified equations of motion.
- **Zone 9 (pink region):** Electrons radiate incoherently while protons radiate coherently, both with regular equations of motion.
- **Zone 10 (cyan region):** Protons and electrons radiate incoherently with regular equations of motion.
- **Zone 11 (light green region):** Here, electrons radiate incoherently with regular equations of motion, while protons are not accelerated to relativistic speeds.
- **"$n_{CSR,\,trf}(r_i)$" (continuous green curve):** Below this curve the electrons move freely for a distance $\Delta r \sim r_i$ within the CSR.
- **"$n_{CSR,\,trf}(\Delta_{sc})$" (dashed black curve):** Below this curve the electrons move freely for a distance $\Delta r \sim \Delta_{sc}$ (one semi-cycle) within the CSR. As a corollary, above this curve electrons would be promptly stopped by the induced electric field, E_{CSR} (which is why above this curve the figure is empty).

3.5 Cumulative coherent radiation analysis

Until this point, we have analyzed the effects of radiation over the equations of motion of the accelerating particles in order to know how they behave and how much energy is drained from the EMF by the conversion into kinetic energy. In this section, we will see that an important part of the energy budget of the FRB could be cumulatively scattered by coherent radiation over the several cycles of acceleration that the particles will experience.

To do that, we will consider that our estimations related to coherent radiation from Section 3.2 are valid, which also assumes the validity of the solutions for the regular equations of motion. To calculate the total coherently radiated energy, we estimated the radiated energy per particle and per semi-cycle by integrating the coherent radiation (Equation 3.12) along the timescale $t_{sc} = \tau_{sc}/\omega_i$ (Equation 2.23). This is

$$\frac{\mathcal{E}_{rad,coh}}{\text{semicycle}} = \int_0^{t_{sc}} P_{rad,coh} \mathrm{d}t \sim \begin{cases} \frac{4\pi}{9}\left(\frac{D}{1/2}\right)^{-2}\left(\frac{m_p}{m_e}\right)^{-2} n r_e^2 \frac{Lc}{\omega^2}\left(\frac{r_i}{r_{f,p^+}}\right)^2, & \left(\frac{r_i}{r_{f,p^+}}\right) \leq 3\left(\frac{m}{m_e}\right)^{-\frac{4}{5}} L_{42}^{-\frac{1}{10}} \\ \left(\frac{D}{1/2}\right)^2 \frac{n\pi^7}{36}\frac{r_e c^2}{\omega^2} m_e c^2 \left(\frac{\omega_i}{\omega}\right)^8, & \left(\frac{r_i}{r_{f,p^+}}\right) > 3\left(\frac{m}{m_e}\right)^{-\frac{4}{5}} L_{42}^{-\frac{1}{10}}. \end{cases} \tag{3.36}$$

Our next step was to integrate this along all semi-cycles,

$$N \equiv \frac{c\Delta t}{\lambda/2} \sim 2 \times 10^6 \, \nu_9 \, \Delta t_{-3}, \tag{3.37}$$

contained within the FRB pulse. Noticing that each step size is estimated as

$$\begin{aligned} \frac{\Delta_{sc}}{r_{f,p^+}} = \frac{c\, t_{sc}}{r_{f,p^+}} &= \left(\frac{D}{1/2}\right)^2 \frac{\pi^2}{6}\frac{m_p}{m_e}\left(m_e c^2 L \frac{c}{r_e}\right)^{1/2}\left(\frac{\omega_i}{\omega}\right)^2 \\ &= \left(\frac{D}{1/2}\right)^2 \frac{1}{6}\left(\frac{m_p}{m_e}\right)^3 \left(\frac{m_e c^2}{L}\frac{c}{r_e}\right)^{1/2}\left(\frac{r_i}{r_{f,p^+}}\right)^{-2}\left(\frac{m}{m_e}\right)^{-2}, \end{aligned} \tag{3.38}$$

we can estimate the radial distance distribution at any step cycle number, k, by approximating

$$\frac{\mathrm{d}r/r_{f,p^+}}{\mathrm{d}k} \sim \frac{\Delta r/r_{f,p^+}}{\Delta k} \sim \frac{\Delta_{sc,k}}{r_{f,p^+}} \sim \mathcal{C}\left(\frac{r}{r_{f,p^+}}\right)^{-2}, \tag{3.39}$$

and then integrating this expression to obtain

$$\frac{r_k}{r_{f,p^+}} \sim \left[3\mathcal{C}k + \left(\frac{r_i}{r_{f,p^+}}\right)^3\right]^{1/3}, \tag{3.40}$$

where

$$\mathcal{C} = \left(\frac{D}{1/2}\right)^2 \frac{1}{6} \left(\frac{m_p}{m_e}\right)^3 \left(\frac{m_e c^2}{L}\frac{c}{r_e}\right)^{1/2} \left(\frac{m}{m_e}\right)^{-2} \sim 3 \times 10^{-4} \left(\frac{m}{m_e}\right)^{-2} L_{42}^{-1/2}. \tag{3.41}$$

We integrate the total energy radiated per particle for each of the branches of $\mathcal{E}_{rad,coh}$ (Equation 3.36), so in the case $r_i/r_{f,p^+} \leq 3\,(m/m_e)^{-\frac{4}{5}}\, L_{42}^{-\frac{1}{10}}$ we have

$$\begin{aligned}
\mathcal{E}_{cycles} &\sim \sum_{k=0}^{k=N} \frac{\mathcal{E}_{rad,coh,k}}{\text{semicycle}} = \mathcal{K}_1 \sum_{k=0}^{k=N} \left(\frac{r_k}{r_{f,p^+}}\right)^2 \sim \mathcal{K}_1 \int_0^N \left[3\mathcal{C}k + \left(\frac{r_i}{r_{f,p^+}}\right)^3\right]^{2/3} \mathrm{d}k \\
&\sim \frac{\mathcal{K}_1}{5\mathcal{C}} \left(\frac{r_i}{r_{f,p^+}}\right)^5 \left\{\left[1 + 3\mathcal{C}N \left(\frac{r_i}{r_{f,p^+}}\right)^{-3}\right]^{5/3} - 1\right\} \\
&\sim 2 \times 10^4\,\text{erg} \left(\frac{n}{\text{cm}^{-3}}\right) \left(\frac{r_i}{r_{f,p^+}}\right)^5 \left(\frac{m}{m_e}\right)^2 L_{42}^{3/2}\, \nu_9^{-2} \\
&\quad \left\{\left[1 + 10^3 \left(\frac{r_i}{r_{f,p^+}}\right)^{-3} \left(\frac{m}{m_e}\right)^{-2} L_{42}^{-1/2}\, \nu_9\, \Delta t_{-3}\right]^{5/3} - 1\right\},
\end{aligned} \tag{3.42}$$

where

$$\mathcal{K}_1 = \frac{4\pi}{9} \left(\frac{D}{1/2}\right)^{-2} \left(\frac{m_p}{m_e}\right)^{-2} n r_e^2 \frac{Lc}{\omega^2} \sim 30\,\text{erg} \left(\frac{n}{\text{cm}^{-3}}\right) L_{42}\, \nu_9^{-2}. \tag{3.43}$$

while in the case $r_i/r_{f,p^+} > 3\,(m/m_e)^{-\frac{4}{5}}\, L_{42}^{-\frac{1}{10}}$ we obtain

$$\begin{aligned}
\mathcal{E}_{cycles} &\sim \sum_{k=0}^{k=N} \frac{\mathcal{E}_{rad,coh,k}}{\text{cycle}} = \mathcal{K}_2 \sum_{k=0}^{k=N} \left(\frac{r_k}{r_{f,p^+}}\right)^{-8} \sim \mathcal{K}_2 \int_0^N \left[3\mathcal{C}k + \left(\frac{r_i}{r_{f,p^+}}\right)^3\right]^{-8/3} \mathrm{d}k \\
&\sim \frac{\mathcal{K}_2}{5\mathcal{C}} \left(\frac{r_i}{r_{f,p^+}}\right)^{-5} \left\{1 - \left[1 + 3\mathcal{C}N \left(\frac{r_i}{r_{f,p^+}}\right)^{-3}\right]^{-5/3}\right\} \\
&\sim 10^9\,\text{erg} \left(\frac{n}{\text{cm}^{-3}}\right) \left(\frac{r_i}{r_{f,p^+}}\right)^{-5} \left(\frac{m}{m_e}\right)^{-6} L_{42}^{1/2}\, \nu_9^{-2} \\
&\quad \left\{1 - \left[1 + 10^3 \left(\frac{r_i}{r_{f,p^+}}\right)^{-3} \left(\frac{m}{m_e}\right)^{-2} L_{42}^{-1/2}\, \nu_9\, \Delta t_{-3}\right]^{-5/3}\right\},
\end{aligned} \tag{3.44}$$

where

$$\mathcal{K}_2 = \left(\frac{D}{1/2}\right)^2 \left(\frac{m_p}{m_e}\right)^8 \frac{n}{36\pi} \frac{r_e c^2}{\omega^2} m_e c^2 \left(\frac{m}{m_e}\right)^{-8} \sim 10^6 \,\mathrm{erg} \left(\frac{n}{\mathrm{cm}^{-3}}\right) \left(\frac{m}{m_e}\right)^{-8} \nu_9^{-2}. \quad (3.45)$$

Then, integrating all the particles within an initial radius, r_i,

$$\mathcal{E}_{tot}\left(r_i\right) \sim 4\pi r_i^2 n \, \mathcal{E}_{cycles} \, \Delta r_i \sim 4\pi r_{f,p^+}^3 n \, \mathcal{E}_{cycles} \left(\frac{r_i}{r_{f,p^+}}\right)^3, \quad (3.46)$$

and then comparing this energy with the energy budget of the FRB, we obtain the plasma density restrictions

$$\begin{aligned} n \ll n_{coh,scat} \sim 12\,\mathrm{cm}^{-3} & \left(\frac{r_i}{r_{f,p^+}}\right)^{-4} \left(\frac{m}{m_e}\right)^{-1} L_{42}^{-1} \, \nu_9^{5/2} \, \Delta t_{-3}^{1/2} \\ & \left\{\left[1 + 10^3 \left(\frac{r_i}{r_{f,p^+}}\right)^{-3} \left(\frac{m}{m_e}\right)^{-2} L_{42}^{-1/2} \, \nu_9 \, \Delta t_{-3}\right]^{5/3} - 1\right\}^{-1/2}, \end{aligned} \quad (3.47)$$

for $\left(r_i/r_{f,p^+}\right) \leq 3\left(m/m_e\right)^{-\frac{4}{5}} L_{42}^{-\frac{1}{10}}$, and

$$\begin{aligned} n \ll n_{coh,scat} \sim 5 \times 10^{-2}\,\mathrm{cm}^{-3} & \left(\frac{r_i}{r_{f,p^+}}\right) \left(\frac{m}{m_e}\right)^3 L_{42}^{-1/2} \, \nu_9^{5/2} \, \Delta t_{-3}^{1/2} \\ & \left\{1 - \left[1 + 10^3 \left(\frac{r_i}{r_{f,p^+}}\right)^{-3} \left(\frac{m}{m_e}\right)^{-2} L_{42}^{-1/2} \, \nu_9 \, \Delta t_{-3}\right]^{-5/3}\right\}^{-1/2} \end{aligned} \quad (3.48)$$

for $\left(r_i/r_{f,p^+}\right) > 3\left(m/m_e\right)^{-\frac{4}{5}} L_{42}^{-\frac{1}{10}}$. The previous restrictions prevent the complete scattering of the FRB energy through coherent radiation from the accelerating particles.

Figure 3.5 shows the restriction, $n_{coh,scat}$ (Equations 3.47 and 3.48), to avoid the complete depletion of the energy budget of a putative FRB (of luminosity $L \sim 10^{42}$ erg/s and duration $\Delta t \sim 1$ms) through the coherent radiation emitted by accelerating protons (continued yellow line) and electrons (continued blue line) initially located at r_i, throughout their interaction with the EMW of the FRB.

The results of Figure 3.5 show that the most relevant plasma density restriction might be produced by the coherently radiating electrons, which at $r_i \sim r_{f,p^+}$ impose a plasma

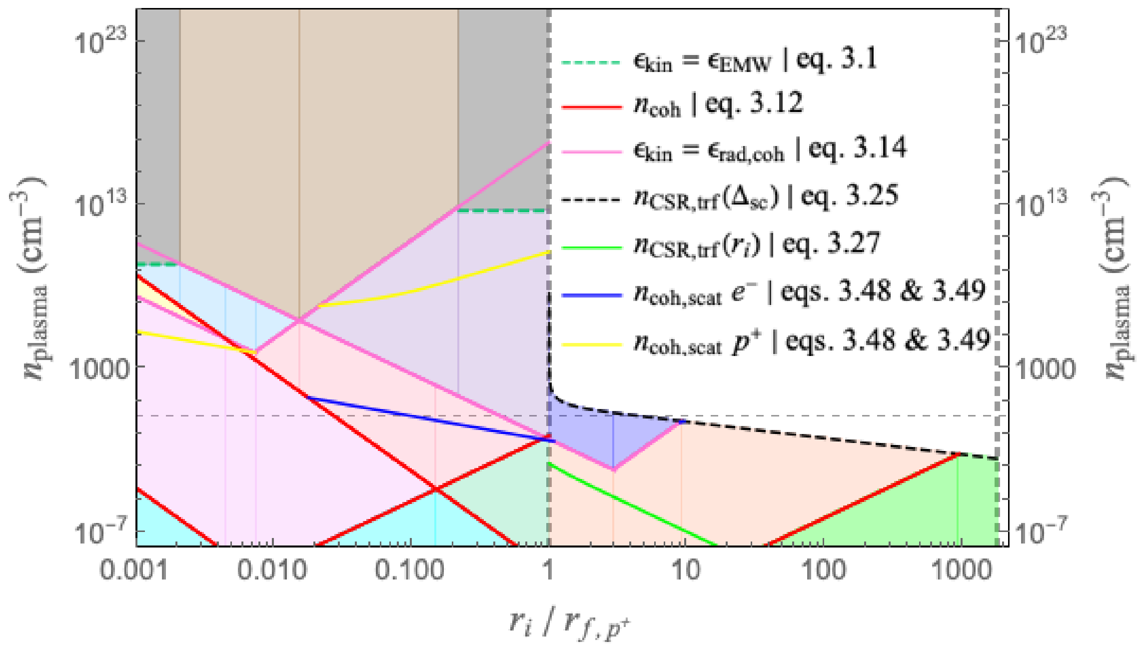

Figure 3.5: This figure shows the plasma density restriction, $n_{coh,scat}$ (Equations 3.47 and 3.48), set to prevent the complete scattering of the FRB energy budged through the coherent radiation emitted by electrons and protons accelerated by a EMW of amplitude $E \sim \sqrt{L/c\,r_i^2}$ from an observed FRB of luminosity, $L = 10^{42}$ erg/s, and frequency $\nu = 1$GHz.

density limit

$$n \ll n_{coh,scat}(r_{f,p^+}) \sim 3 \times 10^{-2}\,\mathrm{cm}^{-3}\,L_{42}^{-7/12}\,\nu_9^{5/3}\,\Delta t_{-3}^{-1/3}, \tag{3.49}$$

which is small, and becomes even smaller for $L > 10^{42}$ erg/s, one of the parameters of FRBs that varies the most.

The restrictions were set from the consideration of a particle acceleration process at a given initial radius, r_i, so their validity actually depends on whether the coherent radio wave was produced at that radius or not. We will discuss more about this in the next chapter. Also note that the restriction were set under the condition that the particles could reach $\gamma \sim \gamma_{max}$, which in the case of a radially-decaying EMW amplitude occurs at $r_i/r_{f,p^+} > r_{lim}/r_{f,p^+} \sim 5 \times 10^{-2}\,(m/m_e)^{-2/3}\,L_{42}^{-1/6}$ (see Equation 2.50 from Subsection 2.2.1), so that the restriction from equation 3.48 should be valid at $r_i \gtrsim 0.1\,r_{f,p^+}$ in the case of Figure 3.5.

Chapter 4

Discussion and conclusions

In this chapter we want to identify any information that could give a new insight about the FRB phenomenon. In order to do so, first we make a short comparison of our particle acceleration model with a previous similar analysis in the literature (Luan and Goldreich, 2014). Then, we analyze the limitations of the plasma density restrictions obtained from the analysis of our coherent-radiation model. After that, we use our results to constrain the emitting location of the FRB signal in the context of the "curvature radiation" (Cordes and Wasserman, 2016; and Kumar et al., 2017) and "synchrotron maser" (Gallant et al., 1992, Lyubarsky, 2014) mechanisms. Finally we present our conclusions and propose future work.

4.1 Model comparison

Luan and Goldreich (2014) did a short order-of-magnitude analysis for the particle acceleration process near the FRB source which was based on a previous study by (Gunn and Ostriker, 1969). We note that the results from Luan and Goldreich (2014) and Gunn and Ostriker (1969) are consistent with ours when estimating the cyclical behavior and maximum Lorentz factor experienced by the accelerating particles under such intense EMWs. However, we emphasize that our work went further by analyzing the potential radiative effects of the particles on themselves and on the incident EMW of the FRB.

4.2 Limitations on the radiative restrictions

One of the most obvious limitations of our radiative analysis and, thus, of our plasma density restrictions (Equations 3.47 and 3.48) comes from analyzing their validity near and above the curve $\epsilon_{kin} = \epsilon_{rad,coh}$ (Equation 3.13), i.e, where the coherent radiation can significantly affect the particle's movement. What we might expect, however, is that the condition $\epsilon_{kin} < \epsilon_{rad,coh}$ indicates that the true equilibrium Lorentz factor $\gamma_{eq} < \gamma_{max}$ for the accelerating (and radiating) plasma particles. In that case, given our definition for the lateral coherent scale l_t (Equation 3.9), we could naively say that, for $\gamma_{eq} < \gamma_{max}$, our restriction for the plasma density could become more restrictive in its first branch (Equation 3.47) and less restrictive in its second branch (Equation 3.48). However, in order to obtain a more robust plasma density restriction we require a fully developed (and more complex) result for the Lorentz factor when $\epsilon_{kin} < \epsilon_{rad,coh}$, which is beyond the scope of our order-of-magnitude analysis.

We also notice that the plasma density restrictions of Equations (3.47) and (3.48) were established from assuming that the outgoing coherent radiation from the accelerating particles can completely scatter the incident electromagnetic energy of the FRB out to its nearby surroundings. Now, even though the coherent emission of the accelerating particles could in fact "modify" the original FRB signal, we are not certain that this modification could directly imply the complete scattering of the FRB energy. Thus, further analysis is needed to derive more reliable conclusions. Despite these limitations, for simplicity, here we take our plasma density restrictions as valid.

In order to resolve the limitations mentioned in this section, it is needed to self-consistently solve the Maxwell equations in conjunction with the equations of motion of the plasma particles –for example, when deriving the dispersion relation of waves in plasmas (Thorne and Blandford, 2017)–. One of the major complexities of completing this task is related to the highly relativistic nature of plasma when faced with such intense low-frequency waves.

4.3 Emission mechanism analysis

In the following analysis, we will assume NS-related progenitor scenarios, as was already observed for the galactic FRB 200428 (The CHIME/FRB Collaboration et al., 2020, Bochenek et al., 2020). We discuss the implications of our restrictions for two of the most accepted coherent emission mechanisms for FRBs in the literature:

4.3.1 Curvature radiation

The curvature radiation is the emission by relativistic bunches of particles (mainly positrons and electrons) that coherently radiate while following the curved magnetic field lines of their NS. Given the latter, the activation radius, r_{act}, of the FRB for this mechanism is restricted to occur within the NS magnetosphere (Cordes and Wasserman (2016); Kumar et al. (2017); Ghisellini and Locatelli (2018); Katz (2018a); Lu and Kumar (2019)), whose characteristic radius is set by the light cylinder

$$r_L = \frac{cP_\star}{2\pi} \sim 0.5 \times 10^{10}\,\mathrm{cm}\,P_{\star 0}, \tag{4.1}$$

where we normalized the latter expression by a rotational period, $P_\star = 1\,\mathrm{s}$.

Now, considering that $r_L < r_{f,p^+}$, the relevant density restriction (in this case, Equation 3.47) from our model of coherent radiation can be rewritten as

$$n \ll n_{coh,scat} \sim 0.5\,\mathrm{cm}^{-3} \left(\frac{r_i}{r_L}\right)^{-3/2} P_{\star 0}^{-3/2}\, L_{42}^{1/6}\, \nu_9^{1/6}\, \Delta t_{-3}^{-1/3}, \tag{4.2}$$

which is relatively low in comparison with the density one might expect to find within a NS magnetosphere (see Pétri, 2016; Cordes and Wasserman, 2016; and Cerutti and Beloborodov, 2017). As a consequence, we propose that emission mechanisms for FRBs produced within a NS magnetosphere (i.e., $r_{act} \lesssim r_L$, like in this case for curvature radiation) could be disadvantaged according to our model.

4.3.2 Synchrotron maser

After the onset of a magnetar flare, it is expected the expulsion of a substantial amount of magnetic energy and relativistic (and/or transrelativistic) plasma particles (see Gaensler et al., 2005, Granot et al., 2006, Beloborodov, 2017). This magnetic energy is transported outwards along with the plasma, and it has been proposed that it is transformed into the EMW of FRBs via the synchrotron maser mechanism, which is the stimulated emission from energetic particles gyrating in a strong and ordered magnetic field (Langdon et al., 1988, Hoshino et al., 1992, Gallant et al., 1992, Usov and Katz, 2000, Sagiv and Waxman, 2002). For FRBs, there are two possible distance scales, r_{act}, for which this process could occur:

The wind termination shock

For a magnetar of dipolar magnetic field $B_\star = 10^{15}\,G$, radius $r_\star = 10^6\,\mathrm{cm}$, and rotational period $P_\star = 1\,\mathrm{s}$, the wind termination shock is determined by the radial distance at which the wind pressure, $L_{sd}/4\pi r^2 c$ (where $L_{sd} = 16\pi^4 B_\star^6 r_\star^6 / c^3 P_\star^4$ is the spin-down luminosity of the NS), equals the pressure, p, of the nebula:

$$r_{ts} = \sqrt{\frac{4\pi^3 B_\star^2 r_\star^6}{P_{\star 0}^4 c^4 p}} \sim 10^{15}\,\mathrm{cm}\, B_{\star 15}\, r_{\star 6}^3\, P_{\star 0}^{-2}\, p_{-4}^{-1/2}, \tag{4.3}$$

where the pressure, p, is normalized to $10^{-4}\,\mathrm{dyn/cm^2}$ (the estimated pressure within the nebula of the repeater FRB 121102; Beloborodov, 2017, Lyubarsky, 2020).

Lyubarsky (2014) claims that $r_{ts} \sim 10^{15} - 10^{16}\,\mathrm{cm}$ is a promising location for the coherent radio emission of FRBs via the synchrotron maser mechanism in a positron/electron wind plasma. Since the restrictions of our model for this case could be extended up to $r_{f,e^-} \sim 10^{13}\,\mathrm{cm}\, L_{42}^{1/2} \nu_9^{-1}$, we cannot put any constraints over this model, even for the more extreme observed FRBs.

Around the place of collision of the wind with previously-ejected baryonic material

Metzger et al. (2019) and others (Beloborodov, 2017, Beloborodov, 2020, and Margalit et al., 2020) propose that the wind deceleration, and therefore, the radio emission of FRBs, could be produced at the meeting place between the newly and previously ejected baryonic material from the flares of a repeating FRB source. According to Metzger et al. (2019), this could occur at $\sim 10^{12} - 10^{14}\,\mathrm{cm}$, where there would be an ion/electron plasma density $n \sim 10^{2} - 10^{5}\,\mathrm{cm}^{-3}$. In such case, the restrictions from our model can be set up to $r_{f,p^+} \sim 10^{10}\,\mathrm{cm}\, L_{42}^{1/2} \nu_9^{-1}$, which means we cannot constrain the emission mechanism for this model.

We highlight that our restrictions are only moderately dependent on the FRB luminosity, except for the distance scale $r_f \propto L^{-1/2}$, which could induce some differences in our analysis. As a consequence, all the implications discussed in this section work well over a wide range of luminosities around $L \sim 10^{42}\,\mathrm{erg/s}$. However, our restrictions might allow the emission of FRBs from within the magnetosphere of a NS for the less luminous events (the lower the luminosity is, the deeper in the magnetosphere FRBs can be produced), such as the case of the galactic FRB 200428 (with $L \sim 10^{38}\,\mathrm{erg/s}$; The CHIME/FRB Collaboration et al., 2020, and Bochenek et al., 2020) from the magnetar SGR 1935+2154 (with $r_L \sim 10^{10}\,\mathrm{cm} P_\star/3.2\mathrm{s}$; Israel et al., 2014). Nevertheless, since a FRB mechanism should cover the complete FRB luminosity range, and that a vast fraction of it constrained by our model if FRBs are produced within the magnetosphere of a NS, we propose that the latter restriction hold for all FRBs.

4.4 Conclusions

In this thesis, we outlined a model of particle acceleration, which was motivated by the intense EMW that should be present in the vicinity of the source of a FRB. We showed that the accelerating particles will quickly become relativistic and move in the direction of the incident FRB wave. In this process the particles periodically reach a Lorentz factor, $\gamma_{max} \sim (\omega_c/2\pi\nu)^2 \gg 1$, which remains valid up to the radial distance,

$r_f = (e/2mc\nu)\sqrt{L/c} \sim 3 \times 10^{10}\,\mathrm{cm}\,(m/m_p)^{-1}\,L_{42}^{1/2}\,\nu_9^{-1}$. The fact that r_f is different for protons and electrons implies that a charge-separation region will form, disrupting the acceleration process of electrons beyond r_{f,p^+} if the plasma composition of the FRB source is dominated by ions and electrons.

In our model, we also analyzed the incoherent and coherent radiation processes experienced by the accelerating particles and concluded that the total emitted coherent radiation can be strong enough to modify the original FRB signal, potentially scattering the electromagnetic energy budget of this event out to the source environment if the FRB activation mechanism is produced at $r_{act} < r_f$ (depending on the plasma density and its composition). As a consequence of the latter, we propose that mechanisms that invoke the emission of FRBs from within the magnetosphere of a NS or magnetar (like the "coherent curvature radiation") might not be favoured by our model. Instead, we support alternative mechanisms in which the FRB is emitted far from the magnetosphere of a neutron star or magnetar, such as the "synchrotron maser". Naturally, given the limitations of our order-of-magnitude estimations, further work is required to obtain more conclusive results.

4.5 Future work

As discussed in this chapter, we need a further analysis of the solutions for the equations of motion of the plasma particles when $\epsilon_{kin} < \epsilon_{rad,coh}$ in order to obtain more reliable plasma density restrictions. In addition, it is necessary to understand how the coherent radiation modifies the incident FRB signal and how much of the initial FRB energy is transferred to the source environment. In order to solve these limitations, we propose to extend our work by self-consistently solving the Maxwell equations and the equations of motion of the plasma. We propose to look for more applications of our results to other progenitor scenarios for FRBs (see Platts et al., 2018). In addition, although this model was applied to FRBs, it is applicable to other FRB-like phenomena (such as the "giant pulses" of radio pulsars; Cordes and Wasserman, 2016); thus, we propose to look for applications in such kind of events.

Bibliography

M. Adachi and M. Kasai. An Analytical Approximation of the Luminosity Distance in Flat Cosmologies with a Cosmological Constant. *Progress of Theoretical Physics*, 127 (1):145–152, Jan 2012. doi: 10.1143/PTP.127.145.

D. C. Backer, T. Wong, and J. Valanju. A Plasma Prism Model for an Anomalous Dispersion Event in the Crab Pulsar. *The Astrophysical Journal*, 543:740–753, Nov. 2000. doi: 10.1086/317150.

K. W. Bannister, R. M. Shannon, J.-P. Macquart, C. Flynn, P. G. Edwards, M. O'Neill, S. Osłowski, M. Bailes, B. Zackay, N. Clarke, L. R. D'Addario, R. Dodson, P. J. Hall, A. Jameson, D. Jones, R. Navarro, J. T. Trinh, J. Allison, C. S. Anderson, M. Bell, A. P. Chippendale, J. D. Collier, G. Heald, I. Heywood, A. W. Hotan, K. Lee-Waddell, J. P. Madrid, J. Marvil, D. McConnell, A. Popping, M. A. Voronkov, M. T. Whiting, G. R. Allen, D. C.-J. Bock, D. P. Brodrick, F. Cooray, D. R. DeBoer, P. J. Diamond, R. Ekers, R. G. Gough, G. A. Hampson, L. Harvey-Smith, S. G. Hay, D. B. Hayman, C. A. Jackson, S. Johnston, B. S. Koribalski, N. M. McClure-Griffiths, P. Mirtschin, A. Ng, R. P. Norris, S. E. Pearce, C. J. Phillips, D. N. Roxby, E. R. Troup, and T. Westmeier. The Detection of an Extremely Bright Fast Radio Burst in a Phased Array Feed Survey. *The Astrophysical Journal Letters*, 841:L12, May 2017. doi: 10.3847/2041-8213/aa71ff.

K. W. Bannister, A. T. Deller, C. Phillips, J. P. Macquart, J. X. Prochaska, N. Tejos, S. D. Ryder, E. M. Sadler, R. M. Shannon, S. Simha, C. K. Day, M. McQuinn, F. O. North-Hickey, S. Bhandari, W. R. Arcus, V. N. Bennert, J. Burchett, M. Bouwhuis, R. Dodson, R. D. Ekers, W. Farah, C. Flynn, C. W. James, M. Kerr, E. Lenc, E. K.

Mahony, J. O'Meara, S. Osłowski, H. Qiu, T. Treu, V. U, T. J. Bateman, D. C. J. Bock, R. J. Bolton, A. Brown, J. D. Bunton, A. P. Chippendale, F. R. Cooray, T. Cornwell, N. Gupta, D. B. Hayman, M. Kesteven, B. S. Koribalski, A. MacLeod, N. M. McClure-Griffiths, S. Neuhold, R. P. Norris, M. A. Pilawa, R. Y. Qiao, J. Reynolds, D. N. Roxby, T. W. Shimwell, M. A. Voronkov, and C. D. Wilson. A single fast radio burst localized to a massive galaxy at cosmological distance. *Science*, 365(6453):565–570, Aug. 2019. doi: 10.1126/science.aaw5903.

A. M. Beloborodov. A Flaring Magnetar in FRB 121102? *The Astrophysical Journal Letters*, 843:L26, July 2017. doi: 10.3847/2041-8213/aa78f3.

A. M. Beloborodov. Blast Waves from Magnetar Flares and Fast Radio Bursts. *The Astrophysical Journal*, 896(2):142, June 2020. doi: 10.3847/1538-4357/ab83eb.

C. D. Bochenek, V. Ravi, K. V. Belov, G. Hallinan, J. Kocz, S. R. Kulkarni, and D. L. McKenna. A fast radio burst associated with a Galactic magnetar. *arXiv e-prints*, art. arXiv:2005.10828, May 2020.

P. C. Boyle and Chime/Frb Collaboration. First detection of fast radio bursts between 400 and 800 MHz by CHIME/FRB. *The Astronomer's Telegram*, 11901, Aug. 2018.

S. Burke-Spolaor, M. Bailes, R. Ekers, J.-P. Macquart, and F. Crawford, III. Radio Bursts with Extragalactic Spectral Characteristics Show Terrestrial Origins. *The Astrophysical Journal*, 727:18, Jan. 2011. doi: 10.1088/0004-637X/727/1/18.

M. Caleb, C. Flynn, M. Bailes, E. D. Barr, T. Bateman, S. Bhandari, D. Campbell-Wilson, A. J. Green, R. W. Hunstead, A. Jameson, F. Jankowski, E. F. Keane, V. Ravi, W. van Straten, and V. V. Krishnan. Fast Radio Transient searches with UTMOST at 843 MHz. *Monthly Notices of the Royal Astronomical Society*, 458:718–725, May 2016. doi: 10.1093/mnras/stw109.

M. Caleb, E. F. Keane, W. van Straten, M. Kramer, J. P. Macquart, M. Bailes, E. D. Barr, N. D. R. Bhat, S. Bhandari, M. Burgay, W. Farah, A. Jameson, F. Jankowski, S. Johnston, E. Petroff, A. Possenti, B. W. Stappers, C. Tiburzi, and V. Venkatraman

Krishnan. The SUrvey for Pulsars and Extragalactic Radio Bursts - III. Polarization properties of FRBs 160102 and 151230. *Monthly Notices of the Royal Astronomical Society*, 478:2046–2055, Aug. 2018. doi: 10.1093/mnras/sty1137.

B. Cerutti and A. M. Beloborodov. Electrodynamics of Pulsar Magnetospheres. *Space Science Reviews*, 207(1-4):111–136, July 2017. doi: 10.1007/s11214-016-0315-7.

S. Chatterjee, C. J. Law, R. S. Wharton, S. Burke-Spolaor, J. W. T. Hessels, G. C. Bower, J. M. Cordes, S. P. Tendulkar, C. G. Bassa, P. Demorest, B. J. Butler, A. Seymour, P. Scholz, M. W. Abruzzo, S. Bogdanov, V. M. Kaspi, A. Keimpema, T. J. W. Lazio, B. Marcote, M. A. McLaughlin, Z. Paragi, S. M. Ransom, M. Rupen, L. G. Spitler, and H. J. van Langevelde. A direct localization of a fast radio burst and its host. *Nature*, 541:58–61, Jan. 2017. doi: 10.1038/nature20797.

P. Chawla, V. M. Kaspi, A. Josephy, K. M. Rajwade, D. R. Lorimer, A. M. Archibald, M. E. DeCesar, J. W. T. Hessels, D. L. Kaplan, C. Karako-Argaman, V. I. Kondratiev, L. Levin, R. S. Lynch, M. A. McLaughlin, S. M. Ransom, M. S. E. Roberts, I. H. Stairs, K. Stovall, J. K. Swiggum, and J. van Leeuwen. A Search for Fast Radio Bursts with the GBNCC Pulsar Survey. *The Astrophysical Journal*, 844:140, Aug. 2017. doi: 10.3847/1538-4357/aa7d57.

P. Chawla, B. C. Andersen, M. Bhardwaj, E. Fonseca, A. Josephy, V. M. Kaspi, D. Michilli, Z. Pleunis, K. M. Bandura, C. G. Bassa, P. J. Boyle, C. Brar, T. Cassanelli, D. Cubranic, M. Dobbs, F. Q. Dong, B. M. Gaensler, D. C. Good, J. W. T. Hessels, T. L. Land ecker, C. Leung, D. Z. Li, H. . H. Lin, K. Masui, R. Mckinven, J. Mena-Parra, M. Merryfield, B. W. Meyers, A. Naidu, C. Ng, C. Patel, M. Rafiei-Ravandi, M. Rahman, P. Sanghavi, P. Scholz, K. Shin, K. M. Smith, I. H. Stairs, S. P. Tendulkar, and K. Vanderlinde. Detection of Repeating FRB 180916.J0158+65 Down to Frequencies of 300 MHz. *The Astrophysical Journal Letters*, 896(2):L41, June 2020. doi: 10.3847/2041-8213/ab96bf.

T. Chiba and T. Nakamura. The Luminosity Distance, the Equation of State, and the Geometry of the Universe. *Progress of Theoretical Physics*, 100(5):1077–1082, Nov 1998. doi: 10.1143/PTP.100.1077.

CHIME/FRB Collaboration, M. Amiri, K. Bandura, M. Bhardwaj, P. Boubel, M. M. Boyce, P. J. Boyle, C. . Brar, M. Burhanpurkar, T. Cassanelli, P. Chawla, J. F. Cliche, D. Cubranic, M. Deng, N. Denman, M. Dobbs, M. Fandino, E. Fonseca, B. M. Gaensler, A. J. Gilbert, A. Gill, U. Giri, D. C. Good, M. Halpern, D. S. Hanna, A. S. Hill, G. Hinshaw, C. Höfer, A. Josephy, V. M. Kaspi, T. L. Landecker, D. A. Lang, H.-H. Lin, K. W. Masui, R. Mckinven, J. Mena-Parra, M. Merryfield, D. Michilli, N. Milutinovic, C. Moatti, A. Naidu, L. B. Newburgh, C. Ng, C. Patel, U. Pen, T. Pinsonneault-Marotte, Z. Pleunis, M. Rafiei-Ravandi, M. Rahman, S. M. Ransom, A. Renard, P. Scholz, J. R. Shaw, S. R. Siegel, K. M. Smith, I. H. Stairs, S. P. Tendulkar, I. Tretyakov, K. Vanderlinde, and P. Yadav. A second source of repeating fast radio bursts. *Nature*, 566: 235–238, Jan. 2019a. doi: 10.1038/s41586-018-0864-x.

CHIME/FRB Collaboration, M. Amiri, K. Bandura, M. Bhardwaj, P. Boubel, M. M. Boyce, P. J. Boyle, C. Brar, M. Burhanpurkar, P. Chawla, J. F. Cliche, D. Cubranic, M. Deng, N. Denman, M. Dobbs, M. Fandino, E. Fonseca, B. M. Gaensler, A. J. Gilbert, U. Giri, D. C. Good, M. Halpern, D. Hanna, A. S. Hill, G. Hinshaw, C. Höfer, A. Josephy, V. M. Kaspi, T. L. Landecker, D. A. Lang, K. W. Masui, R. Mckinven, J. Mena-Parra, M. Merryfield, N. Milutinovic, C. Moatti, A. Naidu, L. B. Newburgh, C. Ng, C. Patel, U. Pen, T. Pinsonneault-Marotte, Z. Pleunis, M. Rafiei-Ravandi, S. M. Ransom, A. Renard, P. Scholz, J. R. Shaw, S. R. Siegel, K. M. Smith, I. H. Stairs, S. P. Tendulkar, I. Tretyakov, K. Vanderlinde, and P. Yadav. Observations of fast radio bursts at frequencies down to 400 megahertz. *Nature*, 566:230–234, Jan. 2019b. doi: 10.1038/s41586-018-0867-7.

CHIME/FRB Collaboration, B. C. Andersen, K. Bandura, M. Bhardwaj, P. Boubel, M. M. Boyce, P. J. Boyle, C. Brar, T. Cassanelli, P. Chawla, D. Cubranic, M. Deng, M. Dobbs, M. Fandino, E. Fonseca, B. M. Gaensler, A. J. Gilbert, U. Giri, D. C. Good, M. Halpern, A. S. Hill, G. Hinshaw, C. Höfer, A. Josephy, V. M. Kaspi, R. Kothes, T. L. Landecker, D. A. Lang, D. Z. Li, H. H. Lin, K. W. Masui, J. Mena-Parra, M. Merryfield, R. Mckinven, D. Michilli, N. Milutinovic, A. Naidu, L. B. Newburgh, C. Ng, C. Patel, U. Pen, T. Pinsonneault-Marotte, Z. Pleunis, M. Rafiei-Ravandi, M. Rahman, S. M. Ransom,

A. Renard, P. Scholz, S. R. Siegel, S. Singh, K. M. Smith, I. H. Stairs, S. P. Tendulkar, I. Tretyakov, K. Vanderlinde, P. Yadav, and A. V. Zwaniga. CHIME/FRB Discovery of Eight New Repeating Fast Radio Burst Sources. *The Astrophysical Journal Letters*, 885 (1):L24, Nov. 2019c. doi: 10.3847/2041-8213/ab4a80.

A. W. Clegg, A. L. Fey, and T. J. W. Lazio. The Gaussian Plasma Lens in Astrophysics: Refraction. *The Astrophysical Journal*, 496:253–266, Mar. 1998. doi: 10.1086/305344.

J. M. Cordes and T. J. W. Lazio. NE2001.I. A New Model for the Galactic Distribution of Free Electrons and its Fluctuations. *arXiv Astrophysics e-prints*, July 2002.

J. M. Cordes and M. A. McLaughlin. Searches for Fast Radio Transients. *The Astrophysical Journal*, 596:1142–1154, Oct. 2003. doi: 10.1086/378231.

J. M. Cordes and I. Wasserman. Supergiant pulses from extragalactic neutron stars. *Monthly Notices of the Royal Astronomical Society*, 457(1):232–257, Mar. 2016. doi: 10.1093/mnras/stv2948.

J. M. Cordes, R. S. Wharton, L. G. Spitler, S. Chatterjee, and I. Wasserman. Radio Wave Propagation and the Provenance of Fast Radio Bursts. *arXiv e-prints*, May 2016.

J. M. Cordes, I. Wasserman, J. W. T. Hessels, T. J. W. Lazio, S. Chatterjee, and R. S. Wharton. Lensing of Fast Radio Bursts by Plasma Structures in Host Galaxies. *The Astrophysical Journal*, 842:35, June 2017. doi: 10.3847/1538-4357/aa74da.

J. Cox, J. L. Coherent radiation from pulsars. *The Astrophysical Journal*, 229:734–741, Apr. 1979. doi: 10.1086/157008.

W. Deng and B. Zhang. Cosmological Implications of Fast Radio Burst/Gamma-Ray Burst Associations. *The Astrophysical Journal Letters*, 783:L35, Mar. 2014. doi: 10.1088/2041-8205/783/2/L35.

S. Dimoudi, K. Adamek, P. Thiagaraj, S. M. Ransom, A. Karastergiou, and W. Armour. A GPU Implementation of the Correlation Technique for Real-time Fourier Domain Pulsar Acceleration Searches. *The Astrophysical Journal Supplement Series*, 239(2):28, Dec. 2018. doi: 10.3847/1538-4365/aabe88.

B. T. Draine. *Physics of the Interstellar and Intergalactic Medium*. 2011.

E. Fonseca, B. C. Andersen, M. Bhardwaj, P. Chawla, D. C. Good, A. Josephy, V. M. Kaspi, K. W. Masui, R. Mckinven, D. Michilli, Z. Pleunis, K. Shin, S. P. Tendulkar, K. M. Bandura, P. J. Boyle, C. Brar, T. Cassanelli, D. Cubranic, M. Dobbs, F. Q. Dong, B. M. Gaensler, G. Hinshaw, T. L. Land ecker, C. Leung, D. Z. Li, H. H. Lin, J. Mena-Parra, M. Merryfield, A. Naidu, C. Ng, C. Patel, U. Pen, M. Rafiei-Ravandi, M. Rahman, S. M. Ransom, P. Scholz, K. M. Smith, I. H. Stairs, K. Vanderlinde, P. Yadav, and A. V. Zwaniga. Nine New Repeating Fast Radio Burst Sources from CHIME/FRB. *The Astrophysical Journal Letters*, 891(1):L6, Mar. 2020. doi: 10.3847/2041-8213/ab7208.

B. M. Gaensler, C. Kouveliotou, J. D. Gelfand, G. B. Taylor, D. Eichler, R. A. M. J. Wijers, J. Granot, E. Ramirez-Ruiz, Y. E. Lyubarsky, R. W. Hunstead, D. Campbell-Wilson, A. J. van der Horst, M. A. McLaughlin, R. P. Fender, M. A. Garrett, K. J. Newton-McGee, D. M. Palmer, N. Gehrels, and P. M. Woods. An expanding radio nebula produced by a giant flare from the magnetar SGR 1806-20. *Nature*, 434(7037): 1104–1106, Apr. 2005. doi: 10.1038/nature03498.

V. Gajjar, A. P. V. Siemion, D. C. Price, C. J. Law, D. Michilli, J. W. T. Hessels, S. Chatterjee, A. M. Archibald, G. C. Bower, C. Brinkman, S. Burke-Spolaor, J. M. Cordes, S. Croft, J. E. Enriquez, G. Foster, N. Gizani, G. Hellbourg, H. Isaacson, V. M. Kaspi, T. J. W. Lazio, M. Lebofsky, R. S. Lynch, D. MacMahon, M. A. McLaughlin, S. M. Ransom, P. Scholz, A. Seymour, L. G. Spitler, S. P. Tendulkar, D. Werthimer, and Y. G. Zhang. Highest Frequency Detection of FRB 121102 at 4-8 GHz Using the Breakthrough Listen Digital Backend at the Green Bank Telescope. *The Astrophysical Journal*, 863:2, Aug. 2018. doi: 10.3847/1538-4357/aad005.

Y. A. Gallant, M. Hoshino, A. B. Langdon, J. Arons, and C. E. Max. Relativistic, Perpendicular Shocks in Electron-Positron Plasmas. *The Astrophysical Journal*, 391:73, May 1992. doi: 10.1086/171326.

G. Ghisellini and N. Locatelli. Coherent curvature radiation and fast radio bursts. *Astronomy and Astrophysics*, 613:A61, June 2018. doi: 10.1051/0004-6361/201731820.

K. Gourdji, D. Michilli, L. G. Spitler, J. W. T. Hessels, A. Seymour, J. M. Cordes, and S. Chatterjee. A sample of low energy bursts from FRB 121102. *arXiv e-prints*, Mar. 2019.

F. Graham Smith, A. G. Lyne, and C. Jordan. The 1997 event in the Crab pulsar revisited. *Monthly Notices of the Royal Astronomical Society*, 410:499–503, Jan. 2011. doi: 10.1111/j.1365-2966.2010.17459.x.

J. Granot, E. Ramirez-Ruiz, G. B. Taylor, D. Eichler, Y. E. Lyubarsky, R. A. M. J. Wijers, B. M. Gaensler, J. D. Gelfand, and C. Kouveliotou. Diagnosing the Outflow from the SGR 1806-20 Giant Flare with Radio Observations. *The Astrophysical Journal*, 638(1): 391–396, Feb. 2006. doi: 10.1086/497680.

J. E. Gunn and J. P. Ostriker. Acceleration of High-Energy Cosmic Rays by Pulsars. *Physical Review Letters*, 22:728–731, Apr. 1969. doi: 10.1103/PhysRevLett.22.728.

T. H. Hankins and J. A. Eilek. Radio Emission Signatures in the Crab Pulsar. *The Astrophysical Journal*, 670:693–701, Nov. 2007. doi: 10.1086/522362.

T. E. Hassall, E. F. Keane, and R. P. Fender. Detecting highly dispersed bursts with next-generation radio telescopes. *Monthly Notices of the Royal Astronomical Society*, 436:371–379, Nov. 2013. doi: 10.1093/mnras/stt1598.

M. Haverkorn. Magnetic Fields in the Milky Way. In A. Lazarian, E. M. de Gouveia Dal Pino, and C. Melioli, editors, *Magnetic Fields in Diffuse Media*, volume 407 of *Astrophysics and Space Science Library*, page 483, Jan 2015. doi: 10.1007/978-3-662-44625-6_17.

J. W. T. Hessels. Fast Radio Bursts and their Possible Neutron Star Origins. *ArXiv e-prints*, Apr. 2018.

J. W. T. Hessels, L. G. Spitler, A. D. Seymour, J. M. Cordes, D. Michilli, R. S. Lynch, K. Gourdji, A. M. Archibald, C. G. Bassa, G. C. Bower, S. Chatterjee, L. Connor, F. Crawford, J. S. Deneva, V. Gajjar, V. M. Kaspi, A. Keimpema, C. J. Law, B. Marcote, M. A. McLaughlin, Z. Paragi, E. Petroff, S. M. Ransom, P. Scholz, B. W. Stappers, and

S. P. Tendulkar. FRB 121102 Bursts Show Complex Time-Frequency Structure. *arXiv e-prints*, Nov. 2018.

A. Hewish, S. J. Bell, J. D. H. Pilkington, P. F. Scott, and R. A. Collins. Observation of a Rapidly Pulsating Radio Source. *Nature*, 217:709–713, Feb. 1968. doi: 10.1038/217709a0.

M. Hoshino, J. Arons, Y. A. Gallant, and A. Langdon. Relativistic magnetosonic shock waves in synchrotron sources - Shock structure and nonthermal acceleration of positrons. *Astrophys. J.*, 390:454–479, 1992. doi: 10.1086/171296.

G. L. Israel, N. Rea, F. C. Zelati, P. Esposito, M. Burgay, S. Mereghetti, A. Possenti, and A. Tiengo. Chandra discovery of 3.2s X-ray pulsations from SGR 1935+2154. *The Astronomer's Telegram*, 6370:1, Aug. 2014.

A. Karastergiou, J. Chennamangalam, W. Armour, C. Williams, B. Mort, F. Dulwich, S. Salvini, A. Magro, S. Roberts, M. Serylak, A. Doo, A. V. Bilous, R. P. Breton, H. Falcke, J.-M. Grießmeier, J. W. T. Hessels, E. F. Keane, V. I. Kondratiev, M. Kramer, J. van Leeuwen, A. Noutsos, S. Osłowski, C. Sobey, B. W. Stappers, and P. Weltevrede. Limits on fast radio bursts at 145 MHz with ARTEMIS, a real-time software backend. *Monthly Notices of the Royal Astronomical Society*, 452:1254–1262, Sept. 2015. doi: 10.1093/mnras/stv1306.

T. Katsouleas and J. M. Dawson. A plasma wave accelerator - surfatron i. *IEEE Transactions on Nuclear Science*, 30(4):3241–3243, 1983.

J. I. Katz. Coherent Emission in Fast Radio Bursts. *Phys. Rev.*, D89(10):103009, 2014. doi: 10.1103/PhysRevD.89.103009.

J. I. Katz. Fast radio bursts — A brief review: Some questions, fewer answers. *Modern Physics Letters A*, 31:1630013, Apr. 2016. doi: 10.1142/S0217732316300135.

J. I. Katz. Coherent plasma-curvature radiation in FRB. *Monthly Notices of the Royal Astronomical Society*, 481(3):2946–2950, Dec. 2018a. doi: 10.1093/mnras/sty2459.

J. I. Katz. Fast radio bursts. *Progress in Particle and Nuclear Physics*, 103:1–18, Nov. 2018b. doi: 10.1016/j.ppnp.2018.07.001.

M. J. Keith, A. Jameson, W. van Straten, M. Bailes, S. Johnston, M. Kramer, A. Possenti, S. D. Bates, N. D. R. Bhat, M. Burgay, S. Burke-Spolaor, N. D'Amico, L. Levin, P. L. McMahon, S. Milia, and B. W. Stappers. The High Time Resolution Universe Pulsar Survey - I. System configuration and initial discoveries. *Monthly Notices of the Royal Astronomical Society*, 409:619–627, Dec. 2010. doi: 10.1111/j.1365-2966.2010.17325.x.

A. Khokhlov, E. Mueller, and P. Hoeflich. Light curves of Type IA supernova models with different explosion mechanisms. *Astronomy and Astrophysics*, 270:223–248, Mar. 1993.

F. Kirsten, M. Snelders, M. Jenkins, K. Nimmo, J. van den Eijnden, J. Hessels, M. Gawronski, and J. Yang. Detection of two bright radio bursts from magnetar SGR 1935+2154. *arXiv e-prints*, art. arXiv:2007.05101, July 2020.

R. Kothes, X. Sun, B. Gaensler, and W. Reich. A Radio Continuum and Polarization Study of SNR G57.2+0.8 Associated with Magnetar SGR 1935+2154. *The Astrophysical Journal*, 852(1):54, Jan. 2018. doi: 10.3847/1538-4357/aa9e89.

P. Kumar, W. Lu, and M. Bhattacharya. Fast radio burst source properties and curvature radiation model. *Monthly Notices of the Royal Astronomical Society*, 468(3):2726–2739, July 2017. doi: 10.1093/mnras/stx665.

P. Kumar, R. M. Shannon, S. Osłowski, H. Qiu, S. Bhandari, W. Farah, C. Flynn, M. Kerr, D. R. Lorimer, J. P. Macquart, C. Ng, C. J. Phillips, D. C. Price, and R. Spiewak. Faint Repetitions from a Bright Fast Radio Burst Source. *The Astrophysical Journal Letters*, 887(2):L30, Dec. 2019. doi: 10.3847/2041-8213/ab5b08.

A. B. Langdon, J. Arons, and C. E. Max. Structure of relativistic magnetosonic shocks in electron-positron plasmas. *Phys. Rev. Lett.*, 61:779–782, Aug 1988. doi: 10.1103/PhysRevLett.61.779. URL `https://link.aps.org/doi/10.1103/PhysRevLett.61.779`.

C. J. Law, M. W. Abruzzo, C. G. Bassa, G. C. Bower, S. Burke-Spolaor, B. J. Butler, T. Cantwell, S. H. Carey, S. Chatterjee, J. M. Cordes, P. Demorest, J. Dowell, R. Fender, K. Gourdji, K. Grainge, J. W. T. Hessels, J. Hickish, V. M. Kaspi, T. J. W. Lazio, M. A.

McLaughlin, D. Michilli, K. Mooley, Y. C. Perrott, S. M. Ransom, N. Razavi-Ghods, M. Rupen, A. Scaife, P. Scott, P. Scholz, A. Seymour, L. G. Spitler, K. Stovall, S. P. Tendulkar, D. Titterington, R. S. Wharton, and P. K. G. Williams. A Multi-telescope Campaign on FRB 121102: Implications for the FRB Population. *The Astrophysical Journal*, 850:76, Nov. 2017. doi: 10.3847/1538-4357/aa9700.

D. R. Lorimer and M. Kramer. *Handbook of Pulsar Astronomy*. Dec. 2004.

D. R. Lorimer, M. Bailes, M. A. McLaughlin, D. J. Narkevic, and F. Crawford. A Bright Millisecond Radio Burst of Extragalactic Origin. *Science*, 318:777, Nov. 2007. doi: 10.1126/science.1147532.

W. Lu and P. Kumar. The maximum luminosity of fast radio bursts. *Monthly Notices of the Royal Astronomical Society*, 483(1):L93–L97, Feb. 2019. doi: 10.1093/mnrasl/sly200.

J. Luan and P. Goldreich. Physical Constraints on Fast Radio Bursts. *The Astrophysical Journal*, 785:L26, Apr. 2014. doi: 10.1088/2041-8205/785/2/L26.

Y. Lyubarsky. A model for fast extragalactic radio bursts. *Monthly Notices of the Royal Astronomical Society*, 442:L9–L13, July 2014. doi: 10.1093/mnrasl/slu046.

Y. Lyubarsky. Interaction of the electromagnetic precursor from a relativistic shock with the upstream flow - II. Induced scattering of strong electromagnetic waves. *Monthly Notices of the Royal Astronomical Society*, 490(1):1474–1478, Nov. 2019. doi: 10.1093/mnras/stz2712.

Y. Lyubarsky. Fast Radio Bursts from Reconnection in a Magnetar Magnetosphere. *The Astrophysical Journal*, 897(1):1, July 2020. doi: 10.3847/1538-4357/ab97b5.

M. Lyutikov. Fast Radio Bursts' Emission Mechanism: Implication from Localization. *The Astrophysical Journal Letters*, 838:L13, Mar. 2017. doi: 10.3847/2041-8213/aa62fa.

M. Lyutikov, L. Burzawa, and S. B. Popov. Fast radio bursts as giant pulses from young rapidly rotating pulsars. *Monthly Notices of the Royal Astronomical Society*, 462:941–950, Oct. 2016. doi: 10.1093/mnras/stw1669.

J.-P. Macquart and J. Y. Koay. Temporal Smearing of Transient Radio Sources by the Intergalactic Medium. *The Astrophysical Journal*, 776:125, Oct. 2013. doi: 10.1088/0004-637X/776/2/125.

J.-P. Macquart, R. M. Shannon, K. W. Bannister, C. W. James, R. D. Ekers, and J. D. Bunton. The Spectral Properties of the Bright Fast Radio Burst Population. *The Astrophysical Journal Letters*, 872:L19, Feb. 2019. doi: 10.3847/2041-8213/ab03d6.

J. P. Macquart, J. X. Prochaska, M. McQuinn, K. W. Bannister, S. Bhandari, C. K. Day, A. T. Deller, R. D. Ekers, C. W. James, L. Marnoch, S. Osłowski, C. Phillips, S. D. Ryder, D. R. Scott, R. M. Shannon, and N. Tejos. A census of baryons in the Universe from localized fast radio bursts. *Nature*, 581(7809):391–395, May 2020. doi: 10.1038/s41586-020-2300-2.

R. Main, I.-S. Yang, V. Chan, D. Li, F. X. Lin, N. Mahajan, U.-L. Pen, K. Vanderlinde, and M. H. van Kerkwijk. Pulsar emission amplified and resolved by plasma lensing in an eclipsing binary. *Nature*, 557:522–525, May 2018. doi: 10.1038/s41586-018-0133-z.

R. N. Manchester, G. B. Hobbs, A. Teoh, and M. Hobbs. The Australia Telescope National Facility Pulsar Catalogue. *The Astronomical Journal*, 129(4):1993–2006, Apr. 2005. doi: 10.1086/428488.

B. Marcote, Z. Paragi, J. W. T. Hessels, A. Keimpema, H. J. van Langevelde, Y. Huang, C. G. Bassa, S. Bogdanov, G. C. Bower, S. Burke-Spolaor, B. J. Butler, R. M. Campbell, S. Chatterjee, J. M. Cordes, P. Demorest, M. A. Garrett, T. Ghosh, V. M. Kaspi, C. J. Law, T. J. W. Lazio, M. A. McLaughlin, S. M. Ransom, C. J. Salter, P. Scholz, A. Seymour, A. Siemion, L. G. Spitler, S. P. Tendulkar, and R. S. Wharton. The Repeating Fast Radio Burst FRB 121102 as Seen on Milliarcsecond Angular Scales. *The Astrophysical Journal Letters*, 834:L8, Jan. 2017. doi: 10.3847/2041-8213/834/2/L8.

B. Marcote, K. Nimmo, J. W. T. Hessels, S. P. Tendulkar, C. G. Bassa, Z. Paragi, A. Keimpema, M. Bhardwaj, R. Karuppusamy, V. M. Kaspi, C. J. Law, D. Michilli, K. Aggarwal, B. Andersen, A. M. Archibald, K. Bandura, G. C. Bower, P. J. Boyle, C. Brar, S. Burke-Spolaor, B. J. Butler, T. Cassanelli, P. Chawla, P. Demorest, M. Dobbs, E. Fonseca,

U. Giri, D. C. Good, K. Gourdji, A. Josephy, A. Y. Kirichenko, F. Kirsten, T. L. Landecker, D. Lang, T. J. W. Lazio, D. Z. Li, H. H. Lin, J. D. Linford, K. Masui, J. Mena-Parra, A. Naidu, C. Ng, C. Patel, U. L. Pen, Z. Pleunis, M. Rafiei-Ravandi, M. Rahman, A. Renard, P. Scholz, S. R. Siegel, K. M. Smith, I. H. Stairs, K. Vanderlinde, and A. V. Zwaniga. A repeating fast radio burst source localized to a nearby spiral galaxy. *Nature*, 577(7789):190–194, Jan. 2020. doi: 10.1038/s41586-019-1866-z.

B. Margalit, B. D. Metzger, E. Berger, M. Nicholl, T. Eftekhari, and R. Margutti. Unveiling the engines of fast radio bursts, superluminous supernovae, and gamma-ray bursts. *Monthly Notices of the Royal Astronomical Society*, 481:2407–2426, Dec. 2018. doi: 10.1093/mnras/sty2417.

B. Margalit, B. D. Metzger, and L. Sironi. Constraints on the engines of fast radio bursts. *Monthly Notices of the Royal Astronomical Society*, 494(4):4627–4644, Apr. 2020. doi: 10.1093/mnras/staa1036.

K. Masui, H.-H. Lin, J. Sievers, C. J. Anderson, T.-C. Chang, X. Chen, A. Ganguly, M. Jarvis, C.-Y. Kuo, Y.-C. Li, Y.-W. Liao, M. McLaughlin, U.-L. Pen, J. B. Peterson, A. Roman, P. T. Timbie, T. Voytek, and J. K. Yadav. Dense magnetized plasma associated with a fast radio burst. *Nature*, 528:523–525, Dec. 2015. doi: 10.1038/nature15769.

M. A. McLaughlin and J. M. Cordes. Searches for Giant Pulses from Extragalactic Pulsars. *The Astrophysical Journal*, 596:982–996, Oct. 2003. doi: 10.1086/378232.

M. A. McLaughlin, A. G. Lyne, D. R. Lorimer, M. Kramer, A. J. Faulkner, R. N. Manchester, J. M. Cordes, F. Camilo, A. Possenti, and I. H. Stairs. Transient radio bursts from rotating neutron stars. *Nature*, 439(7078):817–820, Feb 2006. doi: 10.1038/nature04440.

S. Mereghetti, V. Savchenko, C. Ferrigno, D. Götz, M. Rigoselli, A. Tiengo, A. Bazzano, E. Bozzo, A. Coleiro, T. J. L. Courvoisier, M. Doyle, A. Goldwurm, L. Hanlon, E. Jourdain, A. von Kienlin, A. Lutovinov, A. Martin-Carrillo, S. Molkov, L. Natalucci, F. Onori, F. Panessa, J. Rodi, J. Rodriguez, C. Sánchez-Fernández, R. Sunyaev, and P. Ubertini. INTEGRAL Discovery of a Burst with Associated Radio Emission from the

Magnetar SGR 1935+2154. *The Astrophysical Journal Letters*, 898(2):L29, Aug. 2020. doi: 10.3847/2041-8213/aba2cf.

B. D. Metzger, B. Margalit, and L. Sironi. Fast radio bursts as synchrotron maser emission from decelerating relativistic blast waves. *Monthly Notices of the Royal Astronomical Society*, 485:4091–4106, May 2019. doi: 10.1093/mnras/stz700.

D. Michilli, A. Seymour, J. W. T. Hessels, L. G. Spitler, V. Gajjar, A. M. Archibald, G. C. Bower, S. Chatterjee, J. M. Cordes, K. Gourdji, G. H. Heald, V. M. Kaspi, C. J. Law, C. Sobey, E. A. K. Adams, C. G. Bassa, S. Bogdanov, C. Brinkman, P. Demorest, F. Fernandez, G. Hellbourg, T. J. W. Lazio, R. S. Lynch, N. Maddox, B. Marcote, M. A. McLaughlin, Z. Paragi, S. M. Ransom, P. Scholz, A. P. V. Siemion, S. P. Tendulkar, P. van Rooy, R. S. Wharton, and D. Whitlow. An extreme magneto-ionic environment associated with the fast radio burst source FRB 121102. *Nature*, 553:182–185, Jan. 2018. doi: 10.1038/nature25149.

V. Morello, E. D. Barr, B. W. Stappers, E. F. Keane, and A. G. Lyne. Optimal periodicity searching: revisiting the fast folding algorithm for large-scale pulsar surveys. *Monthly Notices of the Royal Astronomical Society*, 497(4):4654–4671, Aug. 2020. doi: 10.1093/mnras/staa2291.

K. Murase, K. Kashiyama, and P. Mészáros. A burst in a wind bubble and the impact on baryonic ejecta: high-energy gamma-ray flashes and afterglows from fast radio bursts and pulsar-driven supernova remnants. *Monthly Notices of the Royal Astronomical Society*, 461:1498–1511, Sept. 2016. doi: 10.1093/mnras/stw1328.

N. Oppermann, H. Junklewitz, M. Greiner, T. A. Enßlin, T. Akahori, E. Carretti, B. M. Gaensler, A. Goobar, L. Harvey-Smith, M. Johnston-Hollitt, L. Pratley, D. H. F. M. Schnitzeler, J. M. Stil, and V. Vacca. Estimating extragalactic Faraday rotation. *Astronomy and Astrophysics*, 575:A118, Mar. 2015. doi: 10.1051/0004-6361/201423995.

U.-L. Pen and L. Connor. Local Circumnuclear Magnetar Solution to Extragalactic Fast Radio Bursts. *The Astrophysical Journal*, 807:179, July 2015. doi: 10.1088/0004-637X/807/2/179.

J. Pétri. Theory of pulsar magnetosphere and wind. *Journal of Plasma Physics*, 82(5): 635820502, Oct. 2016. doi: 10.1017/S0022377816000763.

E. Petroff, M. Bailes, E. D. Barr, B. R. Barsdell, N. D. R. Bhat, F. Bian, S. Burke-Spolaor, M. Caleb, D. Champion, P. Chandra, G. Da Costa, C. Delvaux, C. Flynn, N. Gehrels, J. Greiner, A. Jameson, S. Johnston, M. M. Kasliwal, E. F. Keane, S. Keller, J. Kocz, M. Kramer, G. Leloudas, D. Malesani, J. S. Mulchaey, C. Ng, E. O. Ofek, D. A. Perley, A. Possenti, B. P. Schmidt, Y. Shen, B. Stappers, P. Tisserand, W. van Straten, and C. Wolf. A real-time fast radio burst: polarization detection and multiwavelength follow-up. *Monthly Notices of the Royal Astronomical Society*, 447:246–255, Feb. 2015a. doi: 10.1093/mnras/stu2419.

E. Petroff, E. F. Keane, E. D. Barr, J. E. Reynolds, J. Sarkissian, P. G. Edwards, J. Stevens, C. Brem, A. Jameson, S. Burke-Spolaor, S. Johnston, N. D. R. Bhat, P. C. S. Kudale, and S. Bhandari. Identifying the source of perytons at the Parkes radio telescope. *Monthly Notices of the Royal Astronomical Society*, 451:3933–3940, Aug. 2015b. doi: 10.1093/mnras/stv1242.

E. Petroff, E. D. Barr, A. Jameson, E. F. Keane, M. Bailes, M. Kramer, V. Morello, D. Tabbara, and W. van Straten. FRBCAT: The Fast Radio Burst Catalogue. *Publications of the Astronomical Society of Australia*, 33:e045, Sept. 2016. doi: 10.1017/pasa.2016.35.

E. Petroff, S. Burke-Spolaor, E. F. Keane, M. A. McLaughlin, R. Miller, I. Andreoni, M. Bailes, E. D. Barr, S. R. Bernard, S. Bhandari, and et al. A polarized fast radio burst at low Galactic latitude. *Monthly Notices of the Royal Astronomical Society*, 469: 4465–4482, Aug. 2017. doi: 10.1093/mnras/stx1098.

E. Petroff, J. W. T. Hessels, and D. R. Lorimer. Fast Radio Bursts. *arXiv e-prints*, Apr. 2019.

M. Pietka, R. P. Fender, and E. F. Keane. The variability time-scales and brightness temperatures of radio flares from stars to supermassive black holes. *Monthly Notices of the Royal Astronomical Society*, 446:3687–3696, Feb. 2015. doi: 10.1093/mnras/stu2335.

M. Pilia, M. Burgay, A. Possenti, A. Ridolfi, V. Gajjar, A. Corongiu, D. Perrodin, G. Bernardi, G. Naldi, G. Pupillo, F. Ambrosino, G. Bianchi, A. Burtovoi, P. Casella, C. Casentini, M. Cecconi, C. Ferrigno, M. Fiori, K. C. Gendreau, A. Ghedina, G. Naletto, L. Nicastro, P. Ochner, E. Palazzi, F. Panessa, A. Papitto, C. Pittori, N. Rea, G. A. R. Castillo, V. Savchenko, G. Setti, M. Tavani, A. Trois, M. Trudu, M. Turatto, A. Ursi, F. Verrecchia, and L. Zampieri. The Lowest-frequency Fast Radio Bursts: Sardinia Radio Telescope Detection of the Periodic FRB 180916 at 328 MHz. *The Astrophysical Journal Letters*, 896(2):L40, June 2020. doi: 10.3847/2041-8213/ab96c0.

E. Platts, A. Weltman, A. Walters, S. P. Tendulkar, J. E. B. Gordin, and S. Kandhai. A Living Theory Catalogue for Fast Radio Bursts. *arXiv e-prints*, art. arXiv:1810.05836, Oct 2018.

J. X. Prochaska, J.-P. Macquart, M. McQuinn, S. Simha, R. M. Shannon, C. K. Day, L. Marnoch, S. Ryder, A. Deller, K. W. Bannister, S. Bhandari, R. Bordoloi, J. Bunton, H. Cho, C. Flynn, E. K. Mahony, C. Phillips, H. Qiu, and N. Tejos. The low density and magnetization of a massive galaxy halo exposed by a fast radio burst. *Science*, 366 (6462):231–234, Oct. 2019. doi: 10.1126/science.aay0073.

V. Ravi, R. M. Shannon, M. Bailes, K. Bannister, S. Bhandari, N. D. R. Bhat, S. Burke-Spolaor, M. Caleb, C. Flynn, A. Jameson, S. Johnston, E. F. Keane, M. Kerr, C. Tiburzi, A. V. Tuntsov, and H. K. Vedantham. The magnetic field and turbulence of the cosmic web measured using a brilliant fast radio burst. *Science*, 354:1249–1252, Dec. 2016. doi: 10.1126/science.aaf6807.

V. Ravi, M. Catha, L. D'Addario, S. G. Djorgovski, G. Hallinan, R. Hobbs, J. Kocz, S. R. Kulkarni, J. Shi, H. K. Vedantham, S. Weinreb, and D. P. Woody. A fast radio burst localized to a massive galaxy. *Nature*, 572(7769):352–354, Aug. 2019. doi: 10.1038/s41586-019-1389-7.

G. B. Rybicki and A. P. Lightman. *Radiative Processes in Astrophysics*. June 1986.

A. Sagiv and E. Waxman. Collective processes in relativistic plasma and their implications for gamma-ray burst afterglows. *The Astrophysical Journal*, 574(2):861–872, aug 2002. doi: 10.1086/340948. URL `https://doi.org/10.1086%2F340948`.

R. M. Shannon, J.-P. Macquart, K. W. Bannister, R. D. Ekers, C. W. James, S. Osłowski, H. Qiu, M. Sammons, A. W. Hotan, M. A. Voronkov, R. J. Beresford, M. Brothers, A. J. Brown, J. D. Bunton, A. P. Chippendale, C. Haskins, M. Leach, M. Marquarding, D. McConnell, M. A. Pilawa, E. M. Sadler, E. R. Troup, J. Tuthill, M. T. Whiting, J. R. Allison, C. S. Anderson, M. E. Bell, J. D. Collier, G. Gürkan, G. Heald, and C. J. Riseley. The dispersion-brightness relation for fast radio bursts from a wide-field survey. *Nature*, 562:386–390, Oct. 2018. doi: 10.1038/s41586-018-0588-y.

M. Sokolowski, N. D. R. Bhat, J. P. Macquart, R. M. Shannon, K. W. Bannister, R. D. Ekers, D. R. Scott, A. P. Beardsley, B. Crosse, D. Emrich, T. M. O. Franzen, B. M. Gaensler, L. Horsley, M. Johnston-Hollitt, D. L. Kaplan, D. Kenney, M. F. Morales, D. Pallot, G. Sleap, K. Steele, S. J. Tingay, C. M. Trott, M. Walker, R. B. Wayth, A. Williams, and C. Wu. No Low-frequency Emission from Extremely Bright Fast Radio Bursts. *The Astrophysical Journal*, 867:L12, Nov. 2018. doi: 10.3847/2041-8213/aae58d.

L. G. Spitler, J. M. Cordes, J. W. T. Hessels, D. R. Lorimer, M. A. McLaughlin, S. Chatterjee, F. Crawford, J. S. Deneva, V. M. Kaspi, R. S. Wharton, B. Allen, S. Bogdanov, A. Brazier, F. Camilo, P. C. C. Freire, F. A. Jenet, C. Karako-Argaman, B. Knispel, P. Lazarus, K. J. Lee, J. van Leeuwen, R. Lynch, S. M. Ransom, P. Scholz, X. Siemens, I. H. Stairs, K. Stovall, J. K. Swiggum, A. Venkataraman, W. W. Zhu, C. Aulbert, and H. Fehrmann. Fast Radio Burst Discovered in the Arecibo Pulsar ALFA Survey. *The Astrophysical Journal*, 790(2):101, Aug 2014. doi: 10.1088/0004-637X/790/2/101.

L. G. Spitler, P. Scholz, J. W. T. Hessels, S. Bogdanov, A. Brazier, F. Camilo, S. Chatterjee, J. M. Cordes, F. Crawford, J. Deneva, R. D. Ferdman, P. C. C. Freire, V. M. Kaspi, P. Lazarus, R. Lynch, E. C. Madsen, M. A. McLaughlin, C. Patel, S. M. Ransom, A. Seymour, I. H. Stairs, B. W. Stappers, J. van Leeuwen, and W. W. Zhu. A repeating fast radio burst. *Nature*, 531:202–205, Mar. 2016. doi: 10.1038/nature17168.

S. P. Tendulkar, C. G. Bassa, J. M. Cordes, G. C. Bower, C. J. Law, S. Chatterjee, E. A. K.

Adams, S. Bogdanov, S. Burke-Spolaor, B. J. Butler, P. Demorest, J. W. T. Hessels, V. M. Kaspi, T. J. W. Lazio, N. Maddox, B. Marcote, M. A. McLaughlin, Z. Paragi, S. M. Ransom, P. Scholz, A. Seymour, L. G. Spitler, H. J. van Langevelde, and R. S. Wharton. The Host Galaxy and Redshift of the Repeating Fast Radio Burst FRB 121102. *The Astrophysical Journal Letters*, 834:L7, Jan. 2017. doi: 10.3847/2041-8213/834/2/L7.

The CHIME/FRB Collaboration, :, B. C. Andersen, K. M. Band ura, M. Bhardwaj, A. Bij, M. M. Boyce, P. J. Boyle, C. Brar, T. Cassanelli, P. Chawla, T. Chen, J. F. Cliche, A. Cook, D. Cubranic, A. P. Curtin, N. T. Denman, M. Dobbs, F. Q. Dong, M. Fandino, E. Fonseca, B. M. Gaensler, U. Giri, D. C. Good, M. Halpern, A. S. Hill, G. F. Hinshaw, C. Höfer, A. Josephy, J. W. Kania, V. M. Kaspi, T. L. Landecker, C. Leung, D. Z. Li, H. H. Lin, K. W. Masui, R. Mckinven, J. Mena-Parra, M. Merryfield, B. W. Meyers, D. Michilli, N. Milutinovic, A. Mirhosseini, M. Münchmeyer, A. Naidu, L. B. Newburgh, C. Ng, C. Patel, U. L. Pen, T. Pinsonneault-Marotte, Z. Pleunis, B. M. Quine, M. Rafiei-Ravandi, M. Rahman, S. M. Ransom, A. Renard, P. Sanghavi, P. Scholz, J. R. Shaw, K. Shin, S. R. Siegel, S. Singh, R. J. Smegal, K. M. Smith, I. H. Stairs, C. M. Tan, S. P. Tendulkar, I. Tretyakov, K. Vanderlinde, H. Wang, D. Wulf, and A. V. Zwaniga. A bright millisecond-duration radio burst from a Galactic magnetar. *arXiv e-prints*, art. arXiv:2005.10324, May 2020.

K. S. Thorne and R. D. Blandford. *Modern Classical Physics Optics, Fluids, Plasmas, Elasticity, Relativity, and Statistical Physics*. 2017.

D. Thornton, B. Stappers, M. Bailes, B. Barsdell, S. Bates, N. D. R. Bhat, M. Burgay, S. Burke-Spolaor, D. J. Champion, P. Coster, N. D'Amico, A. Jameson, S. Johnston, M. Keith, M. Kramer, L. Levin, S. Milia, C. Ng, A. Possenti, and W. van Straten. A Population of Fast Radio Bursts at Cosmological Distances. *Science*, 341:53–56, July 2013. doi: 10.1126/science.1236789.

O. Tsang and J. G. Kirk. The inverse Compton catastrophe and high brightness temperature radio sources. *Astronomy and Astrophysics*, 463(1):145–152, Feb 2007. doi: 10.1051/0004-6361:20066502.

V. V. Usov and J. I. Katz. Low frequency radio pulses from gamma-ray bursts? *Astron. Astrophys.*, 364:655, 2000.

S. Xu and B. Zhang. On the Origin of the Scatter Broadening of Fast Radio Burst Pulses and Astrophysical Implications. *The Astrophysical Journal*, 832:199, Dec. 2016. doi: 10.3847/0004-637X/832/2/199.

Y.-P. Yang and B. Zhang. Extracting Host Galaxy Dispersion Measure and Constraining Cosmological Parameters using Fast Radio Burst Data. *The Astrophysical Journal Letters*, 830:L31, Oct. 2016. doi: 10.3847/2041-8205/830/2/L31.

J. M. Yao, R. N. Manchester, and N. Wang. A New Electron-density Model for Estimation of Pulsar and FRB Distances. *The Astrophysical Journal*, 835:29, Jan. 2017. doi: 10.3847/1538-4357/835/1/29.

C. F. Zhang, J. C. Jiang, Y. P. Men, B. J. Wang, H. Xu, J. W. Xu, C. H. Niu, D. J. Zhou, X. Guan, J. L. Han, P. Jiang, K. J. Lee, D. Li, L. Lin, J. R. Niu, P. Wang, Z. L. Wang, R. X. Xu, W. Yu, B. Zhang, and W. W. Zhu. A highly polarised radio burst detected from SGR 1935+2154 by FAST. *The Astronomer's Telegram*, 13699:1, May 2020.

W. Zhu, L.-L. Feng, and F. Zhang. The Scattering of FRBs by the Intergalactic Medium: Variations, Strength, and Dependence on Dispersion Measures. *The Astrophysical Journal*, 865:147, Oct. 2018. doi: 10.3847/1538-4357/aadbb0.